2014

Aluminum foam core density and geometry influences on the deformation mechanisms and energy absorption capacity of foam filled braided tubular structures in axial and transverse loading

Ramsin Audysho
University of Windsor

ALUMINUM FOAM CORE DENSITY AND GEOMETRY INFLUENCES ON THE DEFORMATION MECHANISMS AND ENERGY ABSORPTION CAPACITY OF FOAM FILLED BRAIDED TUBULAR STRUCTURES IN AXIAL AND TRANSVERSE LOADING

By

Ramsin Audysho

A Thesis
Submitted to the Faculty of Graduate Studies
through the Department of Mechanical, Automotive, and Materials Engineering
in Partial Fulfillment of the Requirements for
the Degree of Master of Applied Science at the
University of Windsor

Windsor, Ontario, Canada

2013

ALUMINUM FOAM CORE DENSITY AND GEOMETRY INFLUENCES ON THE DEFORMATION MECHANISMS OF FOAM FILLED BRAIDED TUBULAR STRUCTURES IN AXIAL AND TRANSVERSE TENSION

by

Ramsin Audysho

APPROVED BY:

_____

F. Ghrib, Outside Department Reader
Department of Civil and Environmental Engineering

_____

N. Zamani, Internal Department Reader
Department of Mechanical, Automotive and Materials Engineering

_____

W. Altenhof, Advisor
Department of Mechanical, Automotive and Materials Engineering

December, 13/2013

DECLARATION OF CO-AUTHORSHIP AND PREVIOUS PUBLICATION

I. Co-Authorship Declaration

I hereby declare that this thesis incorporates material that is result of joint research undertaken in collaboration with Ryan Smith and Krishna Patel under the supervision of Professor William Altenhof. In all cases, the key ideas, primary contributions, experimental designs, data analysis and interpretation, were performed by the author, and the contribution of co-authors was primarily through the provision of experimental testing. I certify that I had a major role in preparation and writing of the manuscripts.

I am aware of the University of Windsor Senate Policy on Authorship and I certify that I have properly acknowledged the contribution of other researchers to my thesis, and have obtained written permission from each of the co-author(s) to include the above material(s) in my thesis.

I certify that, with the above qualification, this thesis, and the research to which it refers, is the product of my own work.

II. Declaration of Previous Publication

This thesis includes 2 original papers that have been previously published or submitted for publication in peer reviewed journals, as follows.

Thesis Chapter	Publication title/full citation	Publication status*
Chapters 1-8	Audysho R, Smith R, Altenhof W, Patel K. Aluminum foam core density and geometry influences on the deformation mechanisms of foam filled braided tubular structures in tension. Journal of Materials and Design, 2014; 54:394-413.	Published
Chapters 1-8	Audysho R, Smith R, Altenhof W (2014). Mechanical assessment of deformation mechanisms of aluminum foam filled stainless steel braided tubes subjected to transverse loading. Journal of Thin Walled Structures, submitted November 15, 2013.	Submitted

I certify that I have obtained a written permission from the copyright owner(s) to include the above published material(s) in my thesis. I certify that the above material describes work completed during my registration as graduate student at the University of Windsor.

I declare that, to the best of my knowledge, my thesis does not infringe upon anyone's copyright nor violate any proprietary rights and that any ideas, techniques, quotations, or any other material from the work of other people included in my thesis, published or otherwise, are fully acknowledged in accordance with the standard referencing practices. Furthermore, to the extent that I have included copyrighted material that surpasses the bounds of fair dealing within the meaning of the Canada Copyright Act, I certify that I have obtained a written permission from the copyright owner(s) to include such material(s) in my thesis.

I declare that this is a true copy of my thesis, including any final revisions, as approved by my thesis committee and the Graduate Studies office, and that this thesis has not been submitted for a higher degree to any other University or Institution.

ABSTRACT

The mechanical response of an energy absorbing device was studied experimentally by means of a custom built testing machine. Results showed that the force/displacement behaviour was strongly dependent upon foam density; however after tow lockup this dependency was reduced. Axially loaded specimens utilizing circular cores reduced the total elongation to failure and maximum load by approximately 120 mm and 7 kN, respectively compared to specimens utilizing rectangular cores. Good agreement and deviation between theoretical results and experimental tests for specimens with low and high density cores were observed with an error of 3.03% and 16.45%, respectively. Significant tensile loads and to a lesser extent bending within the braided tube occurred during transverse loading. Specimens containing circular foam cores were found to be more efficient in SEA, approximately 2 kJ/kg greater than rectangular cores. A 22% reduction in FE was determined for specimens containing rectangular cores compared to circular cores.

DEDICATION

To the love of my life, Christine Elkhoury; for her love, inspiration and patience.

ACKNOWLEDGEMENTS

First, I would like to thank the Lord Jesus Christ for HE has given me the strength, positive attitude, and courage that shape me as a person today.

I wish to express my sincere gratitude and appreciation to my advisor Dr. William Altenhof for all of the support, guidance, wisdom – morally and academically. His display of confidence in my abilities, throughout the course of my thesis, is never to be forgotten. During this research program, I adopted his professional habits which ultimately enabled me to propel through this challenging research program. His emphasis on engineering quality, detail, and organization add a great deal to the learning process which aids in avoiding obstacles ahead.

My sincere thanks go to Weldon Li, a colleague within Dr. Altenhof's research group, for his F.E.A. guidance and support in the early stages of this research. A great deal of appreciation goes to Andy Jenner for his technical assistance in the fabrication of fixture components related to the testing apparatus used for this research. As well, many thanks go to my committee members and the faculty and staff of the Department of Mechanical Engineering for their support.

Finally I wish to express my sincere appreciation to my parents and brother for their unlimited support and patience for encouraging me to pursue advanced education from the very beginning of my academic career.

TABLE OF CONTENTS

LIST OF TABLES

LIST OF FIGURES

LIST OF APPENDICES

Appendix Page

LIST OF ABBREVIATIONS

AISI	American iron and steel institute
CC	circular core
CNRB	constrained nodal rigid body
DOC	direct operating costs
FE	finite element
FE	force efficiency
FFT	foam filled tensile
IED	improvised explosive devices
LVDT	linear voltage differential transducer
NFT	no foam tensile
NFTT	no foam transverse tensile
NFVT	no foam verification tensile
OEF	operation enduring freedom
PEA	personal energy absorbers
RC	rectangular core
SEA	specific energy absorption
TEA	total energy absorbed
TFE	tensile force efficiency
TFFT	transverse foam filled tested
TTL	transistor-transistor logic

NOMENCLATURE

D	perpendicular distance between the tows (mm)
E_{foam}	energy absorbed by aluminum foam (kJ)
E_{total}	total energy absorbed by the structure (kJ)
E_{tube}	energy absorbed by braided tube (kJ)
F	axial force acting on the braided tube/foam core (kN)
f_2	ordinate (force) intercept for the second region of the bilinear force/displacement response of an empty braided tube (kN)
F_{avg}	average tensile force in y direction (kN)
F_{h_Tube}	horizontal component of the tensile force (kN)
F_{max}	max tensile force in y direction (kN)
F_{R_Tube}	resultant of the vertical and horizontal forces acting along the axial direction of the straight section of the braided tube (kN)
F_v	vertical force measured by the load cell (kN)
F_{v_Tube}	vertical component of the tensile force F_v (kN)
k_1	stiffness of the first region of the bilinear force/displacement response of an empty braided tube (kN/mm)
k_2	stiffness of the second region of the bilinear force/displacement response of an empty braided tube (kN/mm)
L	current length of braided tube during deformation (mm)
L_0	initial length of braided tube (mm)
L_{crit}	intersection point of the assumed linear force/displacement relationship (mm)
L_{foam}	length of aluminum foam core (mm)
L_{lockup}	tube length at lockup (mm)
l	unit cell length (mm)
l_x	unit cell length along the x direction (mm)
l_y	unit cell length along the y direction (mm)
R	current radius of aluminum foam filled braided tube during deformation (mm)

R_0	radius of braided tube after assembly of the aluminum foam filled braided tube (mm)
R_{lockup}	radius of braided tube at lockup (mm)
W	width of the tows (mm)
w	instantaneous width of the rectangular section of the aluminum foam core during radial crushing (mm)
w_o	original width of the rectangular section of the aluminum foam core (mm)
y	instantaneous length of the aluminum foam filled braided tube (mm)
Δy	displacement of centre loading bar (mm)
θ_0	initial angle between tows after assembly of the aluminum foam filled braided tube (degrees)
θ	current angle between tows in the unit cell of the braided tube (degrees)
θ_L	lockup angle between tows in the unit cell of the braided tube (degrees)
$\theta_{trans.}$	angle between the *x*-axis (horizontal) direction and the assumed line of action of tensile force (degrees)
ρ_f	aluminum foam core density (kg/m^3)
ϕ	diameter of circular foam core (mm)
δ	total elongation of the braided tube during the transverse deformation process (mm)
$\delta_{critical}$	displacement value representing the transition from foam crushing to significant braid deformation (mm)
σ_{pl}	plateau stress of the aluminum foam core (MPa)

1 INTRODUCTION

There exist many incidents and findings that affect human lives severely with associated economic impacts. These incidents continue to be a major health challenge to the public. Accidental falls are one of the leading causes of fatal and nonfatal injuries in the construction industry. A minimum fall of six feet will create massive impact forces to the fallen worker [1]. High impact forces cause significant injury, even if a worker is in a full body harness. Personal energy absorbers (PEA) reduce impact force and limit deceleration and are an important device in personal safety. The associated costs of fatal construction injuries impose significant economic burdens. In 2012, construction workers were 6.3% of the U.S. workforce [2], 71% higher than entire industry as a whole [3]. In 2004, falls where the leading cause of overall injury costs in Canada accounting for $6.2 billion or 31% of the total [4]. Furthermore, limitations to anthropometric data lead to obese construction workers using PEA not designed for their body weight measurements [5]. Such mismatch causes PEA failure resulting in unexpected injuries or even fatalities.

Composite technology is of interest in aerospace and defense products of all types because it can assist in decreasing total direct operating costs (DOC). The DOC ownership accounted for 50%. Within the 50%, airframe and engine components tallied 51% and 19% on DOC, respectively. In an initiative to maximize weight and fuel savings in the US commercial and defense sectors, between the periods 1970s to 2000s, use of advanced structural composites such as braided tubes and panels, increased by 30% [6]. Barriers that potentially can expand the application of braided composites are manufacturing costs, development costs, and maintenance technology [6]. It is estimated such barriers will cost billions of dollars in investment and research and development [7].

In blast loading conditions, head and body armour assist in mitigating or reducing the likelihood of body trauma. During the periods October 2001 to August 2007, the United States Armed Forces suffered contact with Improvised Explosive Devices (IEDs) which lead to 3000 combat deaths in Iraq and 240 combat deaths in Afghanistan [8]. Within the Canadian Forces, 97 of the 142 casualties in Operation Enduring Freedom (OEF) were a direct result of IEDs and suicide bombs during the conflict [9]. Penetration and/or

fragmentation injuries are the main sources of battlefield deaths. Improvements in body armour designs reduce injury patterns and increase the use of advanced blast protection equipment.

Regulatory agencies substantially change their automotive crash testing and assessment protocols for human injury prevention and road safety. Automotive manufacturers are forced to comply with these protocols. Recent figures from [10], estimated 1.18 million fatalities in road crashes and 50 million were injured worldwide. Traffic injuries were the 9th contributor to the global burden of disease and injury in 1990, and were expected to become 3rd leading contributor by 2020 [11]. From the mid-90s until 2004, Canada's transport accidents were the 3rd highest injury type with an economic burden of $3.7 billion. Given the facts, the increased incorporation of both passive and active energy absorbing devices gives rise to an increase in human injury prevention. Therefore, alternate lighter materials must be considered in the solution.

Since their introduction, energy dissipation devices have proven to be an effective tool in improving personal safety in a variety of engineering applications. Energy absorbing structures may include, but are not limited to, thin walled tubes, honeycomb members and cellular materials. It should be noted that these structures are more commonly observed under compressive loading conditions, for example vehicle crumple zones. In these zones, energy is intended to be absorbed by crushing, fracture, friction, folding, and bending deformation of the metal structures. This transmission of crash energy is maximized axially such that progressive folding pattern is achieved. Although less frequently encountered, tensile energy absorbers are utilized in a number of different applications which may include personal safety equipment and restraint systems.

Aluminum foam filled stainless steel braided structures show potential to replace many comparable metallic energy absorbing components currently in use today. Stainless steel braided tubes can be created with a high level of automation and can also be produced as net-shape parts, both of which are advantageous for manufacturers. In addition, they possess high impact and fatigue resistance, high strength and stiffness to weight ratios

and damage tolerance [12]. They perform well in a variety of loading conditions and are more robust than laminated composites. Moreover, owing to their high strength and load bearing capacity, braided tubes frequently exhibit desirable mechanical properties in the axial and transverse direction. As a result of these potential benefits, they are often implemented and considered in a large number of applications. Within the aerospace industry, braided tubes can be utilized for propeller blades, missile nose cones, aircraft engine containment and engine stator vanes [13]. Within the industrial sector, where cost is the major driving factor for part manufacturing, braided tubes are used as automobile side crossbeams and air bags, restraint devices, and industrial rollers. In addition to crossbeams, A-pillars, B-Pillars, windshield headers and roof side rails are typical structural members where combined forces cause bending mode collapse. This mode is caused by either buckling of the compressed surface or by cracking and tearing of the surface. These modes of failure are typically not favoured in side impact crash events, as they do not maximize energy absorption capacity.

A disadvantage for side impact crossbeams is that energy absorption is localized at the immediate area that undergoes bending. Like foam filled braided tubes, it is efficient if the overall length of the beam could deform and absorb the energy upon impact. Factors influencing side door crossbeams are load path and maximum resisting load of the door [14]. The load carrying capacity and intrusion of the side door structure mainly depends on mechanical properties, shape, size and thickness of its components [14]. The proper combination of these features can dramatically change the behaviour of the structure, providing an efficient, stiff, and crashworthy design. As such, use of braided tubes as crossbeams and restraint devices requires the need for a more comprehensive understanding of the performance of such structures under transverse loading. In other applications, the braided tube can be used as a partial reinforcement in structures such as shipping containers and boat hulls.

The aim of this thesis includes two portions: First, expand and build upon the research completed by both Powell et al. [15] and Cheng et al. [16]. Second, investigate the mechanical response, identify deformation mechanisms, and assess the failure

characteristics of braided tubes with different aluminum foam core geometries through continuously applied uniaxial and transverse loading conditions.

Tensile tests of both empty and aluminum foam filled braided stainless steel tubes were completed using a custom built long stroke testing machine. Powell et al. [15] was forced to complete tensile tests in stages. Between each stage the specimen was unloaded and removed from the testing apparatus, which did disturb the specimen to some extent, which could not be quantified. Use of the long stroke machine, detailed within this thesis, proved to be beneficial as it allowed for a continuous load to be applied to each specimen, until failure, without any form of interruption during testing. A thorough review of past research and literature did not yield any standardized testing protocol for the materials considered in this study. Correspondingly, testing of the metallic foam filled braided stainless steel tubes were completed in a similar fashion as in [15] with the exception of the uninterrupted nature of the testing. The recorded data prior to tow lockup was compared to the results predicted by the theoretical unit cell model developed by Cheng et al. [16] to assess the validity of the model. This analysis was not previously completed by the authors in [16]. Additionally, the research presented in this manuscript also provides for some limitations associated with the theoretical model by Cheng et al. [16].

Transverse loading tests of both empty and aluminum foam filled braided stainless steel tubes were carried out using the long stroke testing machine. The presented findings within this thesis are novel as quantitative assessment of metallic foam filled braided tube deformation and performance characteristics are completed which allows for a greater understanding of overall braided tube/foam performance.

2 REVIEW OF LITERATURE

As related to the research of this thesis, the literature review discusses the experimental testing, theoretical analysis, and finite element simulations of metallic and composite tubular and chain like structures subjected to a variety of loading conditions for identification of failure mechanisms, foam core influence on geometry, and assessment of mechanical response. Section 2.1 discusses the effect of foam core in metallic and composite tube specimens functioning under tensile loads as a unit. Section 2.2 discusses similar literature, however, pertaining to specimens subjected to transverse loaded metallic and composite tubes and panels.

2.1 Deformation mode under uniaxial loading

There are limited publications related to foam filled braided tubes specimens in uniaxial loading. Previous development of efficient tensile energy absorption devices was explored by Cox and Davis [17]. They have completed a study investigating the energy absorption capabilities of braided composites. The samples consisted of fibre bundles or cords woven around dowel pins creating loops analogous to the links of a steel chain. Fibre bundles were arranged in such a manner that neighbouring loops were not in direct contact. The bundles were immersed in a variety of different matrix materials including (epoxy resin, polycarbonate, aluminum/magnesium alloy, and a lead tin alloy). Muralidhar et al. [18] studied both the tensile and compressive behaviour of 1 x 1 weft rib knitted preforms utilizing flax yarns reinforced with an epoxy matrix. Additionally, Goyal et al. [19] presented parametric studies on the various parameters affecting the mechanical properties of 2 x 2 braids. Knitted fabric reinforced composites have demonstrated a great degree of potential as a tensile energy absorbing structure due to several factors such as excellent formability and desirable mechanical properties.

Harte et al. [20-22] have examined the energy absorption capabilities of circular composite braided tubes both experimentally and theoretically. The tubes consisted of hand woven E-glass fibres reinforced with an epoxy matrix. The energy absorption of the tubes was attributed to scissoring of tows within the composite tube and cracking of the epoxy matrix. The stress/strain response of the tubes was shown to be governed by the initial helix angle of the tows relative to the tube axis. Experimental results show the failure mode of the tubes is governed by the initial helix angle. Helix angles smaller than 45 degrees resulted in tube failure due to fibre fracture before hard contact, at helix angles greater than 45 degrees the formation of a neck was observed. After neck propagation along the length of the tube, the fibres failed in pure shear. Circular braids used in combination with an interior core have shown promise as a tensile energy absorbing structure. Previously, the tensile response of circular braids used in combination with an elastic core has been examined both experimentally and numerically [23-25]. In addition to elastic cores, metallic foams have shown favourable performance for application in composite energy absorbing structures. Foam filling in tubular

specimens was explored by Schutze et al. [26] in truss structures where compressive and tensile loads commonly occur. The composite sandwich rods consisted of a lightweight metallic foam core covered by a relatively thin unidirectional glass braid outer layer and a composite inner layer.

Powell et al. [15] conducted an experimental study on both the force/displacement and energy dissipation characteristics of aluminum foam filled braided stainless steel tubes under quasi static tensile loading. The braided tube was selected due to the reduction in tube diameter under elongation. The reduction in tube diameter during elongation allows for compression loading of the interior foam core. The combination of the crushing of the foam core and elongation of the braided tube was determined to be the mechanism of energy dissipation for the composite structure. Due to limitations associated with the stroke length of the testing apparatus, tensile tests were completed in three individual stages. The force/displacement and energy/displacement results were subsequently juxtaposed to achieve a continuous data curve. Energy absorption ranged from approximately 5.2 kJ to 7.9 kJ, depending on the selected aluminum foam core density. Cheng et al. [16] expanded upon the work of Powell by developing a theoretical model based on the kinematic relationship between elongation and tube diameter. The theoretical model was based upon the concept of the unit cell in which tube length and radius are related to the angle between crossing tows. Energy dissipation was a superposition of (1) crushing of the interior foam core prior to tow lockup, followed by (2) elongation/deformation associated with the braided tube after tow lockup. It was assumed that no “interaction effect” between the braided tube and foam core existed during tube elongation to influence the energy/displacement behaviour. The model is semi-empirical, as experimental data is required for the second phase of energy dissipation, namely the deformation associated with the braided tube. Predicted energy absorption levels were compared with experimental findings with a maximum percentage error of 25%. No validation of the unit cell concept prior to tow lockup was completed and details associated with the deformation mechanisms to assess unique observations of the force/displacement behaviour could not be conducted with their apparatus.

2.2 Deformation mode under transverse loading

Within the open literature, no publications were found that provide detailed examination of mechanical assessment and deformation mechanisms through transverse loading of empty and foam filled braided tubes. However, there exists a significant volume of research on foam filled composites and metallic circular tubes. Borvik et al. 2003 [27] conducted an experimental study where it was noted that addition of a foam core drastically increased the energy absorbing capabilities of metallic extrusions under bending loads compared to empty tubes. Saggar [28] conducted four point bending experiments on empty graphite epoxy laminated composite tubes under bending loads. Results indicate that the failure process is dependent on the fiber orientation and ply stacking sequence. Tubes were observed to fail in compression with fiber breakage and delamination being the prominent damage modes.

Nageswara et al. [29] presented findings on lateral crushing of triaxial braided composite tubes. The experimentally measured force/displacement responses of the composite tubes were validated to predictions from a theoretical model. The theoretical model utilized within the study was a modified existing unit cell based material model for axial crushing of tubes to predict the response of the triaxial braided composites under lateral loads. Matrix, fiber-tension and fiber-compression failures were the leading causes of lateral crushing of braided specimens. Finite element (FE) results predicted failure through matrix cracking in the loading vicinity, specifically by means of fiber compression. Mechanical responses indicated that lateral crushing was independent of the rate of loading and, as a result of the significant matrix rupture, dependent upon the mechanical material behaviour of the fibers. No distinct peak load in the experimental force/displacement response was observed and a consistent crushing load of 3 kN was noted. Littell et al. [30] analyzed 60 degree triaxial braided composite tubes with the 0° axial braid fibers perpendicular to the applied tensile load (transverse direction). The study has identified the formation of edges and local splitting of fiber tows as processes that have a significant effect on tensile strength. Gan et al. [31] summarized results from quasi-static FE simulations and experimental tests on the energy absorption characteristics of grid-stiffened composite structures under transverse compressive

loading. In this study, it was observed that compressive loading applied to the rib side of the specimens demonstrated a damage development processes that continued up to very large displacements with relatively small load reductions after initial failures. Compressive loading applied to the skin side demonstrated a severe degree of load reduction and specimens deformed to a lesser extent before complete failure. Isogrid plates loaded on the skin side absorbed more energy than those loaded on the rib side, and isogrid mechanical performance was superior, when compared to a square-grid configuration. Energy absorption values ranged from 38.97 J to 81 J measured at maximum displacements.

Finite element based research on triaxial braided composites was previously investigated by several authors. Li et al. [32] studied the 2D transverse impact response of a triaxial braided composite model developed using the non-linear explicit FE code LS DYNA. The unit cell consisted of six sub cells and their associated material properties where specified at the shell element integration points to simulate the braid architecture. Simulations indicate that failure was initiated by cracking of the matrix between specified sub cells, where only bias fibers existed. Additionally, a smaller braid angle led to significant nonlinearity in the mechanical response. A relationship between composite material properties and braid angle demonstrated weaker mechanical properties in the transverse direction. Littell et al. [33] developed a macroscopic FE based analytical model to analyze the impact response of triaxial braided carbon fiber composites under transverse tensile loading. The unit cell of the braided composite was modeled as a series of shell elements, where each element was modeled as a laminated composite. Zhang et al. [34] experimentally investigated the transverse impact behaviour of a four step three dimensional carbon/epoxy rectangular braided composites under quasi-static and drop weight tests. The observed force/displacement response indicated that linear behaviour takes place before peak load was obtained. The initial linear response was a result of elastic deformation of the carbon fiber tows and resin. Mechanisms of failure were identified as resin cracking and local indentation damage on the front surface of the specimens.

3 RESEARCH OBJECTIVES

It is important to understand the mechanical response of foam filled braided tubes under uniaxial and transverse loading conditions for employment as novel energy absorbing devices in numerous industrial sectors. Literature associated with this research is scarce. Limited research exists on aluminum foam filled braided stainless tubes functioning in uniaxial tensile loading. No publication exists regarding foam filled braided tubes under transverse loading. A thorough understanding of the behaviour, failure mechanisms, and mechanical response, in both deformation modes, is required to exploit the advantages these structures offer. To achieve this, a unique testing apparatus that provides long stroke capabilities for continuous tests due to their extension characteristics will be designed to fully test the capabilities of these specimens. The testing apparatus proved to be beneficial in obtaining the necessary information. The following details within this thesis present complete experimental analysis:

1. Specimens, of long or short lengths will be tested until catastrophic failure without the interruption of the system.
2. The testing device will be designed with interchangeable mounting locations.
    a. The apparatus will provide continuous tests while eliminating significant manpower, induced errors, and loss of energy absorbed upon unloading.
3. Study the observed differences in the results; identifying deformation mechanisms, what they are, and how they influence the response.
4. Investigate what braid/foam density and geometry combinations give the best balance of energy absorption as a function of foam core crushing and braid tube elongation.
5. Provide details at critical points in the mechanical response by utilizing the high speed cameras to capture the structure's motion during the deformation process and associate the time based images with the force/displacement response.
6. Validate Cheng's theoretical model from the obtained experimental radius versus length relationship results captured through high speed image analysis.

4 DESIGN OF THE TESTING APPARATUS

This chapter provides detailed description of the testing apparatus and the finite element analysis methodology used to complete the design. The engineering prints of the main assembly, individual members of the assembly and of the fixtures are provided in Appendix A. The press code for a down stroking machine is illustrated in Appendix B. The finite element analysis results of the testing apparatus are provided in Appendix C.

4.1 Introduction

By means of the testing machine, Figure 1, continuous tests until catastrophic failure without any interruption to the system provided experimental data and complete understanding of the deformation mechanisms of foam filled braided stainless steel tubes. Integrated within this testing apparatus, high speed cameras and data acquisition system were able to provide experimental evidence and capture the tows motion as well as the interaction effect between braided tube and metallic foam core. The behaviour of the failure mechanisms were visually studied through high speed recordings, which has never been considered in previous research. The experimental results gathered will aid in developing and validating a finite element model to predict the complex behaviour of the tows.

The process of loading/unloading/reloading was not considered in this thesis. Previous research conducted by Powell [15] utilized such an approach as a result of testing apparatus (crosshead displacement) restrictions. In addition, this loading and unloading induced set up complications, altered the behaviour of material, and influenced the energy absorption capability of the assembly. Furthermore, the positioning of the foam core would shift during handling between loading and unloading once again altering the test specimen. Thus, these restrictions limited Powel [15] to fully exploit the advantages these specimens can offer.

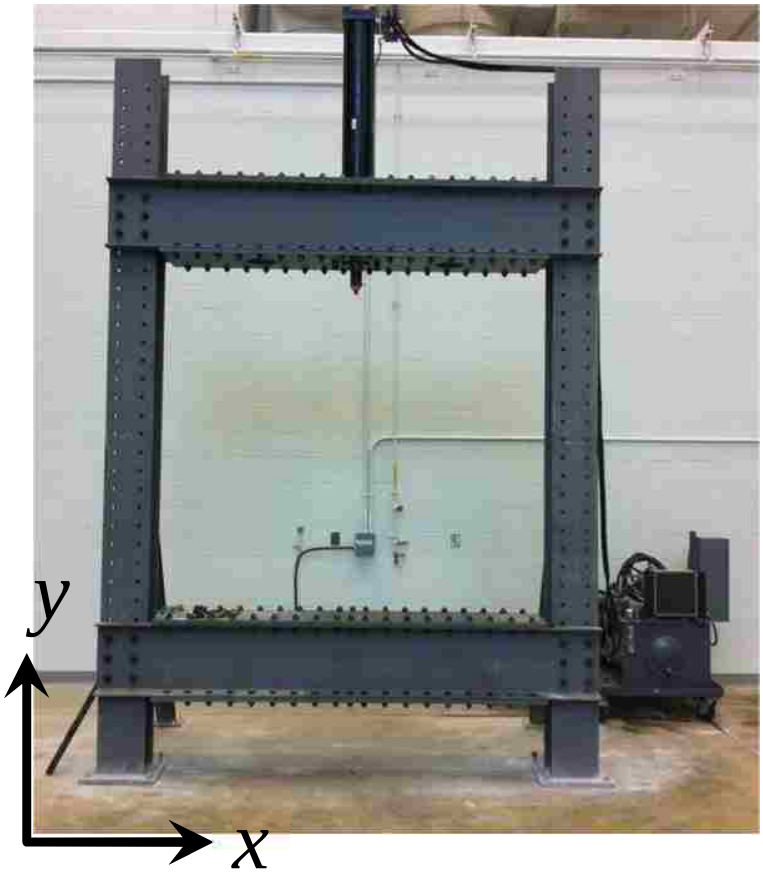

Figure 1: Front view of the testing apparatus.

The testing machine is thus an important tool both for research and for advanced product development. The following sections describe the function of the testing machine and structural analysis of the frame. Subsequent chapters provide detailed results and discussions from typical uniaxial and transverse tests of foam filled braided stainless steel tubes.

4.2 The testing machine

The testing device is a set of moveable steel reaction columns, channels, and plate stiffeners that can be assembled in almost limitless configurations and used in conjunction with other testing apparatus to apply loads to almost any structural component or subassembly. This large-scale testing machine can apply loads up to 250 kN in tension and 300 kN in compression on specimens up to 1.2 m in length. The

machine has an overall height of 3.96 m (13 ft.) with 2.24 m (7.35 ft.) of usable clearance between the columns. The summary on the capacity and main parameters of the machine is presented in Table 1.

Table 1: Geometrical properties of connections

Structural Member	Section	ASTM Designation	Flange Angles (in.)				Web Angles (in.)	
			Gage	Length	Bolt Spacing (y-direction)	Bolt Spacing (x-direction)	Gage	Length
Column	W10 x 77	A36	0.87	10.2	4	5.52	0.54	10.62
Column	W4 x 13	A36	0.35	4.00	NA	NA	0.28	4.16
Beam	C15 x 40	A36	0.65	3.52	4	5.52	0.52	15.00
Bolt/nut/washer	7/8	A325	NA	NA	NA	NA	NA	NA
Bolt/nut/washer	3/4	A325	NA	NA	NA	NA	NA	NA

An iterative design process was used to determine the column and beam size as well as the bolt patterns. During the process, the effective von Misses stresses and displacements were closely monitored and compared to the yield stress of the material (ASTM A36). The iterative process involved FE simulations of an axial loading condition (load applied at mid-span of the ¼ model) in order to find a section best suited for the applications of this research and for future considerations. For the column W10 x 68, W10 x 77, and W10 x 89 were considered; and for the beam C12 x 25, C12 x 30, C15 x 25, C15 x 30, and C15 x 40 were considered. During each iterative simulation run, there was no variation in mesh density, bolt hole size, and material model.

The rate of loading on the specimen is controlled through valves that control the motion of the actuator. Testing can be conducted at predetermined rate of pressure application. This permits the application of a constant pressure of any value up to 20.68 MPa (3000 psi) for an indefinite length of time. This option is useful for testing of materials in plastic deformation under a constantly sustained load. The hydraulic cylinder is mounted through the rectangular/circular through holes in the upper portion of the machine's plate stiffeners. The plate stiffeners act as support for structural integrity against bending moments. The upper portion – lower plate stiffeners is outfitted with three hollow circular cross section cutouts to support offset loading. Note that offset testing was not conducted

for this experimental work. Figure 2 illustrates the testing machine and the available room for the test specimen below the fully extended cylinder. A circular clamping device

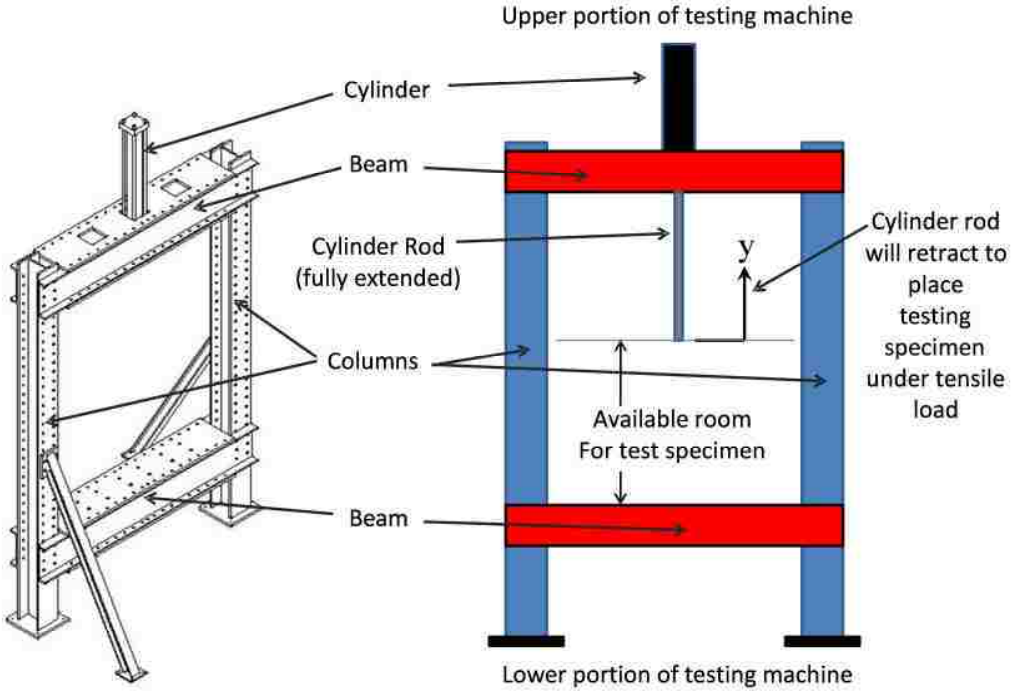

Figure 2: Isometric and front view of testing machine.

constrains the motion of one of the ends of the braided tube to testing machine at the lower support beam. An additional clamp will be fastened to the translating end of the cylinder rod through adapter plates which will clamp the other end of the braided tube. Tensile testing of the tubes will be completed by retracting the rod of the hydraulic cylinder in the positive *y*-direction as shown in Figure 2. The length of the testing specimen is approximately 600 mm (23 in) and the clamps which will fasten the braided tube to the testing machine have a length of approximately 200 mm (8 in). The estimated clearance between the lower beam and the free tip of the rod is estimated to be approximately 1 m (40 in).

The upper axial fixture, illustrated in Appendix A2.1, is threaded into the piston rod. The piston rod extends as the oil from the accumulator travels through the lines. When the cylinder reaches its starting position, a 2 x 4 inch lumber is used to prevent the cylinder

from further extension due to gravity. According to the press safety standards code Z142-02 (Appendix B); the system was redesigned with integrated flow controls and counterbalance valve in order to safely operate in vertical rod down orientation. The modern pumping unit with pressure, flow, and power control supplied by Checker Industrial Ltd. uses Parker hydraulic cylinders manufactured by Parker Hannifin Corporation. The unit Series 2H piston pump, with a model number of PVP16304R212, has the ability to achieve a maximum pressure of 3,000 psi (210 bar). A 7.5-hp, 3-phase, 1800 rpm motor powers the pumping unit. The maximum flow rate can be as high as 26.49 L/min (7 gpm) and can retract the main cylinder with velocity of 2201.67 mm/min (~86.68 in/min) and extend with velocity of 1452. 63 mm/min (~57.19 in/min); bore of the main cylinder is 152.4 mm (6 inches), rod diameter 88.9 mm (3.5 inches), and area of the main cylinder is 18238.67 mm^2 (28.27 $inch^2$). Once the set-up is complete, manual operation of the valve is required to retract the cylinder.

The maximum pressure of the accumulator is 3000 psi. At operating pressure of 2000 psi yields an extend force output of 252 kN. However, system flow rate does not affect the force; it only affects the speed of the cylinder. For the current operating pressure, the system flow rate is set to 4 gpm, this indicates an operating retract speed of approximately 20.97 mm/s (0.826 in/s).

4.3 Structural analysis

In order to analyze the static behaviour of the structure with respect to effective stress and maximum deflection, we refer to three different constructive solutions of the machine's frame: (1) uniaxial, (2) offset, and (3) transverse loading. Figure C1 provides an overview of the loading on all three conditions. The structural members have bolted connections that permit to fix structural members and hydraulic cylinder. In more details the main structure consists of base plates welded to the columns with bolt on supports applied to concrete floor.

4.4 Finite element model selection

A three-dimensional FE model was simulated under LS-DYNA™ version 971s R4.2 on a personal computer with dual-core 2.4 GHz Intel processors with 8 GB of dynamic random access memory based on selection of the model that most closely reproduces the actual assembly and connection behaviour. The connection is modeled using constrained nodal rigid body (CNRB). The CNRBs are a convenient way to connect similar mesh areas or element type (shell-to-shell). Kinematic coupling constraints are imposed between nodes which are joined to CNRBs. This type of constraint is appropriate for finite strain and rotation in small displacement analysis. In brief, the FE model can be described as follows.

The mesh of the connection model is represented using all major connection components: column, beam, plate stiffeners. These components are independent from (i.e. not jointed to) each other and interactions are taken into consideration whenever they come in contact with each other. The CNRB for each bolt hole, on the beam and column or column and plate stiffeners, act as a rigid bolt connection. Contact interactions are considered between the column and beam flanges, beam upper and lower flange contact with upper and lower plate stiffeners by employing a single CONTACT_AUTOMATIC_SINGLE_SURFACE algorithm available in LS-DYNA™. This contact definition considers shell thickness from the mid-plane and is worthy for quasi-static simulations where minimal deformation occurs. A penalty based formulation for contact was invoked by applying 0.25 static and 0 dynamic friction coefficients. An elastic material model (referred to as MAT_ELASTIC within LS-DYNA™) was selected for the columns, beams, and plate stiffeners. The material model assumes isotropic behaviour and the effective stress follows the von-Mises definition. Refer to Figure C2 in Appendix C for details. With regards to transverse loading case, a rigid material definition was applied to the cubic blocks tied to the discrete spring. A nonlinear elastic translation material model, MAT_SPRING_NONLINEAR_ELASTIC, was selected for the discrete spring acting as the braided tube. A force/displacement response was provided (used from experimental findings).

Discretization of the structure involved generating an IGES file from a CAD model designed in Catia v5 R20, for the ¼ model structure. The IGES file provided and served as a means of developing the geometry of the FE model. The completed FE model of the structure consisted of 41,806 nodes and 40,436 elements, 40,436 of which are shell type elements. Explicit numerical integration was used in this analysis and fully integrated shell element (ELFORM 16) was selected as the element formulation for all of the individual components making up the testing apparatus due to faster computing time. In this FE model, all shell elements were meshed on the physical mid-surface plate of the structure. Thus, the initial contact interpretations will be minimized.

The discretization of the individual structural members was carried out using HyperMesh v11 software. An element size of 10 mm x 10 mm was used where discontinuities did not occur and 9 mm x 5 mm was used where circular hole discontinuities occurred throughout the model. This was necessary to ensure an accurate calculation of the stress distribution resulting from the stress concentration caused by the circular hole discontinuity.

4.5 Boundary conditions and loading

Numerical analyses were performed following the experimental build-up and loading method described in section 4.3. One quarter model was used for numerical analysis considering structural symmetry. This aids in limiting the computation time and providing model simplicity. In these, (1) two beams are symmetrically connected to the column's flanges, (2) the ends of these beams are constrained through CNRBs, and (3) at the upper portion of the machine, two plate stiffeners (upper and lower) are symmetrically and horizontally aligned (*xy* plane), Figure C3; they are connected to the two beams; lower portion of the machine contains the identical members arranged in similar fashion. The large mid through hole located on the machine's upper portion – lower plate stiffeners contains four small surrounding symmetrical through holes (where the hydraulic cylinder would normally mount). In the symmetrical model, loading is applied on one of the four holes where a central node was created and tied through CNRBs. The circular mesh created around the through hole, its outer diameter reflects the

outer diameter of the corresponding structural washer used. The central node ties (through CNRBs) to the entire nodes existing in the area between the inner diameter of the through hole and outer diameter of the structural washer. This aspect is essential in order to take into account the displacements and stresses in that zone and determine the stiffness that is strongly needed in order to correctly size and analyze the mechanical members.

Figure C3 demonstrates the boundary conditions applied to the FE model. To enforce connection symmetry, all nodes of the column's web (*z* direction) viewed from the *xy* plane have been restrained displacement in the direction of *x* and restrained rotation in the direction of *y* and *z*. In the *xy* plane, all nodes in the column's footing (along the web and flange) have been restrained in all translational and rotational directions. Along the edges of symmetry (*y* direction), all nodes on the plate stiffeners' edge have been restrained displacement in the direction of *x* and restrained rotation in the directions of *y* and *z*. Along the edges of symmetry (*x* direction), all edge nodes on the plate stiffeners and beam have been restrained displacement in the direction of *y* and restrained rotation in the directions of *x* and *z*. To produce only vertical reaction forces, the plate stiffeners and beam end support are assumed as pin. These restraints allow the quarter model structural members to move upward so that corresponding forces generated from the prescribed force can be distributed among the connection assemblages.

The analysis was carried out for the axial loading condition where the load generated by the hydraulic cylinder is at mid-span of the testing apparatus. This loading condition was deemed worst case scenario and was considered as minimum load criteria that needs to be met for size selection of the columns and beams. A downward force of 87.5 kN was applied on the upper portion-lower plate stiffeners and an upward force of 87.5 kN on the lower portion-upper plate stiffeners as depicted in Figure C1(a). Upward and downward forces in the FE model were applied to best simulate the nature of the kinematic constraints of the aluminum foam filled braided structure, symmetry of the model, and to avoid any singularity problems in the FE model analysis due to the concentrated force. This type of loading results in a tensile force introduced on the plate stiffener by

employing vertical load in mid-section of the machine. A safety factor of 1.8 was considered in the design given that this testing apparatus will be used for future experimental research that will require high loads. Table 2 summarizes details associated with the loading conditions applied to the FE model.

Table 2: Summary of the loading, symmetry and FE model

Loading condition	Load (kN)	Full model load (kN)	Symmetry used	FE Model
Axial	87.5	350	Yes	1/4
Offset	87.5	350	Yes	1/4
Transverse*	NA	NA	Yes	1/4

*Boundary prescribed motion was applied for this type of loading.

4.6 Results

In the design of the testing machine, it is of great interest the static displacements and stress responses. The present design was mainly aimed at providing strong machine stiffness and for this reason the results are studied with reference to stresses and displacements and are presented in terms of ultimate state response, for all the examined load cases. The results are summarized and presented in Table 3.

Table 3: Finite element stress and displacement results of the testing device

Loading Condition	Bolt Connection	Effective Stress (MPa)				Maximum Deflection of System (mm)			
		Column	Beam	Plate Stiffener	Max Stress	Column	Beam	Plate Stiffener	Resultant
Axial	6	62.36	243.44	238.23	243.45	0.39	0.82	1.11	1.11
Offset	6	112.25	234.91	222.35	234.91	0.51	0.72	1.02	1.02
Transverse	6	111.94	23.78	7.26	111.94	0.06	0.02	0.01	0.06

Figures C4(a) illustrates the resultant displacement profile of the quarter model at the ultimate state in the uniaxial loading case. It is observed that little or no deformation occurs in both upper and lower column-beam connection and the loading area. The maximum horizontal displacement of the column in the (y direction) is approximately 0.394 mm which occurs at mid-span. Total resultant displacement of the machine

assembly is approximately 1.11 mm which was noted to occur at mid-span at the loading region. Individual member displacements were observed to be below 1 mm and were deemed negligible. The corresponding von Mises stress distribution is presented in Figure C5. The figure reveals that comparatively greater effective stress, approximately 243.44 MPa, is generated mainly in the upper portion – lower plate stiffeners and beam's lower flange, which are in compression. Also, smaller stress develops in the beam and column which are under the elastic range, excluding the stress concentration area near the bolt holes in beam web and column flange as illustrated in Figure C6 (b) and (c). Furthermore, most of the stress accumulation in the column, on the order of 63 MPa, was observed to be at the lower column-beam connection, Figure C6 (a). These are due to the upper and lower bending moments and column restraints of the model which are located at the lower portion of the column.

Figure C7 depicts the von Mises stress distribution at upper and lower bolt pattern connection which confirms that eccentric loading results in a non-uniform stress distribution in a shear type connection. Because of the moment, each bolt is subjected to a force acting perpendicular to a radial line from the centroid to the bolt pattern. It is assumed that the magnitude of the force in a bolt due to the moment load is proportional to its distance r from the centroid.

Figure C8 illustrates the deformation configuration of the eccentric column-beam connection at the ultimate state in the offset loading condition. In this case the moment arm is reduced by approximately 537.54 mm (21.16 in.), this equates to higher stress and deflection for the column member. Correspondingly, column nearly doubled in stress which was observed to be 112.25 MPa and deflection increased by 57% to 0.689 mm compared to axial loading case. However, effective stress of the entire frame decreased to approximately 234.91 MPa due to an observed lower stress on the plate stiffeners which was noted at 222.35 MPa. Correspondingly, the machine's resultant displacement, as noted in Figure C4(b), also slightly decreased. Plate stiffeners stress reduction of approximately 16 MPa is largely due to transfer of the stress to the column rather than plate stiffeners. Moreover, less resistance and stronger stiffness in the beam prevents

further deflection. Furthermore, it was observed from Figure C9, that the upper and lower column-beam eccentric connections were similar in magnitude and stress distribution. The stress distribution is higher on the inboard side of the connection with maximum localized magnitudes of approximately 69 MPa.

Figure C4(c) illustrates the resultant displacement of the structural frame in the transverse loading condition. A nonlinear elastic spring with a given stiffness and force/displacement load curve representing an empty braided tube from [15] and [16] was modeled to monitor the local stress distribution of the transverse fixture attachment on the column. An assumption is made such that stress generated from transverse tension of the braided tube would equally transfer through the transverse fixture to the column. As such, one end node of the discrete element was rigidly attached to the column and the opposite node was constrained through extra_nodes_node to a slave rigid block. Displacement driven boundary_prescribed_motion_rigid option was used on two blocks, i.e. slave and master bodies. Considering the column, noted stress magnitude was approximately 111.94 MPa compared to offset loading condition. However, the stress contours were highly localized at the connection area of the transverse fixture, as depicted in Figure C10, compared to axial and offset conditions which were observed to be more distributed over the surrounding region. The lower beam experienced concentrated stress, approximately 31.9 MPa, at the upper right bolt connection (*yz* plane) due to a reaction bending moment from the loads generated by the discrete element. The observed stress, approximately 18.1 MPa, in the beam is transferred to the upper flange – first bolt connection (*xy* plane) as well to the upper plate stiffeners at the lower portion of the machine. No stress or displacements were noted for the upper portion of the machine.

Table 4: Mechanical properties for ASTM A36 and A325 structural steel

Material	**Density (kg/m^3)**	**Young's Modulus (MPa)**	**Poisson's Ratio**	**Yield Stress (MPa)**	**Ultimate Stress (MPa)**	**Elongation (%)**
A36	7830	210	0.28	248	441	21
A325	7830	210	0.28	660	585	21

Numerical examination of the maximum effective stress values, illustrated in Table 3, shows that maximum effective stresses are below the yield stress of the material and hence it is considered as safe under the aforementioned applied load of 87.5 kN. Table 4 provides the mechanical properties for ASTM A36 structural steel material used for the testing apparatus. It is observed from Table 3 that the effective stress for the column in the axial and offset loading conditions are much lower than the effective stresses for the beam and plate stiffeners. As a result, the size selection of column, beam, and plate stiffeners collectively were below 248 MPa yield stress of A36 structural steel.

4.7 Conclusion

It has been presented an approach to design a structure that is to be constructed in a single prototype. Criteria of strength, stiffness and versatility in the choices of geometry of structural members were adopted. Due to the specific functions of the machine, that is to test mechanical specimens, the design was oriented by the assumption that the structure stiffness is an essential requirement.

5 EXPERIMENTAL TESTING AND ANALYTICAL MODELING METHODS

The experimental and analytical testing methods employed in this research consisted of five major components: design of the testing apparatus, compressive testing, uniaxial testing, transverse testing, and theoretical model validation. The process is depicted in Figure 3. The testing apparatus is devoted to test on specimens in different conditions of load, displacement and deformation. The machine was considered as a system of load frame, hydraulic system, and instrumentation devices for monitoring testing procedures, Chapter 4. Section 5.2 provides detailed procedure on quasi-static compressive testing of aluminum foam cores. To assess the deformation mechanisms and validate the theoretical model developed by [16], quasi-static uniaxial testing was completed on empty and foam filled braided tubes. Section 5.3 addresses details associated with the testing process. Similar to uniaxial testing, within section 5.4, transverse testing method of empty and foam filled braided tubes is provided. Section 5.5 presents the test set up for theoretical model validation.

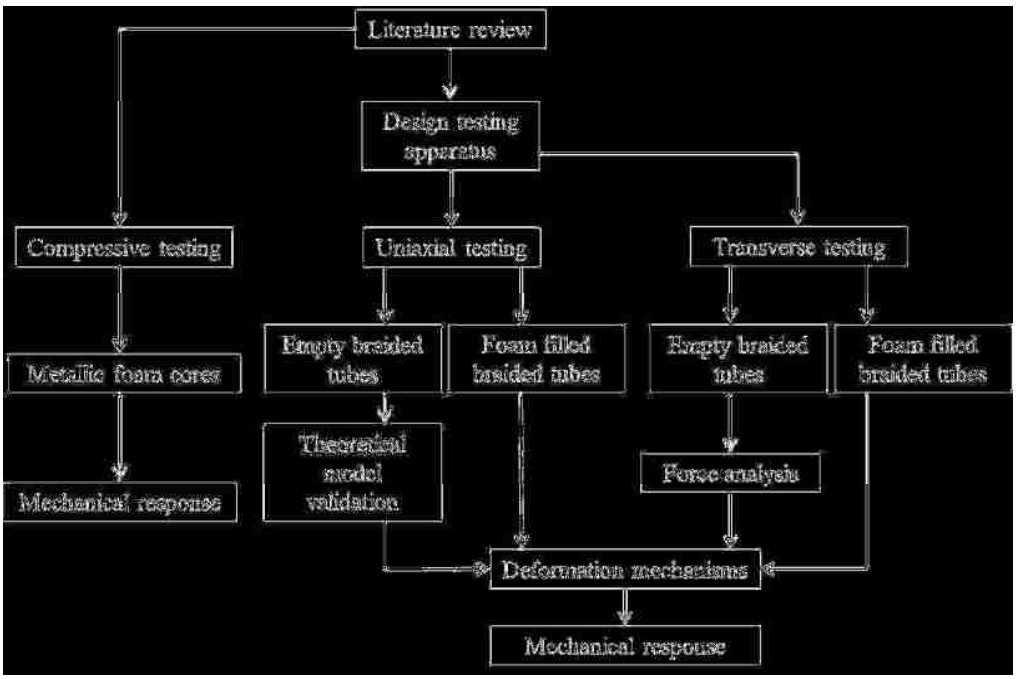

Figure 3: Flow chart of the testing program.

5.1 Overview of the testing methods

The braided tube utilized within this research was woven from American Iron and Steel Institute (AISI) 304 stainless steel wires having a diameter of 0.51mm. Each tow consisted of a bundle of 8 wire strands, 48 tows were woven around the circumference of the tube in a standard "2 over/2 under" geometrical configuration. The nominal tube diameter provided by the manufacturer was 64.5 mm. The mechanical properties of AISI 304 stainless steel are listed below in Table 5.

Table 5: Mechanical properties of the AISI 304 stainless steel braid wire

Young's Modulus (GPa)	Yield Strength (MPa)	Tensile Strength (MPa)	Elongation (%)	Density (kg/m^3)
193	241	586	55	8027

Vertical displacement of the end portion of the hydraulic actuator, for both uniaxial and transverse deformation process, was measured using an Acuity AR700-50 non-contact laser displacement transducer having a 1280 mm range and a frequency response of approximately 9 kHz. The load was measured using a 220 kN PCB strain gauge based (model #1204-03A) load cell mounted to the translating hydraulic ram and integrated into the upper uniaxial fixture. Signals from the displacement transducer and load cell were measured through National Instruments NI9215, which has a sampling capacity of 100 kHz/channel and a NI9237 module (4 channel, 16 bit, analog input module), with a sampling capacity of 50 kHz, respectively, both of which were contained within a CompactDAQ NI9274 chassis. A data sampling rate of 2 kHz was applied for all tests.

High speed image data, capturing the deformation process of the uniaxial and transverse loading process, was obtained through use of a Photron SA4 high speed, high resolution camera which was synchronized with the CompactDAQ system and associated modules which obtained displacement and load measurements. Time synchronization was completed through a custom developed LabVIEW program and a National Instruments NI9401 transistor–transistor logic (TTL) module which provided a high speed voltage signal to commence and stop the Photron camera consistent with the initiation and

termination of data acquisition from the other two modules. Photographs were obtained at a rate of 60 images per second at a resolution no less than 640 by 640 pixels^2 (for the majority of the testing a resolution of 896 by 896 pixels^2 was implemented). A shutter speed of 1/1000 s was utilized and ample lighting was provided by two ARRI 750 watt lights. Time differences between the transducer data and the high speed images were observed to be no greater than 1 ms over the duration of the test. Acquisition of the testing data was stopped following completion of the event.

5.2 Compressive testing

The closed cell aluminum foam used throughout this research was provided by Cymat Corporation and was fabricated using the Cymat foam casting process also known as the air bubbling or melt gas injection technique. The process involves the addition of ceramic particles or magnesium oxides to enhance viscosity of the liquid metal to be foamed. Furthermore, the molten metal is foamed by gas injection (air/nitrogen) using rotating air injection shafts to generate fine gas bubbles and distribute them homogenously in the melt. References [36] and [37] provide a good overview of the melt gas injection process which results in the fabrication of aluminum foam panels. The addition of ceramic particles stabilizes the air bubbles that are injected in the melt. Previous studies completed by Degischer [38] and Xia et al. [39] have demonstrated that the tensile and compressive properties of aluminum foams can be altered through the use of different additives such as SiC or Mn elements. The alloying of aluminum foams is a very useful process as it may allow for the production of foams with mechanical properties tailored for a specific application. No additional alloying elements were investigated within this research. Cymat [40] indicates that the aluminum foam can exhibit density, average cell size and cell wall thickness ranging from 0.069 g/cm^3 – 0.54 g/cm^3, 3 mm – 25 mm, and 50 μm – 85 μm, respectively. Specific to the foam considered within this research, no characterization of the foam microstructure was completed.

Uniaxial compressive testing of foam specimens was completed to assess the engineering stress/strain behaviour of the metallic foam material. Testing was completed on six different aluminum foam specimens using a hydraulic Tinius Olsen compression testing

machine. The testing machine was equipped with a linear voltage differential transformer (LVDT) having a range of 150 mm. Depending upon the range of loads experienced within a compression test for a given specimen, a strain gauge based load cell (PCB model numbers 1204-03A (220 kN), 1204-02A (90 kN), or 1203-03A (9 kN)), having a suitable measurement range, was implemented. A National Instruments CompactDAQ system, containing the NI9215 and NI9237 modules, were used to measure signals from the displacement and load transducers. Data was acquired at a rate of 2 kHz.

Each compression test was completed with a nominal crosshead speed of 1.04 mm/s. Loading of the metallic foam occurred on the specimen faces which were parallel to the continuously cast direction (in a direction consistent with the height of the specimen). Details of each specimen tested, including foam density and observations obtained from testing are provided in Table 6, for specimens utilized in circular cores, and Table 7, for specimens extracted from foam utilized in rectangular cores. The identification system of the tests specimens follows the convention $\alpha\phi$-$\beta\boldsymbol{\rho}$-CC for circular core geometries, where α is either 'H' or 'L' implying High or Low diameter (ϕ), β is either 'H' or 'L' implying High or Low foam density ($\boldsymbol{\rho}$), and 'CC' indicates Circular Core. For the rectangular prism core geometries, the specimen identification follows the convention $\gamma\boldsymbol{\rho}$-RC, where γ is either 'H' or 'L' implying High or Low foam density ($\boldsymbol{\rho}$), and RC indicates Rectangular Core geometry.

Table 6: Compression specimen (circular cores) information and observations

Specimen ID	Test #	Density (kg/m^3)	Specimen Geometry(mm)		Load Cell Range (kN)	Elastic Modulus (MPa)	Plateau Stress (MPa)	Densification Strain (%)
			Diameter	Height				
Hϕ-Hρ-CC	1	488.80	84.18	26.18	90	151.29	3.98	33.3
	2	489.98	84.07	26.12	90	139.77	4.01	37.2
	3	474.29	84.29	26.21	90	120.53	3.99	34.1
Hϕ-Lρ-CC	1	315.09	83.24	25.11	90	43.83	0.73	38.6
	2	317.71	83.44	25.11	90	27.50	0.47	40.1
	3	293.86	83.39	25.45	90	39.61	0.50	39.2
Lϕ-Hρ-CC	1	439.47	79.69	26.58	220	158.61	3.15	38.9
	2	451.60	79.49	26.04	90	92.79	2.96	40.4
	3	439.18	79.41	25.91	90	97.60	2.80	39.2
Lϕ-Lρ-CC	1	331.51	79.09	25.05	90	29.48	0.58	35.1
	2	330.46	78.51	25.36	90	14.75	0.41	44.4
	3	348.31	78.46	25.19	90	8.60	0.32	25.2

Table 7: Compression specimen (rectangular cores) information and observations

Specimen ID	Test #	Density (kg/m^3)	Specimen Geometry(mm)		Load Cell Range (kN)	Elastic Modulus (MPa)	Plateau Stress (MPa)	Densification Strain (%)
			Diameter	Height				
Hρ-RC	1	489.68	37.936	24.53	90	201.54	3.80	28.1
	2	477.55	37.256	24.52	90	182.32	3.30	29.7
	3	453.25	36.814	24.71	90	139.81	3.10	30.1
Lρ-RC	1	162.38	64.004	24.21	90	11.18	0.36	43.3
	2	169.42	62.736	24.24	90	16.55	0.40	42.9
	3	163.17	63.738	24.58	90	7.44	0.36	41.2

Five measurements for each critical dimension (length, width, and height for rectangular cores, and diameter and height for circular cores) were taken and an average value was computed and used to calculate the density of the aluminum foam specimen. Compression testing was completed until engineering strains ranging from approximately 0.7 to 0.9 were obtained.

5.3 Uniaxial testing

5.3.1 Empty stainless steel braided tubes

Tensile testing of the tube specimens was completed using the testing machine as illustrated in Figure 4a. Prior to testing, each end of the braided tube was inserted into an annular clamp and secured by means of a conical wedge with a preload of approximately 27 kN. Figure 4b illustrates the specimen test geometry, containing the braided tube, upper and lower fixtures, and the annular clamp. This test geometry was consistent for specimens which were also filled with aluminum foam. The geometry of the annular clamp and conical wedge is identical to structures used in the studies within [15] and [16] and are illustrated in Figure 4c. The test set up consisted of inserting the annular clamps into the upper and lower adapter plates, attached to the testing machine, such that the flat face of the annular clamp was in contact with the flat face of the adapter plate. No mechanical fasteners were used to attach the braided tube to the testing machine. This approach ensured appropriate alignment of the braided tube.

Testing was conducted on tubes having lengths approximately equal to 830 mm, 720 mm and 330 mm. Three tests were conducted for each length. Table 8 indicates the specific lengths of braided tube for each test. The specimen ID, noted in Table 8, corresponds to the specimen identification that uses one of two abbreviations, NFT and NFVT, with the former implying “No Foam Tensile” and the latter implying “No Foam Verification Tensile”. The NFVT specimens were used to ensure consistent findings from the work presented and those found in references [15] and [16].

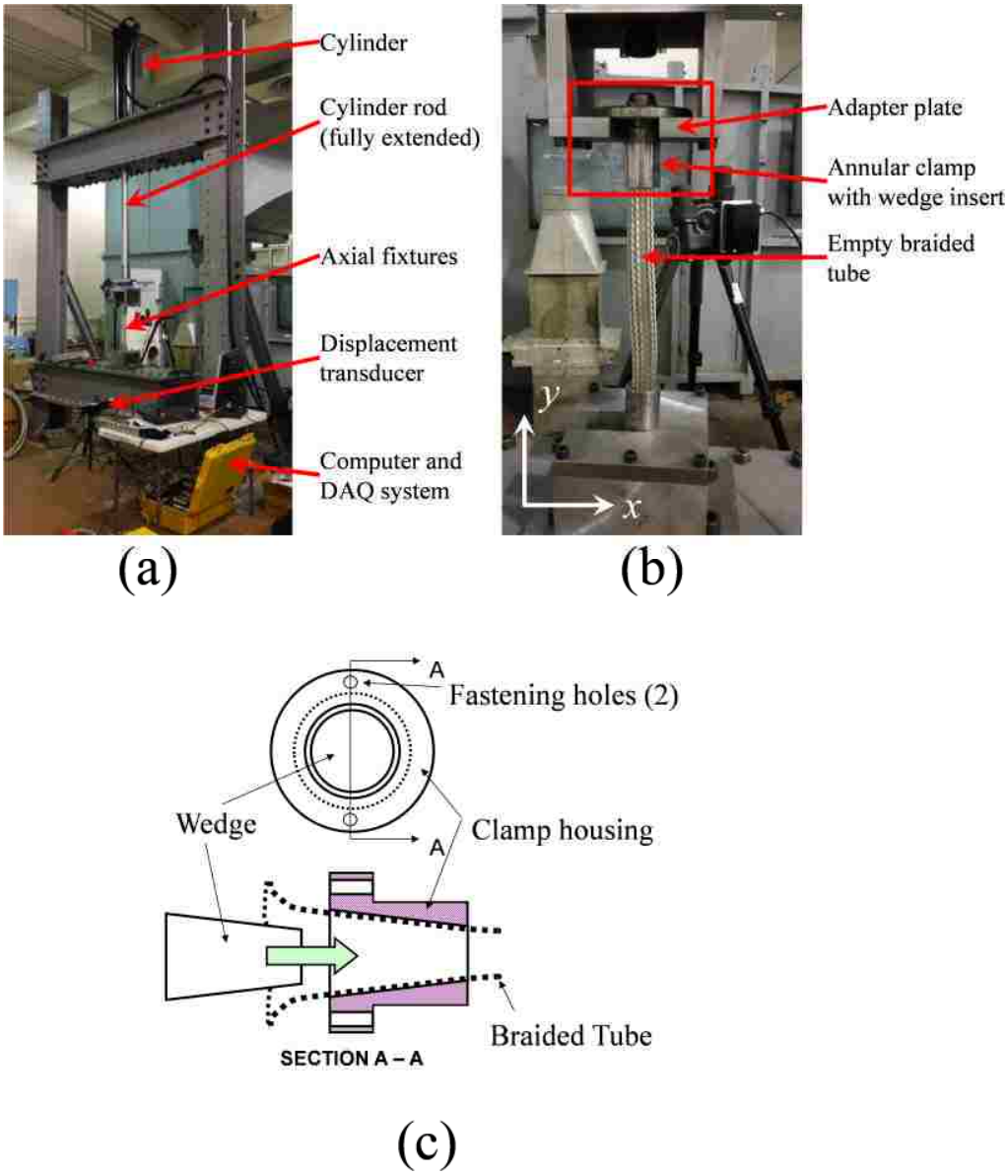

Figure 4: Testing apparatus setup (a) entire system, (b) tested geometry and (c) annular clamp device.

Table 8: Empty specimen information pre- and post-test

Specimen ID	Test #	Tube Length (mm)	Average Force (kN)	TFE (%)	Total Energy Absorbed (kJ)	SEA (kJ/kg)
NFT	1	811	35.413	71.40	8.15	9.89
	2	840	34.272	70.40	8.48	9.93
	3	843	33.424	67.90	8.57	10.00
	4	710	35.516	71.40	8.18	11.34
	5	701	32.743	67.70	8.22	11.54
	6	746	29.908	60.20	8.02	10.58
NFVT	1	359	30.468	61.70	4.71	7.72
	2	278	34.566	67.90	4.80	7.87
	3	331	30.846	61.80	4.34	7.11

5.3.2 Aluminum foam filled stainless steel braided tubes

Braided tube specimens were cut from tubular wrap using conventional cutting shears. Each specimen was cut to a desired length which allowed for approximately 330 mm between each annular clamp and a total tube mass of approximately 610g. The aluminum foam cores were cut into either a cylindrical or rectangular geometrical configuration. For a given foam filled braided tube specimen, the core geometry was either a rectangular prism or a cylinder. The density of the cores varied; however, they were classified into high and low density for each geometrical configuration. The densities of the foam cores are detailed in Tables 9 and 10 with a naming convention consistent to previous; however, the abbreviation ‘FFT’ is used to imply a braided tube which is “foam filled tensile” under tensile loading.

Table 9: Circular core foam filled specimen information pre- and post-test

Specimen ID	Test #	Tube Length (mm)	Core Geometry(mm)		Average Force (kN)	TFE (%)	Total Energy Absorbed (kJ)	SEA (kJ/kg)
			Diameter	Height				
FFT-Hϕ-Hρ-CC	1	335	84.471	26.024	18.95	55.49	7.46	5.61
	2	329	83.578	25.920	20.11	55.52	8.24	6.05
	3	326	84.922	26.626	17.42	49.99	7.97	5.91
FFT-Hϕ-Lρ-CC	1	345	84.412	25.408	4.48	9.91	8.10	7.36
	2	329	84.386	24.990	3.07	6.58	8.27	7.51
	3	349	84.198	25.100	4.52	10.08	8.20	7.50
FFT-Lϕ-Hρ-CC	1	338	79.848	26.044	26.2	75.12	6.30	5.54
	2	337	79.938	25.846	22.5	67.18	8.14	7.02
	3	333	79.936	25.994	22.5	71.55	6.46	5.52
FFT-Lϕ-Lρ-CC	1	332	79.412	23.340	6.93	15.44	8.13	7.76
	2	329	78.696	25.382	5.96	13.65	7.52	7.63
	3	326	78.988	25.256	6.12	13.61	8.34	8.42

Table 10: Rectangular core foam filled specimen information pre- and post-test

Specimen ID	Test #	Tube Length (mm)	Core Geometry (mm)			Average Force (kN)	TFE (%)	Total Energy Absorbed (kJ)	SEA (kJ/kg)
			Width	Length	Height				
FFT-Hρ-RC	1	337	75.65	250.41	77.12	9.65	23.54	10.81	5.39
	2	322	75.65	250.41	77.12	13.23	32.38	10.02	5.13
	3	324	75.47	250.09	78.98	11.69	28.18	9.92	4.67
FFT-Lρ-RC	1	330	75.03	250.06	76.82	3.11	1.57	9.01	8.03
	2	336	75.74	250.07	76.87	3.27	1.24	8.95	7.98
	3	335	75.31	250.04	75.49	3.43	2.08	8.08	7.94

The rectangular foam prisms were constructed using three smaller segments obtained from an aluminum foam panel using the water jet cutting technique. An adhesive with the trade name “PL Premium” by LePage was used to secure the segments together. Appropriate curing time was allocated after application to ensure the adhesive was applied properly. Any sharp edges were removed using a band saw to avoid braid damage upon insertion. The rectangular core was orientated within the braided tube such that the

tensile loading direction was parallel to the continuous casting direction (the direction defined by the height of the specimen).

The circular cores were comprised of ten smaller circular cylinders (pucks), also cut from a foam panel, using the water jet cutting technique, and were assembled in the same manner as the rectangular cores. For the circular cores, the interfaces between each puck were perpendicular to the tensile loading direction. Correspondingly, the tensile loading direction, for the circular core specimens, was perpendicular to the continuous casting direction (the direction defined by the height of the specimen). Specific core and braided tube geometry, prior to testing, are detailed in Tables 9 and 10.

Insertion of the foam core into the braided tube was completed manually by two individuals. The braided tube was compressed to an extent such that the aluminum foam core, when inserted, slid into the compressed tube with ease. When compressing the tube, the angle between the tows increased resulting in an increase in the diameter of the tube. After insertion, the tube was released from its compacted condition. Careful attention was applied to ensure the position of the foam core was centered within the length of the tube. Once the assembly process was completed, the upper and lower ends of the braided tubes were inserted into the annular clamps and transferred to the top and bottom adapter fixtures attached to the testing machine. Prior to uniaxial testing, the length of each aluminum foam filled structure was verified by measuring between the clamp points. Figure 5, graphically illustrates the assembly process of the rectangular core foam filled braided tube. The assembly process for the cylindrical foam core was consistent with this process.

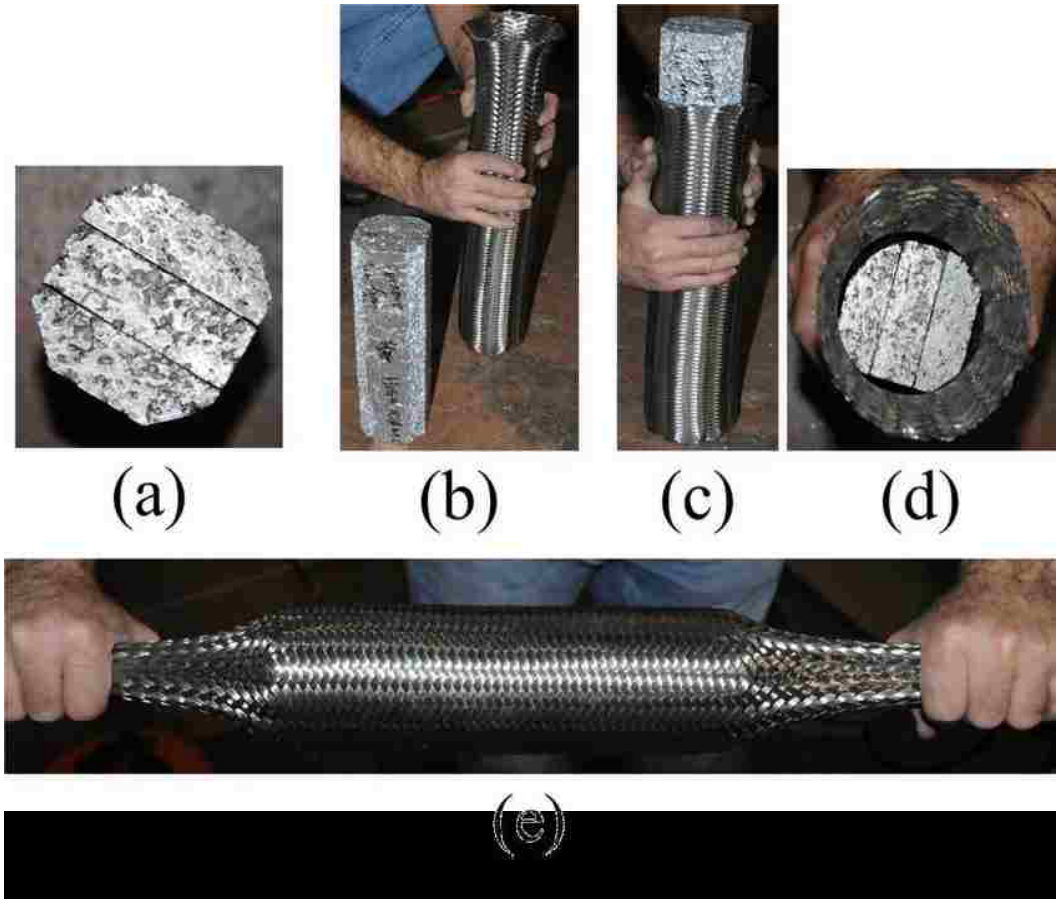

Figure 5: Assembly process of the rectangular high density aluminum foam filled braided tube.

5.4 Transverse testing

5.4.1 Empty stainless steel braided tubes

Two unique fixtures were required to complete the transverse testing. Each side of the 300 kN capacity machine used an identical transverse fixture assembly which consists of two side plates and one adapter plate. Figures A4.1 – A4.3 in Appendix B illustrate complete details associated with this fixture. Two side plates, 25.4 mm thick and 1.143 m in length, were fastened to both columns of the testing machine. The adapter plate is 269.748 mm x 165.1 mm with a thickness of 25.4 mm. This plate contained a 33.02 mm radius semi-circular cutout such that the annular clamp [15] mates and fastens to it. Furthermore, a second centre fixture mounted on the translating hydraulic cylinder which

consisted of two vertical plates and one horizontal plate. Figures A5.1 – A5.4 in Appendix B illustrate detailed engineering prints associated with this fixture. The upper horizontal plate contains a 20.65 mm through hole which allows a 19.05 mm nominal diameter bolt to be fastened to the conical wedge insert incorporated into the annular clamp. Lastly, a 76.2 mm diameter circular solid bar is bolted between the vertical plates; upon upward vertical displacement of the hydraulic cylinder the bar contacts the braided tube at mid span as illustrated in Figure 6.

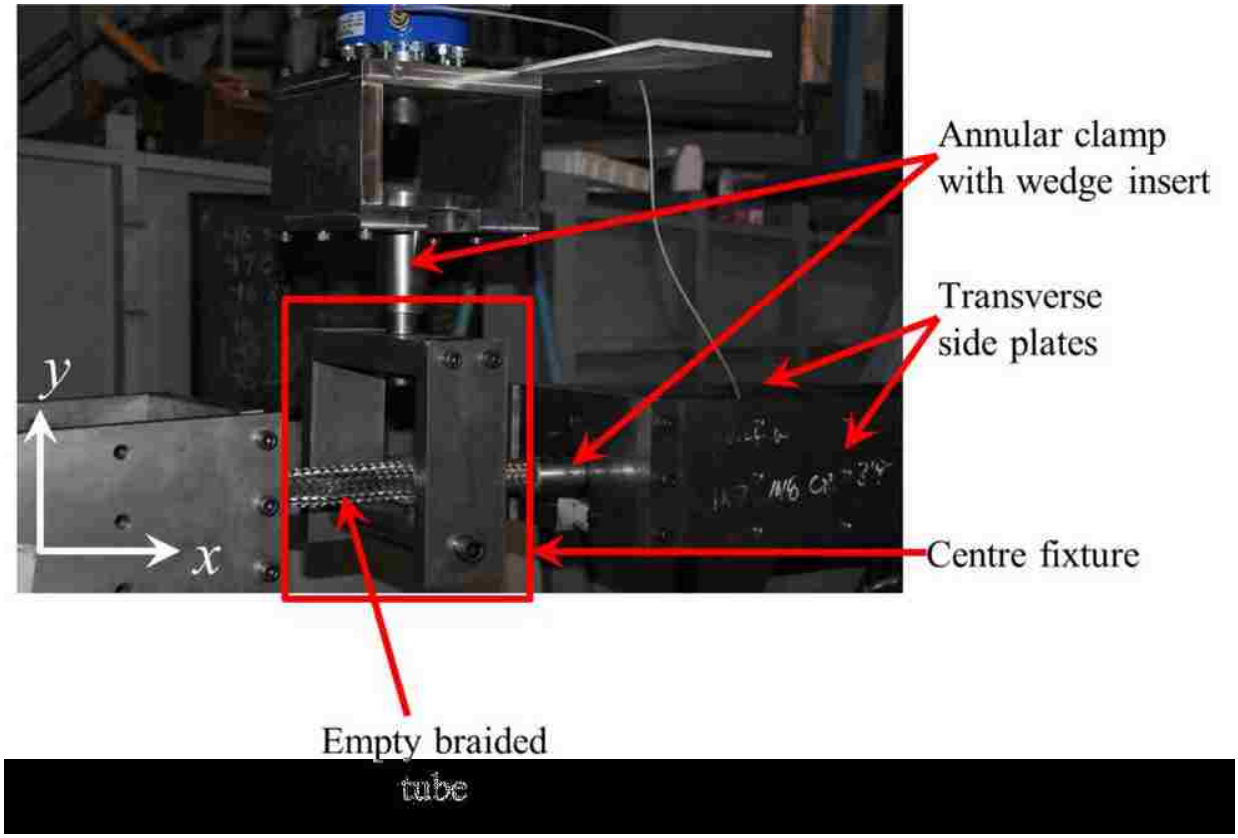

Figure 6: Transverse test setup of untested empty braided tube.

Prior to testing, one end of the braided tube was inserted into an annular clamp and secured by means of a conical wedge with a preload of approximately 33 kN. The test set up procedure consisted of first lowering the hydraulic cylinder such that it is in centre axis position aligned with that of the side plates as illustrated in Figure 6. After the crosshead was aligned, one end of the braided tube/annular clamp is fastened to the

adapter plate. Once fastened, the free end of the braided tube is fed through the center fixture and is inserted into the opposite side annular clamp and secured by a conical wedge with the same preload, which then is fastened to the opposite side adapter plate. The adapter plate/annular clamps are fastened by a series of four (4) 6.35 mm nominal diameter bolts and one (1) 9.525 mm nominal diameter bolt to prevent bending and for structural security. The distance between both conical wedges, representing the loaded region of the braided tube, was approximately 330 mm. Preparation of the centre fixture consisted of inserting the annular clamp to the upper adapter plate, attached to the testing machine, such that the flat face of the annular clamp was in contact with the flat face of the adapter plate. This approach ensured appropriate alignment of the braided tube.

Table 11 provides the specific lengths of tube for each test. The specimen ID, noted in Table 11, corresponds to the specimen identification that uses NFTT abbreviation with former implying “No Foam Transverse Tensile”.

Table 11: Empty specimen information pre- and post-test

Specimen ID	Test #	Tube Length (mm)	Average Force (kN)	FE (%)	Total Energy Absorbed (kJ)	SEA (kJ/kg)
NFTT	1	329	12.59	29.6	2.67	5.86
	2	329	12.24	29.9	2.37	5.21
	3	329	12.13	30.8	2.46	5.41
	4	329	11.95	28.9	2.46	5.41
	5	329	13.00	30.7	2.57	5.65

5.4.2 Aluminum foam filled stainless steel braided tubes

Specimen preparation involved measuring a total length of 420 mm using a tape measure and manually cutting the braid wires using steel wire cutters. The usable braid length between annular clamps was measured to be approximately 330 mm once fully assembled. The total mass of the tube was measured to be approximately 455 g. Two foam architectures were employed in this experimental research study namely circular (cylindrical) or rectangular for a given foam filled braided tube test. The inner metallic foam cores were prepared in a similar procedure to the foams cores used for uniaxial

testing. Several foam densities were tested and were classified into either high or low density for each geometrical configuration. The densities of the foam cores are detailed in Tables 12 and 13 with a naming convention consistent to previous; however, the abbreviation 'TFFT' implies "transverse foam filled tested".

Table 12: Circular core foam filled specimen information pre- and post-test

Specimen ID	Test #	Tube Length (mm)	Core Geometry (mm)		Average Force (kN)	FE (%)	Total Energy Absorbed (kJ)	SEA (kJ/kg)
			Diameter	Height				
TFFT-Hρ-CC	1	330	79.93	26.27	19.64	41.6	6.19	5.63
	2	330	79.79	26.27	20.17	37.7	6.84	6.39
	3	330	80.06	26.23	24.12	35.4	8.08	6.42
TFFT-Lρ-CC	1	330	79.57	25.21	17.44	24.2	6.16	6.15
	2	330	79.11	25.42	15.82	23.4	5.41	5.29

Table 13: Rectangular core foam filled specimen information pre- and post test

Specimen ID	Test #	Tube Length (mm)	Core Geometry (mm)			Average Force (kN)	FE (%)	Total Energy Absorbed (kJ)	SEA (kJ/kg)
			Width	Length	Height				
TFFT-Hρ-RC	1	330	75.13	250.33	78.65	19.61	33.6	7.44	3.65
	2	330	75.47	250.04	78.97	23.11	33.3	9.13	4.32
	3	330	75.13	250.33	78.65	20.16	30.5	7.80	3.82
TFFT-Lρ-RC	1	330	75.54	500.00	76.24	13.71	18.6	4.72	4.29
	2	330	75.36	500.06	76.71	11.50	16.4	4.03	3.74
	3	330	75.03	250.01	78.21	10.16	16.2	3.51	3.41

The rectangular foam cores tested under transverse loading were consistent (in terms of geometrical architecture and assembly process) with the prisms used under uniaxial loading. Note, once the braid/foam assembly was mounted within the testing machine, its orientation was parallel to the floor.

Similar to rectangular cores, circular cores were also assembled and oriented parallel to the length of the braided tube. Ten smaller cylindrical pucks also cut by the water jet

cutting process were used to form a circular cylinder. After full insertion into the braided tube, the interfaces of the circular cores between each puck were parallel to the transverse loading direction. Correspondingly, the transverse loading direction, for the circular core specimens, was parallel to the continuous casting direction (the direction defined by the width of the specimen). Specific core and braided tube geometry, prior to testing, are detailed in Tables 12 and 13.

Process handling of the foam core into the braided tube is identical to the process described in section 5.3.2. However, prior to transverse deformation, length measurements were taken between clamp points and five diameter measurements were taken along the length respectively. The assembly process for the rectangular and cylindrical foam prisms were consistent with the ones mentioned in section 4.3.4.

5.5 Braid motion analysis for theoretical model validation

5.5.1 Tow motion analysis – validation of the unit cell equations

To investigate the radius/extension behaviour of the braided tube prior to tow lockup, post-processing of the digital images acquired with the high speed camera was completed using the digital image analysis software, ProAnalyst [41]. The goals of these analyses were to determine tube radius as a function of tube elongation prior to tow lockup, in the case of an empty braided tube, and validate the unit cell equations which are used in the analytical model developed by Cheng et al. [16].

Two regions along the radial direction (*x*-axis direction) were identified for post-test analysis. These regions were carefully selected such that they were not near the vicinity of the annular clamps but near the centre of the braided tube where the largest diameter occurred when compressed. Figure 7a illustrates the locations of these two regions. Lines 1 and 2, which were selected for linear tracking in only the direction of the line, were defined such that they were orientated with the x-axis/radial direction. Within ProAnalyst a “thresh derivative” search type was utilized with a “black to white” image operation having a threshold value of 30. The black to white image filter, applies a binary operation to the pixels within the original image. For the 256 scales of gray within a grayscale

image, the threshold value will be used to distinguish between white and black. Any pixel with a value less than the threshold value will be set to black and the remaining pixels will be set to white [41]. It was discovered that this binary image filter technique allowed for clear definition of the edges of the specimen in the image analysis process, so that the radius could be determined as a function of tube elongation. Figure 7b provides the configuration of the braided tube and the associated tracking points to determine the radius prior to tow lockup. This tracking was completed manually for each photograph obtained during the tow motion, which resulted in approximately 180 images to be analyzed.

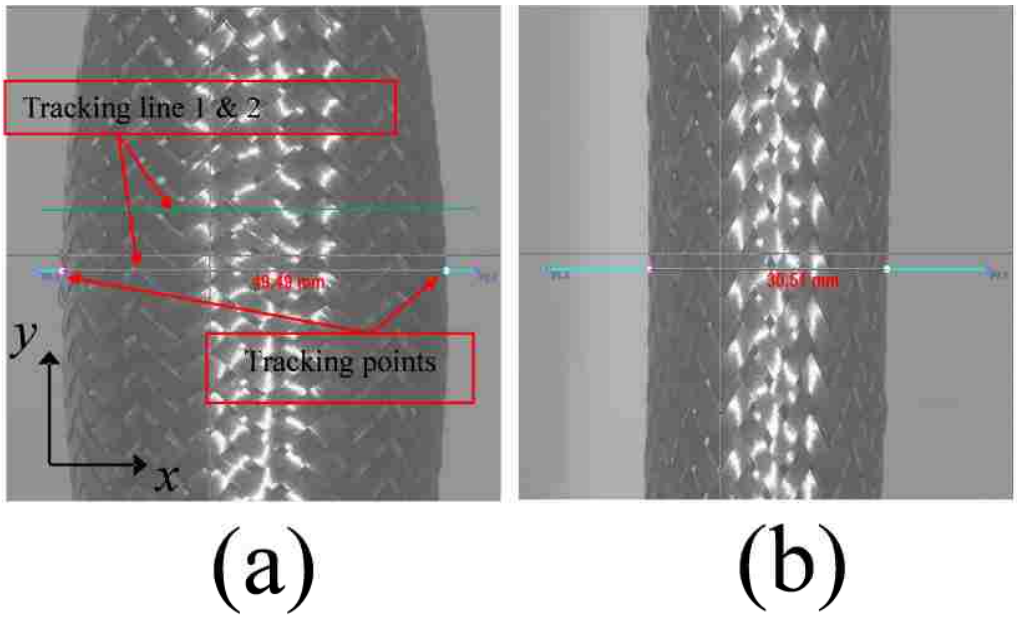

Figure 7: Tracking region of empty tube through ProAnalyst at (a) initial state and at (b) extended tube prior to tow lock up.

6 EXPERIMENTAL AND ANALYTICAL OBSERVATIONS AND DISCUSSION

Experimental results obtained in this research proved to be valuable for investigating failure mechanisms such that braid tube/foam density and geometry combinations provided ample data for optimization and compatibility in future works.

6.1 Experimental compressive observations and discussion for aluminum foams

The engineering stress/strain responses from six different configurations of foam cores with densities ranging from 162.38 kg/m^3 to 489.98 kg/m^3 are presented in Appendix D. Furthermore, mechanical material behaviour, such as elastic modulus, plateau stress and densification strain are presented in Tables 6 and 7.

At low strains, the foam deforms elastically and deformation is controlled by cell wall bending and/or compression. This region is defined as the linear/elastic region which was observed to occur over a range of strains of 0 mm/mm to 0.025 mm/mm for both circular and rectangular cores. It is evident from Tables 6 and 7 as well as Figures D1-D6 in Appendix D that high density foam cores responded with a higher plateau stress ranging from approximately 3.0 MPa to 3.99 MPa while low density cores exhibited plateau stresses ranging from 0.4 MPa to 0.6 MPa. A detailed discussion regarding variability between specimens relating to elastic modulus, plateau stress, and densification strain is presented in Chapter 7. All specimens exhibited an upper yield strength which was followed by strain softening upon further loading.

The linear elastic region is followed by a region where material strength does not vary significantly with further material straining; a negligible or minor degree of strain hardening occurred in this regions known as the ‘plateau’ region. The range of strains where this is observed is dependent upon the foam density. Low density specimens exhibited a plateau region within the range of strain from 0.03 mm/mm to 0.4 mm/mm and high density specimens illustrated a plateau region within strains of 0.026 mm/mm to 0.30 mm/mm. Deformation in this region is highly localized at the cellular level and

results from buckling and brittle crushing of cell walls and the formation of plastic hinges at the cell walls. These deformation mechanisms propagate throughout the specimen. Since the deformation is localized, large oscillations in stress occur due to the repetitive nature of the process of cell collapse. Consequently, the extent of each region is a function of foam density. This deformation characteristic, in addition to variation in cell size and cell size distribution, results in a small amount of strain hardening within the plateau region. However, the plateau stress is estimated as an average value of strength of the material within this region of strain during loading.

Material densification occurs once a notable increase in the slope of the stress/strain material response is observed. Tables 6 and 7 provide estimated densification strains for each specimen tested.

6.2 Experimental observations and discussion for uniaxial tests

6.2.1 Tensile response for empty braided tubes

Figures 8 and 9 illustrate the force versus displacement and energy versus displacement responses of empty tube specimens of lengths approximately equal to 330 mm and 700 mm. Additionally, Table 8 presents the average (tensile) force observed during testing, as well as the tensile force efficiency (TFE), total energy absorbed (TEA), and the specific energy absorption (SEA). Note that the average force is computed as the area bound by the force/displacement curve and the abscissa, normalized with respect to the total displacement observed within each test. The TFE is computed as the average force normalized with respect to the maximum force observed in a given test and is presented in equation 1. The rectangular rule is utilized to calculate the total energy absorbed which is the area bound by the force/displacement curve and the abscissa throughout the entire displacement domain as defined by equation 2. The SEA, calculated from equation 3, is the total energy absorbed by a structure divided by its mass. Three tests were completed for each length of tube and consistent mechanical behaviour was observed for all three tubes of identical length.

$$TFE = \frac{F_{avg}}{F_{max}} = \frac{\frac{1}{\delta_{max}} \cdot \int_0^{\delta_{max}} F_z \cdot d\delta}{F_{max}} \quad (1)$$

$$TEA = E_{total} = \sum_{i=2}^{N-1} P_i \left(\frac{\delta_{i+1} - \delta_{i-1}}{2} \right) \quad (2)$$

$$SEA = \frac{TEA}{m} \quad (3)$$

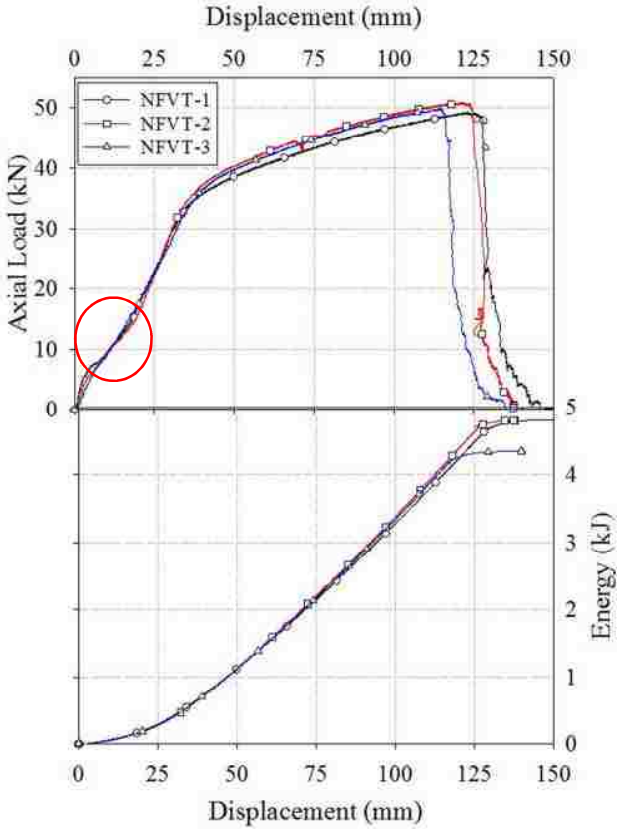

Figure 8: Force/displacement and energy/displacement responses for empty braided tubes of length 330 mm.

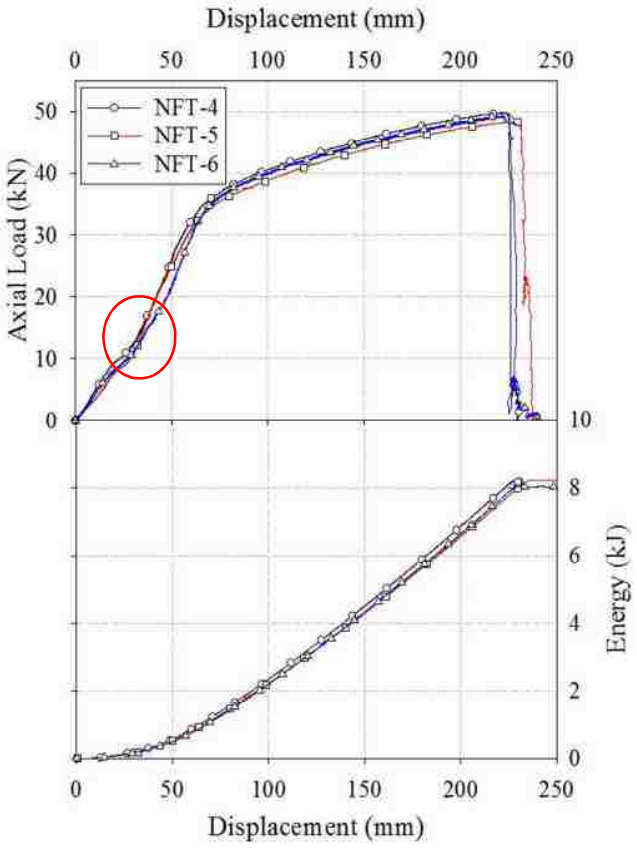

Figure 9: Force/displacement and energy/displacement response of empty braided tube of length 700 mm.

Observations indicate that a linear response of the tubes was noted up to loads approximately equal to 8.5 kN and 10 kN for the 330 mm and 700 mm length tubes, respectively. Further loading induces a minor degree of nonlinear behaviour resulting from the lateral bending of contacting wires on the exterior of the engaging tows (circled regions in Figures 8 and 9). Figure 10 illustrates the wire deformation at neighbouring tows when this response was observed to occur. A similar response was observed in [20] where “a dry braid”, in similar reference to empty braid, after axial tensile extension the tows lockup and the stiffness of the braid increases dramatically. The circled regions in Figures 8 and 9 emphasize the localized wire deformation. The localized plastic hinge at these locations results in material wire stack up and a minor alteration in the slope of the force/displacement response. Subsequent to this deformation characteristic, a linear

response is further observed in the braided tube as a result of the elastic deformation occurring within the remainder of the wires forming the tows of the braided tube. It was observed that the stiffness within the linear region following the nonlinear response was not consistent with the stiffness prior to the nonlinear tube behaviour. Similar to the findings from the current investigation, the structures considered in [17] exhibited unique mechanical responses which were dependent upon the deformation mode. In the work by Cox and Davis [17], unique deformation characteristics, and the corresponding mechanical response, of composite chain links occurred as a result of extensive matrix damage followed by lockup of chain links. Additionally, Muralidhar [18], who considered reinforced epoxy composites under tensile and compressive loading, observed micro-cracking of the fibre matrix due to flax yarns' immediate contact with each other. Lateral bending of fibres caused rupture which resulted in a reduction of strength. This deformation characteristic is consistent to the findings in this study; however, the brittle behaviour of the fibres resulted in fracture rather than plastic deformation observed in the current investigation.

A comparison of the force/displacement response of the two different lengths of tubes, illustrated in Figures 8 and 9, indicate that in the first 10 mm of axial extension, the force/displacement response of the NFVT tubes was stiffer than the NFT specimens. This finding is expected as for any tube modeled as a simple linear spring the stiffness of the spring is inversely proportional to its length. Correspondingly, shorter length tubes (NFVT specimens) will exhibit a higher degree of stiffness. After 10 mm of axial extension, the force/displacement relationships with different lengths vary significantly, which results from the collective local plastic deformation occurring within the tows of the braided tube. The deformation phenomenon satisfies the inverse relationship between the structure length and stiffness.

A significant variation in the force/displacement response was noted to occur at approximately 34 kN tensile load. This load was observed to be independent of the original tube length. An almost linear force/displacement response was observed between 34 kN and 50 kN tensile loads. At approximately 50 kN load, failure of individual wires

within the tows were observed to occur. This resulted in a progressive failure mode of the braided tube.

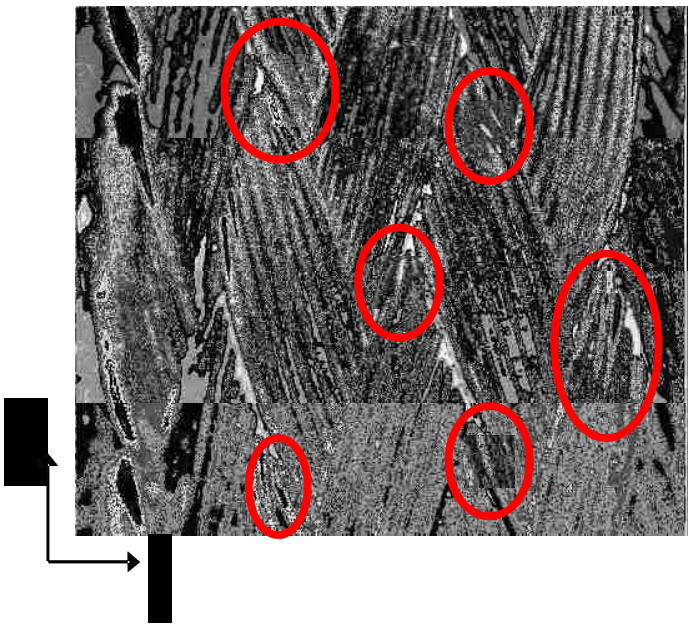

Figure 10: High speed camera image of wire tow scissoring, lateral bending and stack up.

The average SEA of the empty tubes within groups NFT and NFVT were found to be 10.55 kJ/kg and 7.57 kJ/kg, respectively. When normalized with respect to the initial length of the specimen the NFT and NFVT exhibited SEA per unit length of 13.75 kJ/(kg·m) and 23.76 kJ/(kg·m) indicating a dependency of the SEA with respect to length of the braided tube. The values of SEA found for the empty braided tubes are similar to those obtained for the chain composites developed by [17].

6.2.2 Tensile response for circular foam filled braided tubes

Figures 11 and 13 present the force versus displacement and energy versus displacement responses of the circular core aluminum foam filled braided tubes. Photographs depicting the axial deformation process of the high density core for specimen 1 are illustrated in Figure 12 and photographs for low density core for specimen 2 are illustrated in Figure 14. Annotations in Figures 11 and 13 correspond to the images in Figures 12 and 13, respectively.

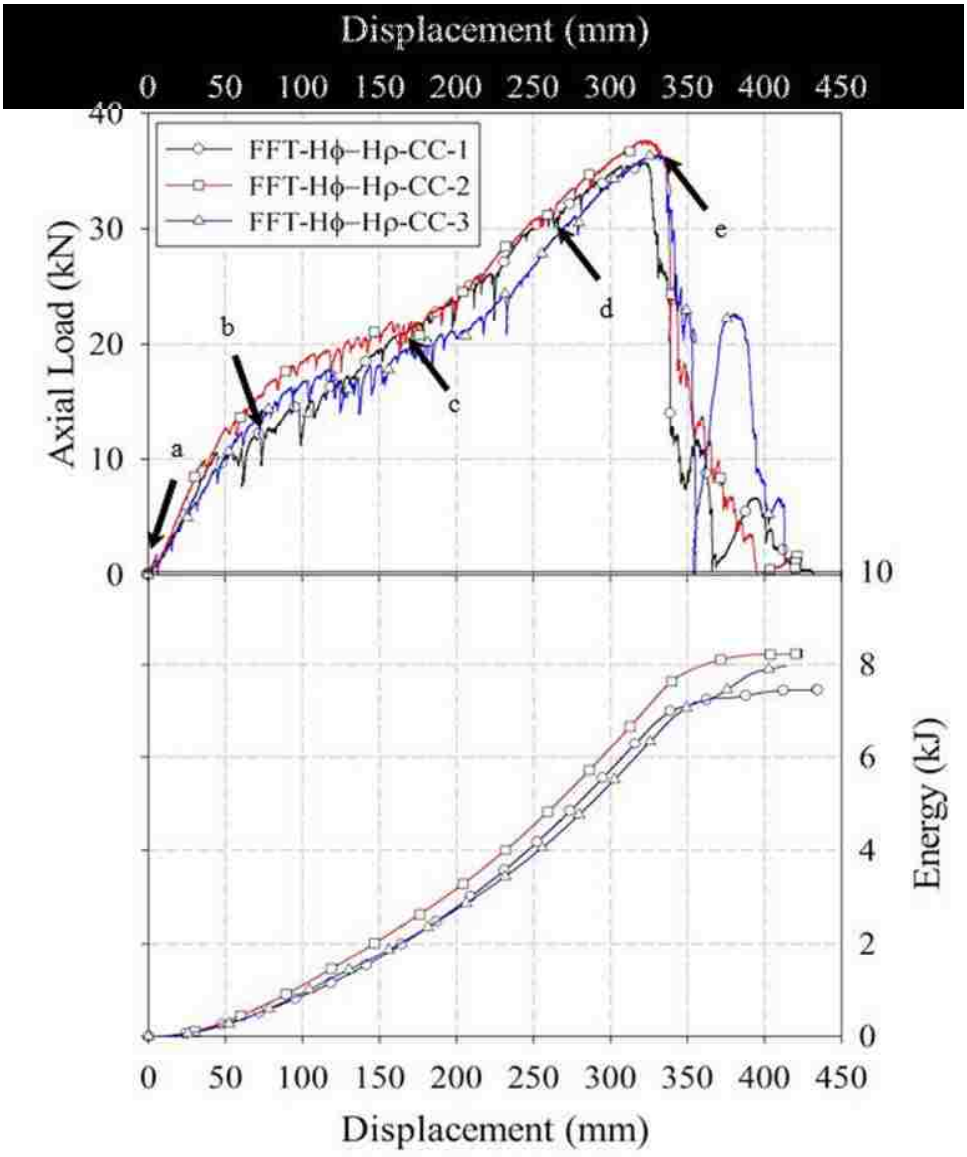

Figure 11: Force/displacement and energy/displacement responses for circular core, high diameter high density foam filled braided tube.

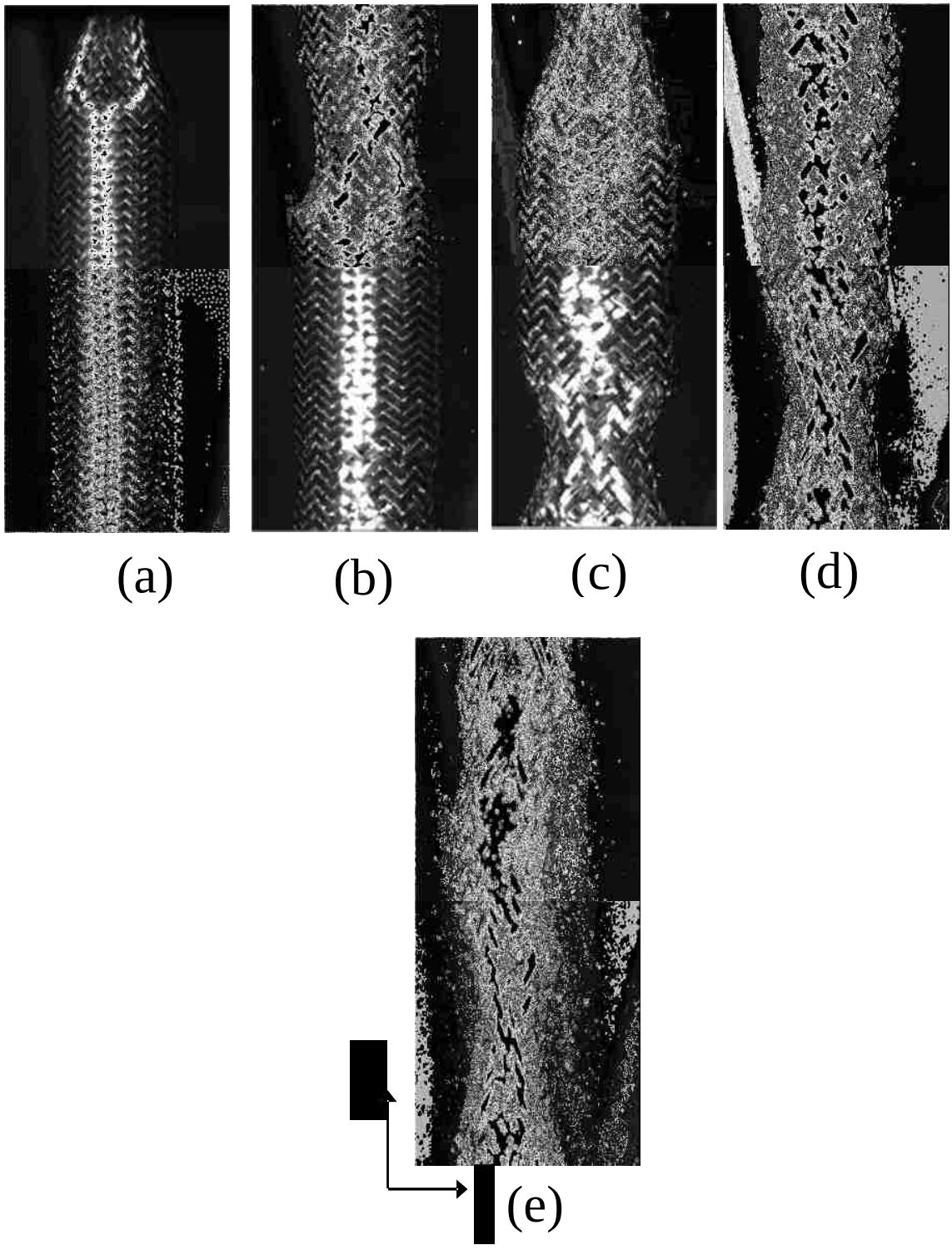

Figure 12: Photographs illustrating the axial tensile deformation process of the high foam circular core braided tube for specimen 1.

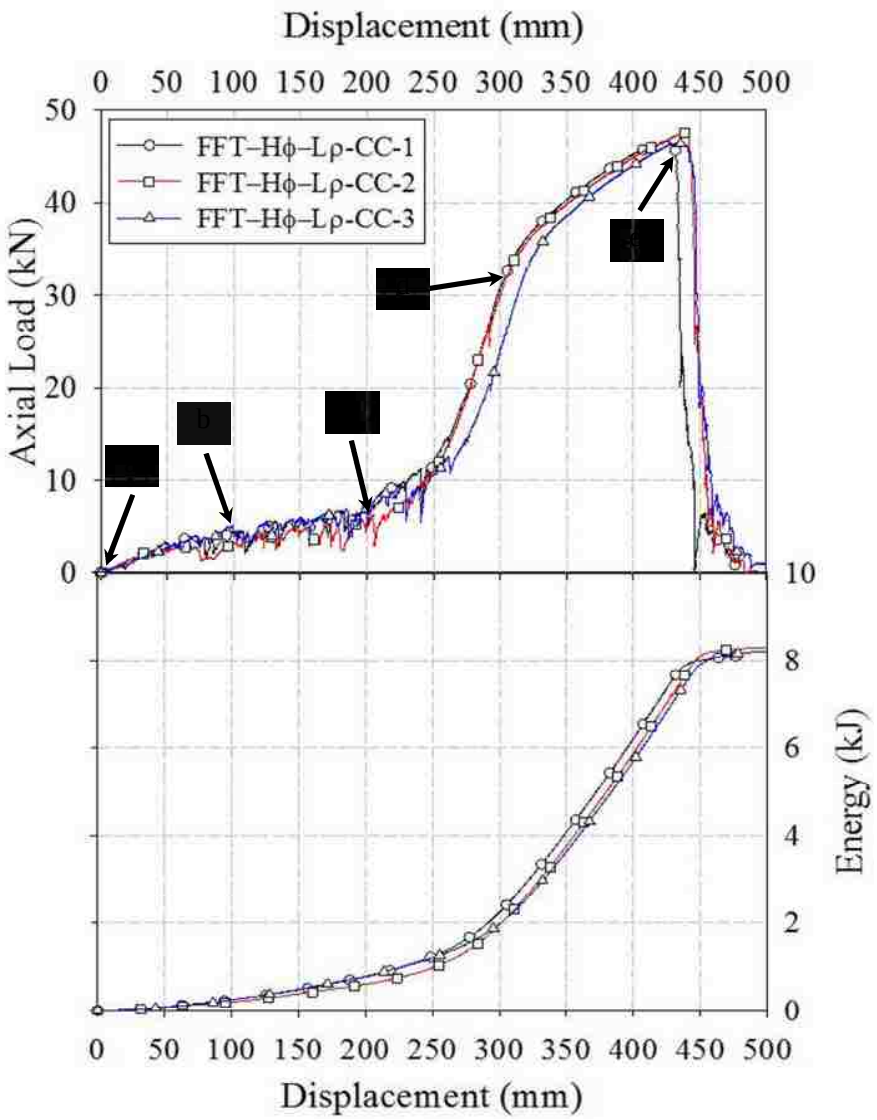

Figure 13: Force/displacement and energy/displacement responses for circular core, high diameter low density foam filled braided tube.

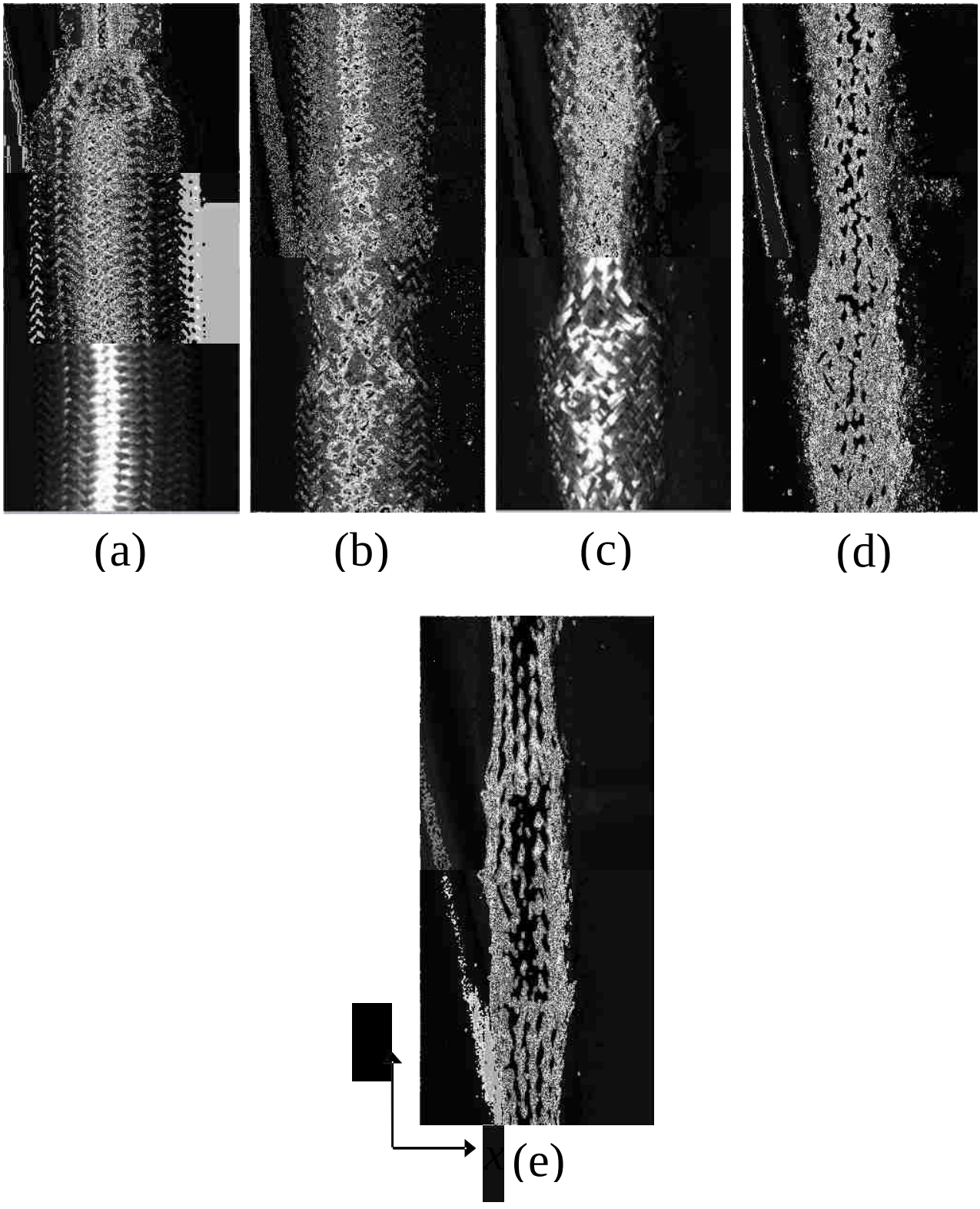

Figure 14: Photographs illustrating the axial tensile deformation process of the low foam circular core braided tube for specimen 2.

Photographs of the axial deformation process illustrate that immediately following the application of tensile load the tows became close packed and crushed the foam core. Significant crushing of the foam core was noted to occur at displacements greater than 50 mm. Rapid cell collapse resulted in significant reductions or oscillations in the measured load. These force transients are noted to be independent of foam core density and occur until displacements approximately equal to 250 mm.

For the high density foam core specimens the force/displacement response was noted to become increasingly nonlinear and obtained a maximum load of approximately 38 kN. The decoupling of foam core pucks was observed to occur early in the deformation process as noted in Figure 12(b). Further decoupling occurs as extension of the braided tube occurs. Decoupling of the foam core pucks results in a force concentration near the vicinity of the necking region. This results in a great degree of localized foam crushing as evident in Figure 12(d). Furthermore, within this region of reduced diameter of the braided tube, tow lockup has occurred and results in significant straining of the tows of the braided tube. Similar behaviour was observed in the findings from Cox and Davis [17] in specimens where massive matrix fracture resulted in dominant chain link interaction and straining thus causing highly localized deformation.

Examination of the high speed photographs showed remains of the foam core that were not fully crushed. As a result of the decoupling between neighbouring pucks, often the free foam core section would re-orientate such that the mid-plane of the puck would no longer be perpendicular to the axial (loading) direction. As a result the energy dissipation potential of the structure is reduced. Furthermore, it is noted that the maximum load supported by the foam filled braided tube is much less than the failure load associated with an empty braided tube under tensile loading. Similar observations were noted by [21] where significant reduction in the failure load is a direct result of the localized necking that occurs within the braided tube. The presence of the neck in the tube results in significant stress concentrations and reduces the load at failure.

For specimens containing low density foam cores, the force/displacement responses are presented in Figure 13. Similar fluctuations in the loading characteristics are observed during foam crush which occurred over displacement ranging from 50 mm to 250 mm. However, the general trend in the force/displacement response, over this range of displacements, is more linear than specimens involving high density foam cores. Braided tubes incorporating low density foam cores typically experience complete foam pulverization and tow lockup through the entire length of the tube. This finding was also noted in other research involving braided tubes with inner cores [23]. Necking in the braided tube is noted to occur, but only to a minor amount, as illustrated in Figure 14 (b)-(d). Without the presence of any significant localized necking occurring within the braided tube, no substantial stress concentrations are imposed on the tows and correspondingly the elongation and maximum load are both increased, compared to specimens incorporating high density foam.

Figures 15 and 16 illustrate the mechanical response of the foam filled braided tubes having high and low density foam cores in the low diameter configuration. A comparison of Figures 11, 13, 15 and 16 illustrate that for a common foam core density, the force/displacement response is consistent with the exception of the significant reduction in maximum displacement at tube failure. For specimens incorporating low diameter foam cores, the elongation to failure is reduced as tow lockup occurs at a lower degree of displacement. As well, it was noted by [17] that by using longer links, the lock up strains can be increased to 0.6 mm/mm, notably higher than the values originally obtained ($\leq$0.5) for the chains used to date.

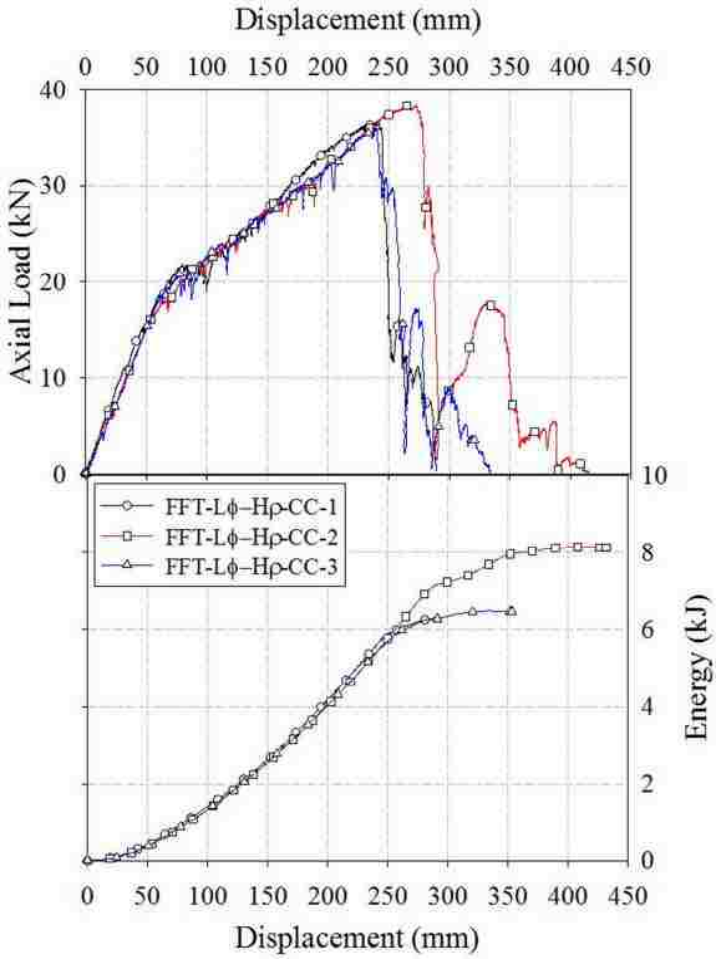

Figure 15: Force/displacement and energy/displacement responses for circular core, low diameter high density filled braided tube.

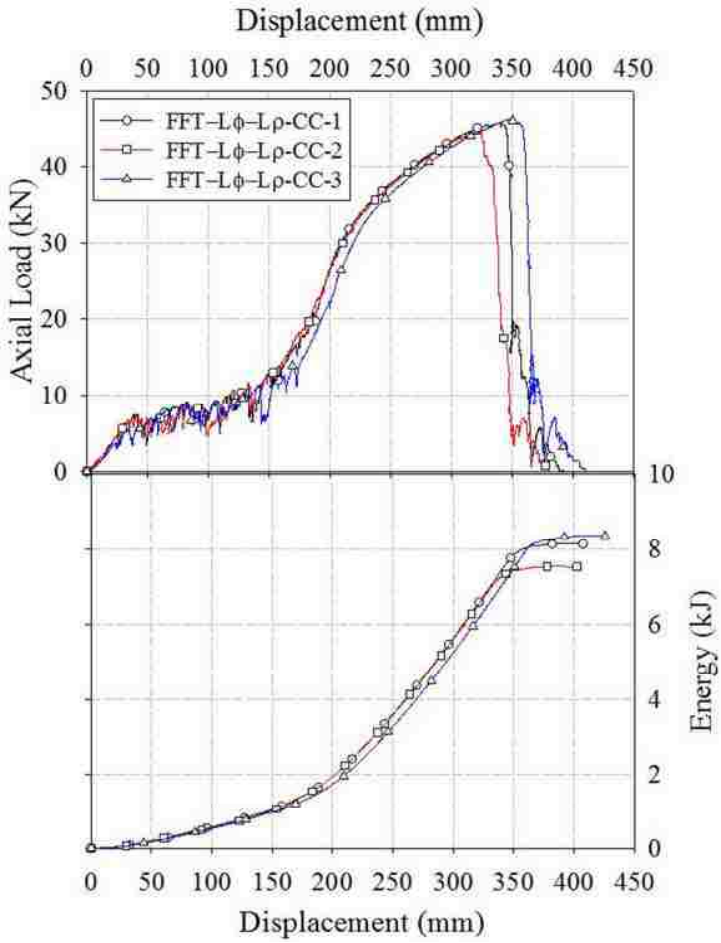

Figure 16: Force/displacement and energy/displacement responses for circular core, low diameter low density filled braided tube.

Independent of the foam core diameter, it is apparent that a strong interaction effect is noted for specimens incorporating high density foam cores. Figures 11 and 15 illustrate that the force/displacement response of these specimens does not exhibit any mechanical characteristics observed for an empty braided tube under tensile loading. If an interaction effect did not exist one would expect that the force/displacement response would illustrate behaviour typical of an empty braided tube after tow lockup, however, this was not the case for the high density foam cores. For specimens incorporating low density cores, independent of the diameter of the core, the force/displacement response after approximately 250 mm was noted to be similar to an empty braided tube. Thus it is

apparent that the interaction effect between the core and braided tube is not as significant in this configuration.

Figures 17 and 18 illustrate the force/displacement responses of representative specimens of high and low diameter cores, respectively. The variable $\delta_{critical}$ is defined in these graphs as the displacement where a transition from foam core crushing to braided tube deformation occurs. The lack of the interaction effect noted to occur in specimens utilizing low density metallic foam results in a significant region in the displacement domain, up to $\delta_{critical}$, where the load bearing capacity of the structure does not vary to a significant extent. Also presented in Figures 17 and 18 are ranges, in the displacement domain, where the average force was computed. Note that the range of displacement used for assessment of the average force (presented in Table 9, for circular cores, and Table 10, for rectangular cores) was from the displacement where foam crushing was noted to commence until no significant further foam compression occurred. This range of displacement was selected since for many of the lower density foam specimens; this region did not exhibit significant increases in the load during deformation. This method of determining average force was used in the computation of the TFE presented in Tables 9 and 10. This mechanical response, where no significant increase in load occurs over an elongation, is favoured in many applications where load limiting devices are needed, for example fall arrest systems. The total energy absorbed, as presented in Tables 9 and 10, is the area bound by the force/displacement curve and the abscissa throughout the entire displacement domain. The SEA, also presented in Tables 9 and 10, is the total energy absorbed by the system divided by the sum of the masses of the braided tube and foam core. An analysis of the variability of the observed values of the TEA, TFE, and SEA was completed and discussions on this analysis are presented in Chapter 7.

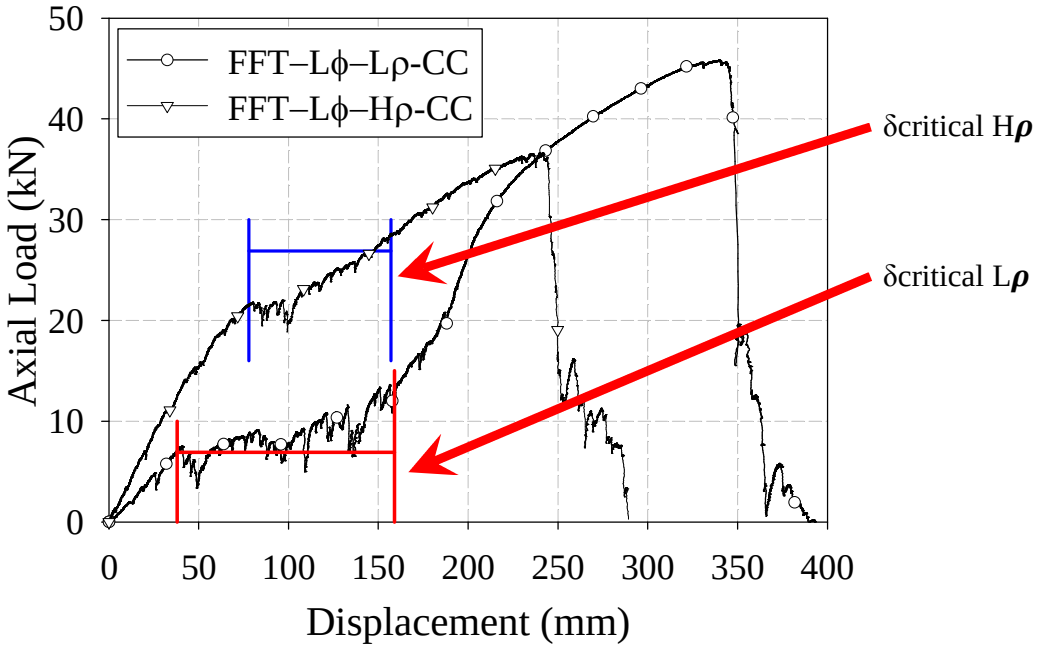

Figure 17: Overlay of low diameter high and low density profiles articulating average force.

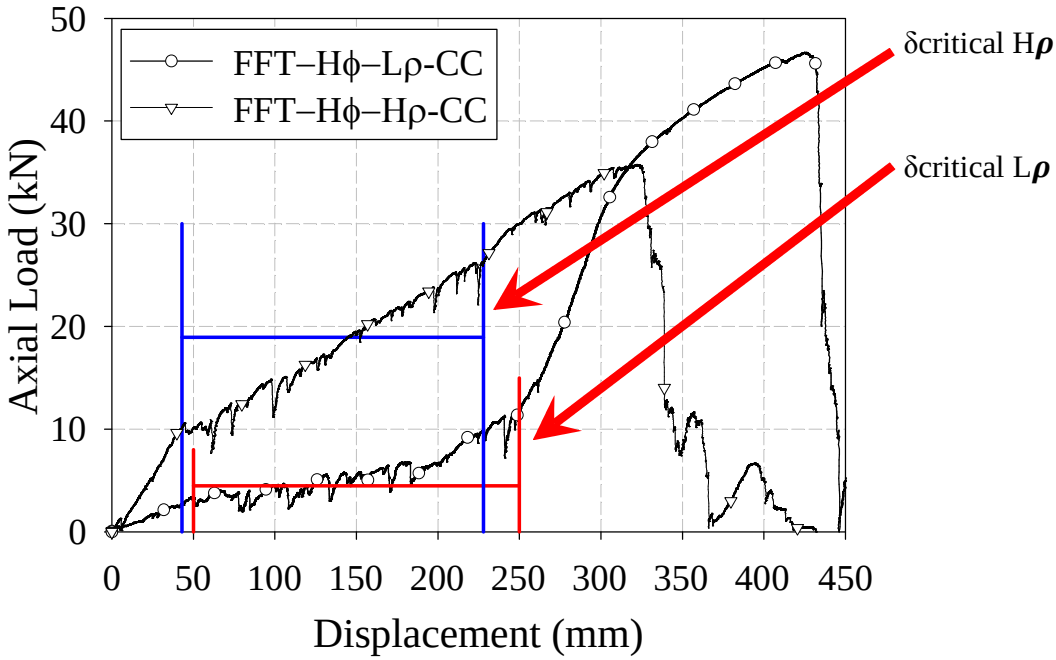

Figure 18: Overlay of high diameter high and low density profiles articulating average force.

From the force/displacement responses in Figure 17, the foam core crushing phase, which was observed to occur over displacements of 40 mm to 155 mm, exhibited a near constant crush force. The average crush force was observed to be approximately 6.9 kN over the foam core crushing phase. The foam core crushing phase for specimens incorporating high density foam was observed to be in the range of 75 mm to 154 mm. In this displacement domain a linear increase in tensile load from 22.8 kN to 28.4 kN was observed and the average crush force was observed to be 26.8 kN.

The load necessary to initiate foam core crushing was observed to be lower for the low density specimens compared to the high density foam cores as evident in Figures 17 and 18. This finding should be expected due to the reduction in mechanical material strength of the lower density foam cores.

Responses of test 3, presented in Figure 11, and test 2 in Figure 15, illustrate a secondary loading regime occurring after the maximum load is obtained and load bearing strength is significantly reduced. This was noted to occur for two out of approximately twenty tests. As a result of the helix configuration of individual wires which form the tows of the braided tube, if failure of tows occurred in a unique fashion, significant degree of tube twisting followed by additional load support occurred. For test 3, which exhibited failure at 334 mm displacement, the braided tube began to twist which provided further support load and correspondingly permitted further energy dissipation. Figure 19 illustrates the twisted region of the braided tube. Prior to this deformation characteristic the braided structure absorbed 7.2 kJ and post twisting, energy absorbed increased to 8.03 kJ. Test 2 exhibited similar characteristics with energy absorption pre- and post-fracture of 7.54 kJ and 8.14 kJ, respectively. This deformation characteristic was noted to occur only for specimens utilizing a high density foam core.

Figure 19: Tapered profile of specimen 2 for low diameter high density circular core tubular assembly prior to failure.

This deformation characteristic was not evident for low density core specimens as the failure mechanism of the braided tubed was a result of complete failure of the wires forming the tows of the tube. The wires failed in entirety through a given section of the braided tube. However, for the specimens incorporating a high density foam core the presence of localized necking within the braided tube resulted in failure of a limited number of wires through a given section; other wires within this section did not fracture. Since the wires of the braided tube form a helix, failure of a limited number of wires will not necessarily result in complete elimination of the load bearing capacity of the structure. Rather, if the location and configuration of neighbouring tows permitted the wires, which did not fail through the section to support further tensile loads, additional elongation would result in further energy dissipation. As a result of the helix configuration the braided tube and failure of a limited number of wires a twisting process to align the load bearing wires to the axial direction occurred. It was observed that this configuration was uncommon and happened only on a limited number of tests specimens.

6.2.3 Tensile response for rectangular foam filled braided tubes

Figures 20 and 22 present the force versus displacement and energy versus displacement responses of the rectangular core aluminum foam filled braided tubes. Photographs depicting the axial deformation process of the high density core for specimen 3 are illustrated in Figure 21 and photographs for low density core for specimen 2 are illustrated in Figure 23. Annotations in Figures 20 and 22 correspond to the images in Figure 21 and 23, respectively. Table 10 presents the average force, TFE, TEA, and SEA of the foam filled braided tube for a given test. Note that the average force, TFE, and SEA are computed as discussed in Section 6.2.2.

The force/displacement responses, as depicted in Figure 20, illustrate a strong interaction effect, between the foam core and the braided tube, occurring for specimens containing high density foam cores. The specimens in Figure 20, after approximately 300 mm displacement, do not exhibit mechanical characteristics similar to an empty braided tube under tensile loading. Photographs of the axial deformation process for specimens containing high density rectangular cores illustrate that necking in the braided tube occurred as illustrated in Figure 21 (d)-(g). However, the degree of necking within the specimens was noted to be lower than observed for specimens containing cylindrical cores. This difference is associated with the lack of adhesive bonding between the individual foam panel sections, which make up the interior rectangular core, perpendicular to the axial/loading direction. The localized collapse of cells and fracture of the rectangular foam core results in this minor degree of necking. No consistency in the location of the fracture/collapse of the foam core was observed, however, it is hypothesized that inconsistent foam cell geometry and distribution in the manufacturing of the foam may be the rationale for this finding. No testing was completed to investigate this hypothesis. Additionally, the response of test 1 was observed to occur over a longer displacement. This is expected as the original length of the braided tube for test 1 was longer than those utilized in tests 2 and 3. However, peak loads and general deformation characteristics are consistent amongst all three tests.

For specimens incorporating low density cores, foam crushing ensues immediately following the application of tensile load. Significant crushing of the foam core was noted to occur at displacements greater than 50 mm. Photographs depicting the axial deformation of the low density rectangular cores, as presented in Figure 23, illustrate complete foam pulverization without the presence of any significant localized necking occurring within the braided tube. Correspondingly, the elongation and maximum load are both increased, compared to specimens incorporating high density foam. The force/displacement response after approximately 250 mm, as illustrated in Figure 22, was noted to be very similar to an empty braided tube. Photographic evidence of the deformation characteristics presented in Figure 23 (e) and (f), illustrate that the foam core was completely crushed to the extent that the braided tube experienced tow lockup (just following deformation after Figure 23 (d)) throughout its entire length. Clearly, the interaction effect between the foam and the braided tube is negligible as load to failure of the foam filled specimen was rather consistent to an empty braided tube, with a value approximately equal to 50 kN.

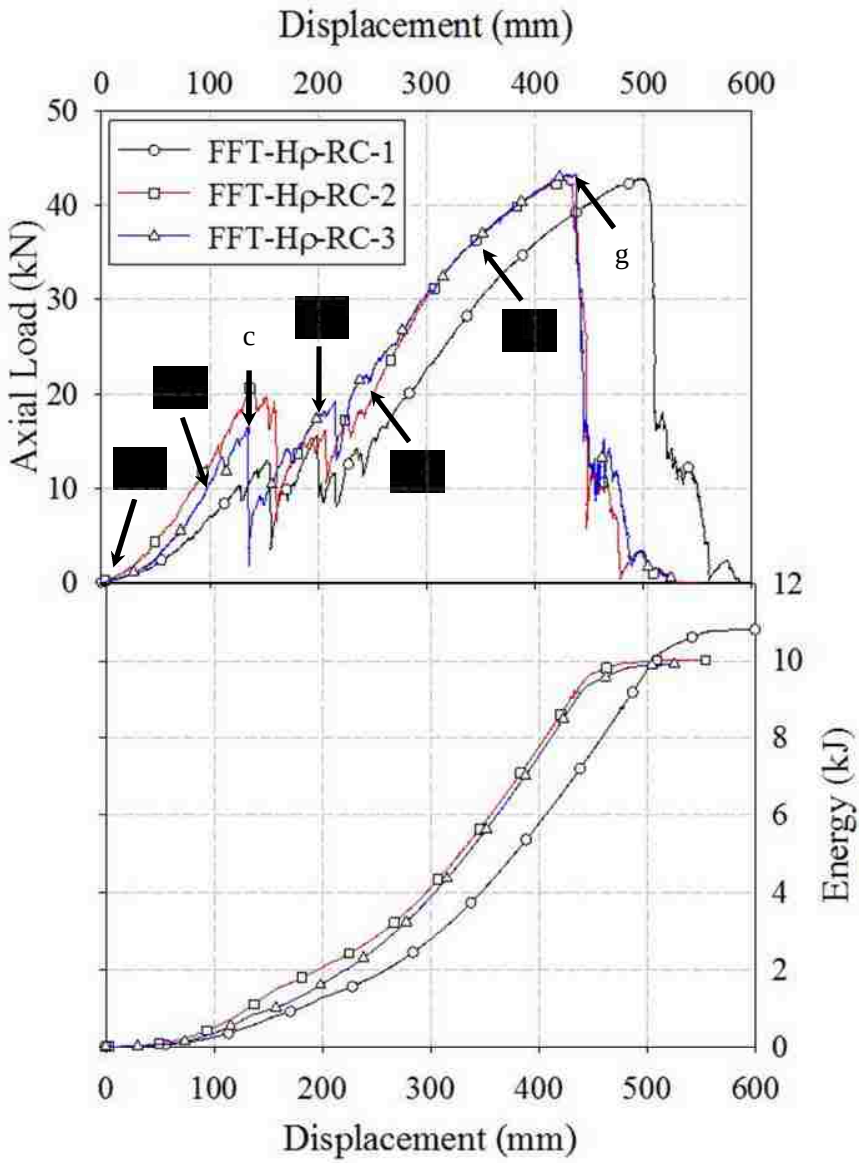

Figure 20: Force/displacement and energy/displacement responses of rectangular cores high density.

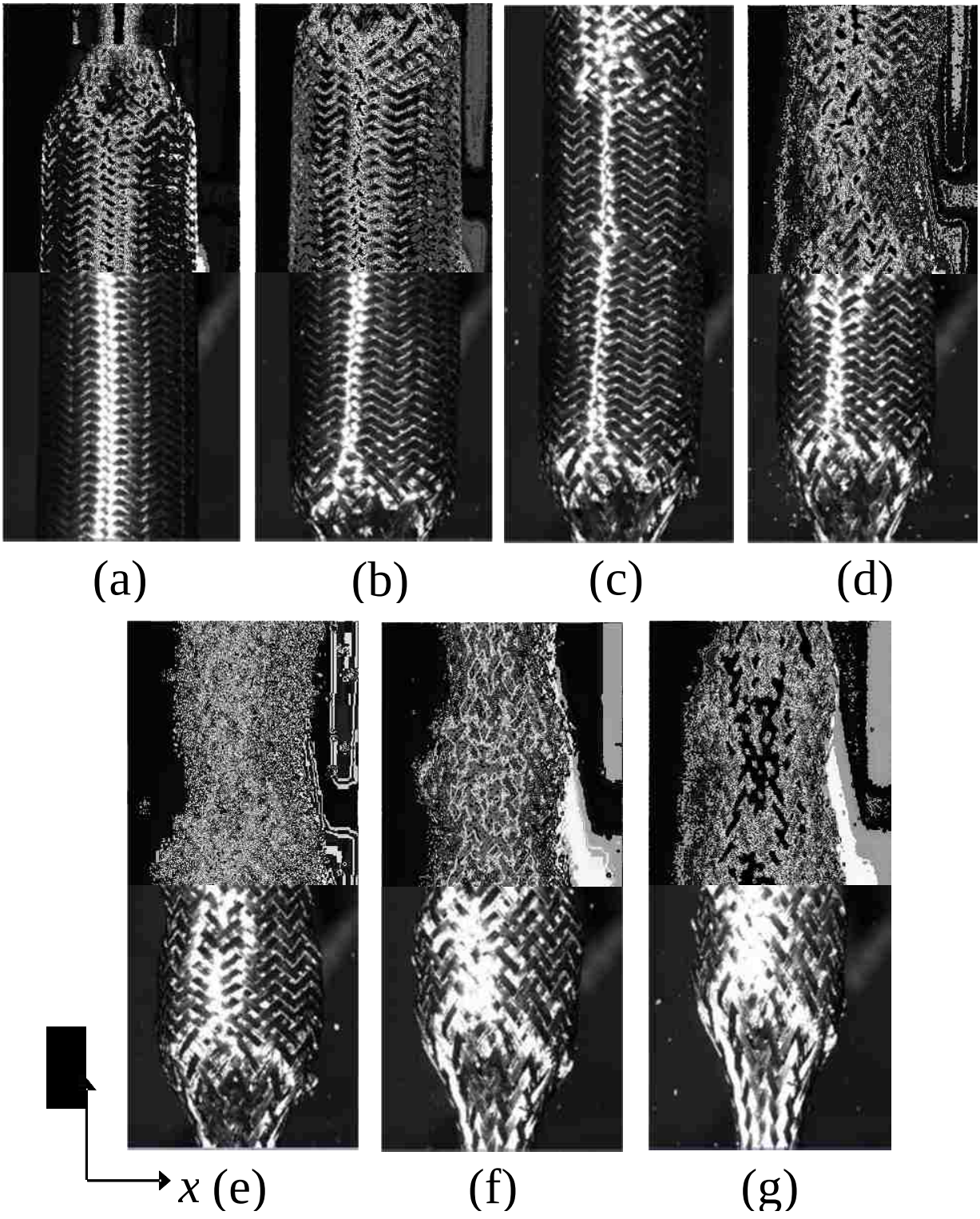

Figure 21: Photographs illustrating the axial tensile deformation process of the high density rectangular core braided tube for specimen 3.

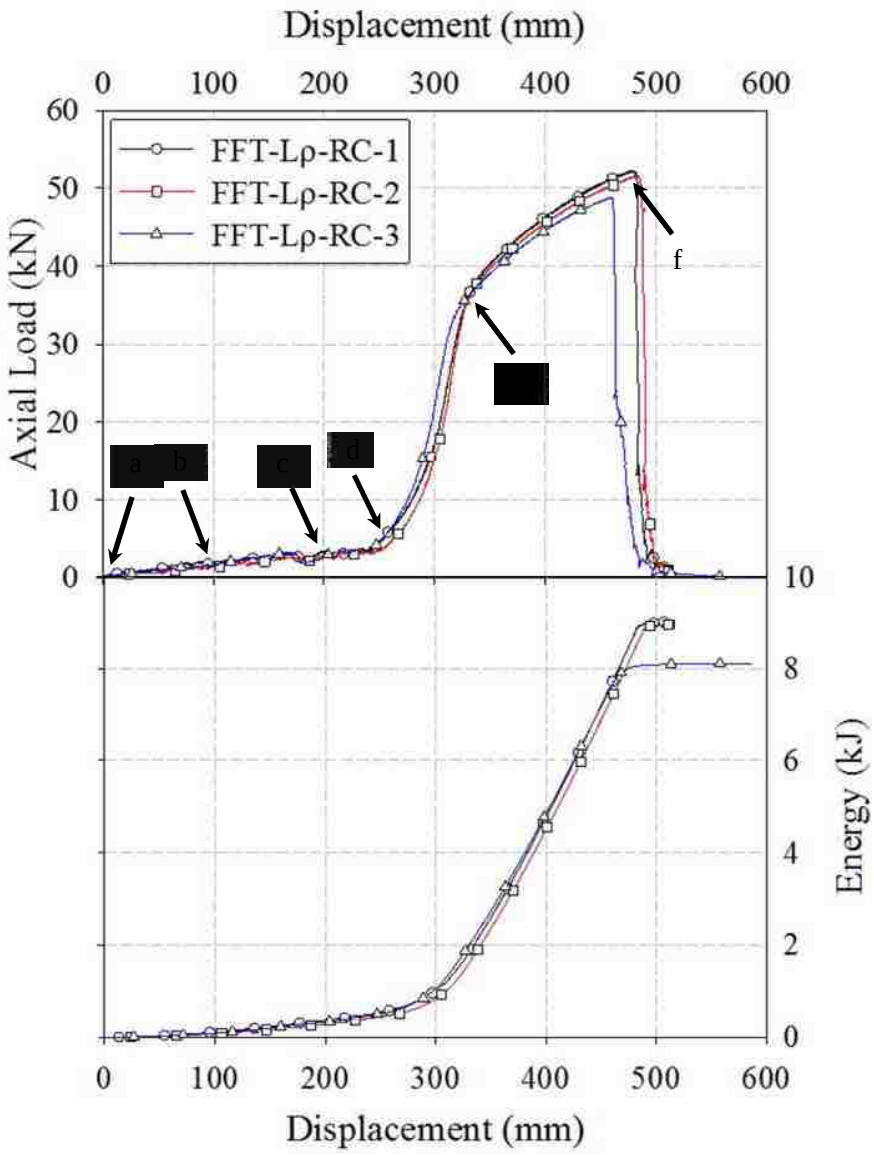

Figure 22: Force/displacement and energy/displacement responses of rectangular cores low density.

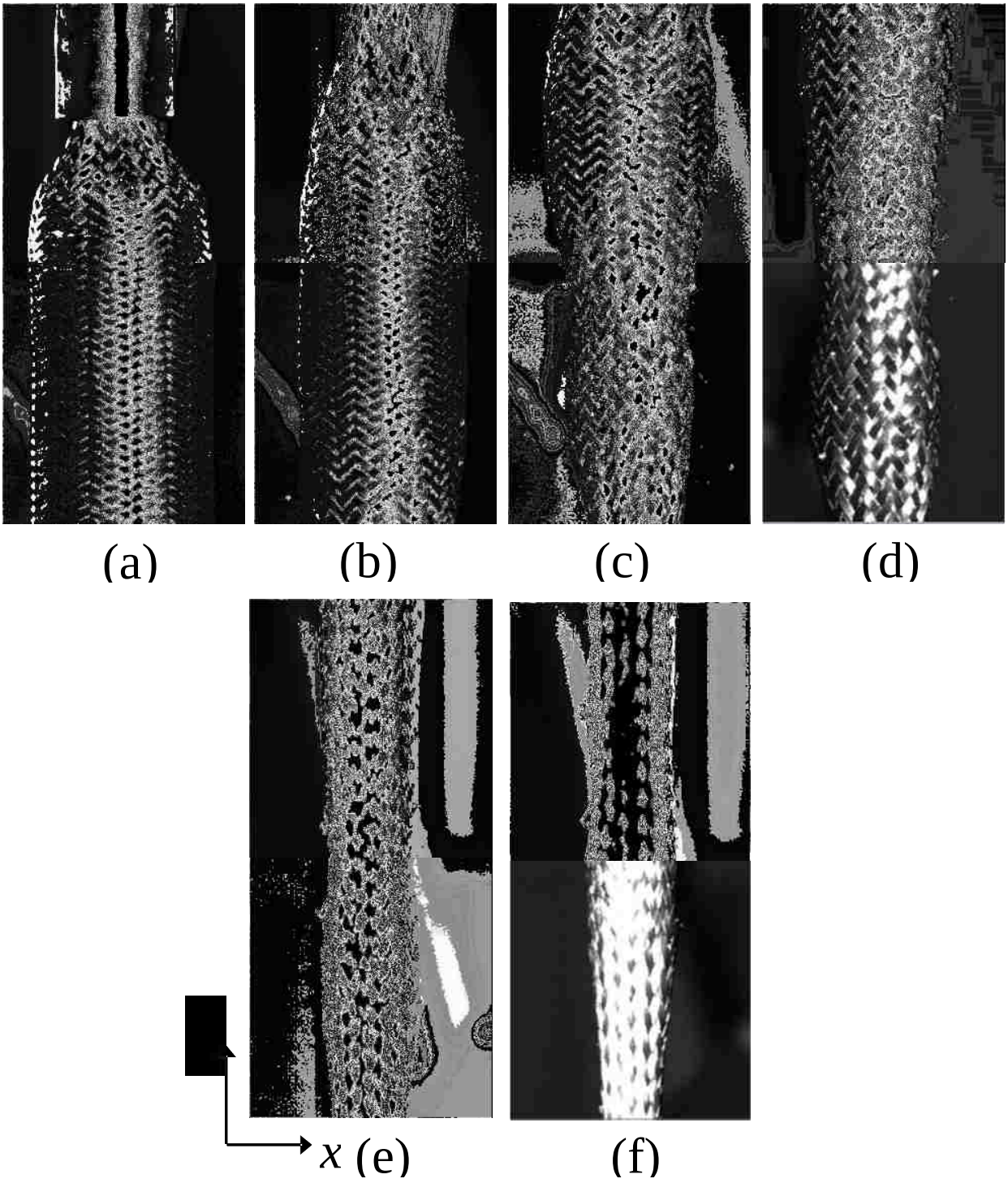

Figure 23: Photographs illustrating the axial tensile deformation process of low density rectangular core braided tube for specimen 2.

Figure 24 presents the force/displacement responses of low and high density aluminum foam rectangular core filled braided tubes. Similar to Figures 17 and 18, the value of $\delta_{critical}$ is illustrated in Figure 24 as well as the range of displacement where the evaluation of the average tensile force was computed for each specimen. Comparison of the two results presented in Figure 24 further articulates the lack of any core/braided tube interaction effect for the specimen utilizing a low density aluminum foam core, while an interaction between the two components is evident in the case of the specimen incorporating a high density aluminum foam core. Although the displacements at $\delta_{critical}$ are approximately equal for both specimens, significantly reduced loads after displacements greater than approximately 275 mm are evident for the specimen utilizing a high density core. Clearly the force/displacement behaviour is not a linear combination of foam crushing followed by braided tube deformation as assumed in the analytical model of Cheng et al. [16]. However, such a statement is not correct for the specimen incorporating the low density aluminum foam core, which appears to exhibit a response where little or no interaction effect is found. Based upon the photographs presented in Figures 21(b) and 23(b), as well as Figures 12(b) and 14(b), it is evident that for specimens incorporating a high density foam core, the elevated mechanical strength of the core does not allow for a uniform foam crushing process to occur and thus a less favourable interaction between the stainless steel braided tube and high density foam core results. Correspondingly, localized necking of the composite structure during elongation reduces the load bearing capacity after the core is crushed as much as it can be [21].

It is evident that the observed interaction effect between the foam core and braided tube is dependent upon the density of the foam core and, to a lesser extent, the assembly process of the high density foam core. For example, specimens who utilized a circular core typically failed at lower elongations compared to specimens which incorporated a rectangular core. The puck separation, in the circular core specimens, resulted in localized necking within the braided tube and reduced the total elongation to failure as a result of the localized deformation. Such an interaction effect was not noted by Cheng et al. [16] which may be attributed to the foam core densities which were utilized in their studies but also, and importantly, the multiple loading/resetting cycles of the specimens

completed by Cheng et al. [16]. When resetting the specimen for a subsequent loading cycle, the crushed interior foam core would have orientated itself potentially more uniformly within the braided tube. Correspondingly, the observations noted in the research in [16] deviate from the present study.

Examination of the SEA values presented in Tables 9 and 10 indicate that specimens containing the low density aluminum foam core illustrated notably higher SEA when compared to specimens having a high density core. This can be attributed to the lack of localized deformation for specimens containing low density aluminum foam cores. Localized deformation, as was found for specimens with high density foam cores, resulted in failure of the braided structure before complete core crush could be obtained; thus resulting in reduced energy dissipation capacity. A minor increase in the SEA is noted for low density aluminum foam filled braided tubes compared to empty braided tubes of similar length. A lower SEA exists for high density foam filled braided tubes compared to an empty braided tube.

Additionally, experimental observations (in Table 9) indicate that there is no significant influence of the diameter of the foam core on the SEA. As well, there appeared to be no significant variation of the SEA for either the circular or rectangular core low density specimens, however, an approximate 20% reduction was noted for the SEA for specimens containing a rectangular core compared to circular cores. This is most likely a result of the slightly higher density of the high density rectangular foam cores, which result in mechanical strength incompatibilities between the core and the braided tube causing braid tube failure at lower levels of deformation.

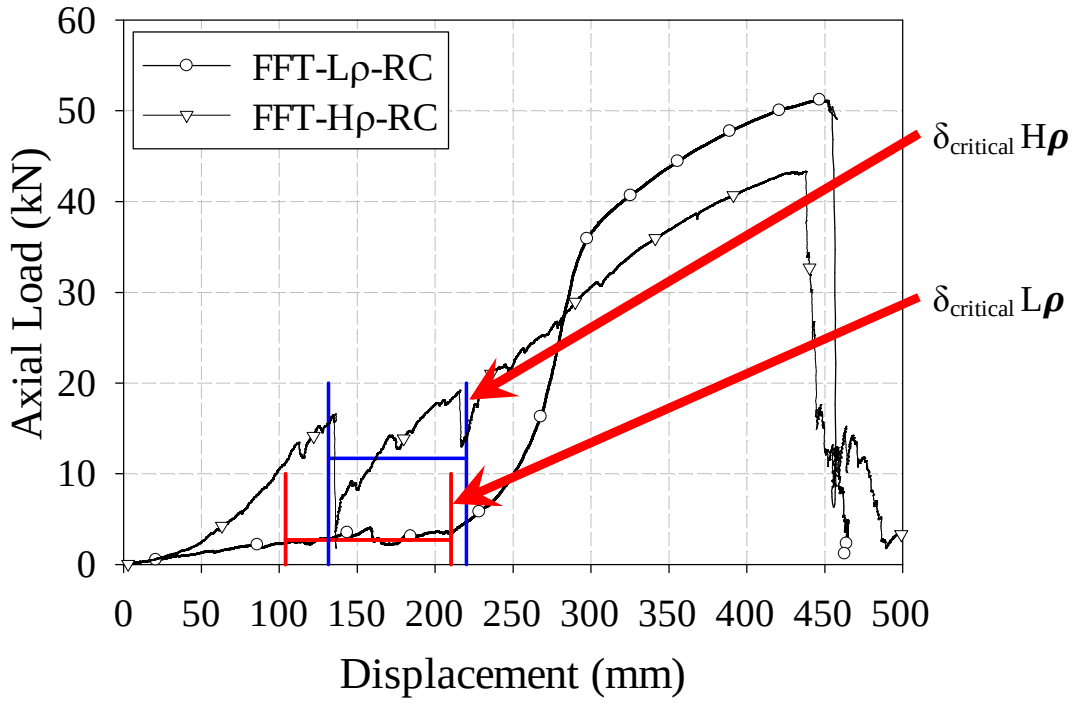

Figure 24: Overlay of rectangular core high (test 3) and low density (test 1) profiles articulating average force.

6.3 Braid motion analysis and discussion for theoretical model validation

6.3.1 Tow motion analysis – validation of the unit cell equations

An examination of the results of the radius versus length behaviour from image analysis, presented in Figure 7, indicated that both lines 1 and 2 of the tracked regions were very similar. This behaviour was expected since careful selection of the location of the tracking lines was completed. For clarity and brevity, results are presented for only line 1 tracked region.

The theoretical model developed by [16] ultimately predicts energy absorption as a function of displacement. The theoretical model is based on the unit cell concept where the braided tube diameter and length are related to the angle between the crossing tows and is described in detail in reference [16]. Similar kinematic relationships are noted in [20] and [21] that are applied to various braid tow angles. In addition, [19] and [23-25]

provide detailed analytical models to describe the cross sectional shape of the foam core and braided tube upon tensile load application. Relevant equations to illustrate the validation process are presented below. Figure 25 illustrates the unit cell used in the derivation of these equations. The distance between two nodes, along a tow, within the unit cell is defined by the symbol '*l*'. Correspondingly, the distances in the axial and radial directions are related to '*l*' and '*θ*', the current angle between the tows through equations (4) and (5), respectively.

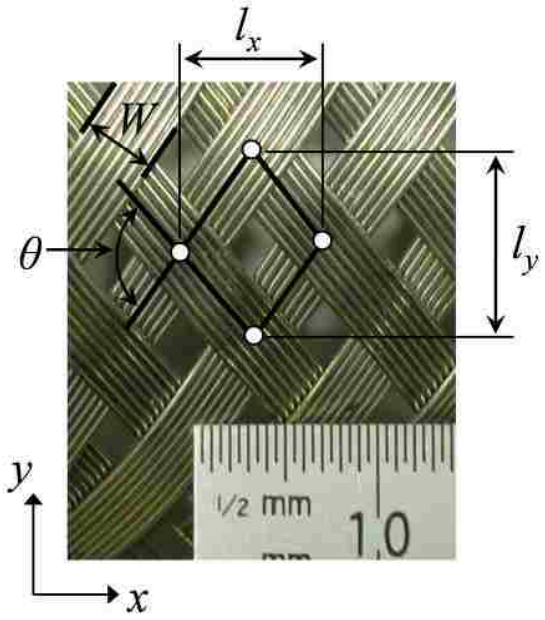

Figure 25: Unit cell of the braided tube and the associated geometric parameters.

$$l_y = 2 \cdot l \cdot \sin\left(\theta/2\right) \tag{4}$$

$$l_x = 2 \cdot l \cdot \cos\left(\theta/2\right) \tag{5}$$

Using these parameters, an expression for the initial tube radius 'R_o' and the current radius 'R' is related to the initial ('θ_o') and current ('θ') braid angles through equation (6).

$$\frac{R}{R_o} = \frac{\sin\left(\theta/2\right)}{\sin\left(\theta_o/2\right)} \tag{6}$$

The initial ('L_o') and current ('L') lengths of the braided tube are related to the initial and current braid angles through equation (7).

$$\frac{L}{L_o} = \frac{\cos\left(\theta/2\right)}{\cos\left(\theta_o/2\right)} \tag{7}$$

Validation of the theoretical model was completed through comparison of the radius as a function of instantaneous length of the braided tube. This was completed by solving equations (6) and (7) for the current braid angle then equating both of these equations and solving for the instantaneous radius as a function of instantaneous length. In this analysis, values for the initial radius, initial length, and initial braid angle were experimentally measured to be 49.98 mm, 336 mm, and 55.3 degrees, respectively. These values were obtained from images obtained from experimental elongation of an empty braided tube prior to tow lockup.

Figure 26 illustrates the instantaneous radius of the braided tube as a function of instantaneous length of the braided tube for both the analytical model and experimental findings. A strong agreement between both findings is evident with a nonlinear response observed. Theoretical findings from the analysis typically under-predict experimental values of the radius for length increases of the braided tube.

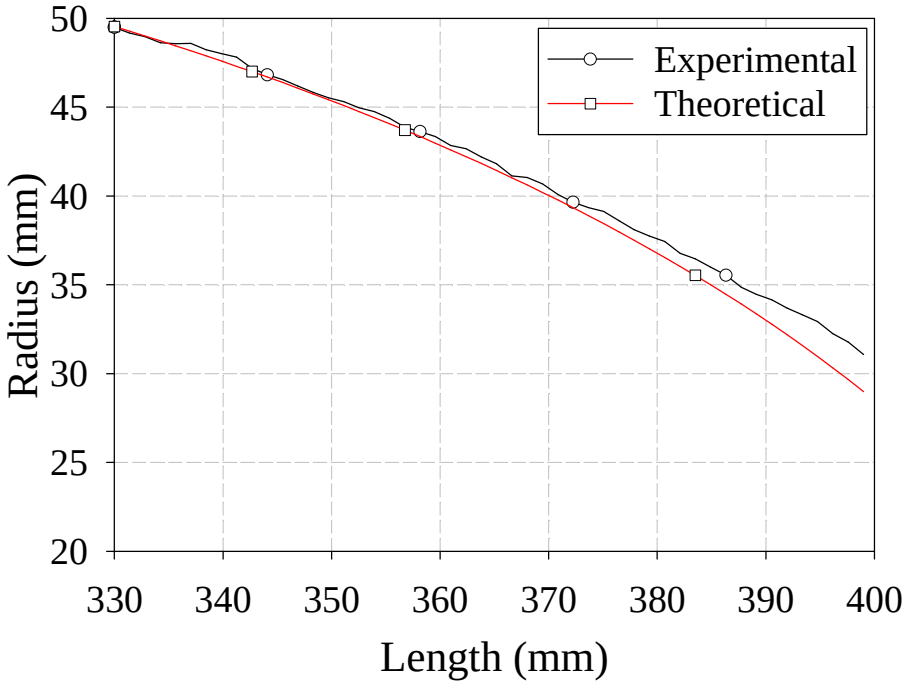

Figure 26: Experimental and theoretical radius versus instantaneous length findings.

To investigate the difference between theoretical predictions and experimental measurements evaluation of the error between both methods was completed. The error, computed from equation (8), represents the average error determined over the entire length consideration of the braided tube. Additionally, a validation metric '*V*', as proposed by Oberkampf and Trucano [42] was computed using equation (9). The validation metric has the following four advantages. First, it normalizes the difference between the theoretical results and the experimental data by computing a relative error norm. Second, the absolute value of the relative error only permits the difference between the theoretical results and the experimental data to accumulate. Third, when the difference between the theoretical results and the experimental data is zero at all measurement locations, then the validation metric is unity. And fourth, when the summation of the relative error becomes large, the validation metric approaches zero. The last two aspects exist due to the implementation of the hyperbolic tangent function.

$$Error = \frac{1}{L_2 - L_1} \cdot \int_{L_1}^{L_2} \left| \frac{R_{Exp}(L) - R_{Theory}(L)}{R_{Theory}(L)} \right| dL \tag{8}$$

$$V = 1 - \frac{1}{L_2 - L_1} \cdot \int_{L_1}^{L_2} \tanh\left(\left| \frac{R_{Exp}(L) - R_{Theory}(L)}{R_{Theory}(L)} \right| \right) dL \tag{9}$$

In order to compute the error and validation metric a cubic spline representing the experimental radius as a function of length was determined to numerically compute the integrals within equations (8) and (9). Following this regression, which resulted in a correlation coefficient equal to unity, the error and validation metric were found to be 0.98 and 1.69%, respectively. As a result, the unit cell model developed by the researchers from reference [16] generates accurate predictions for radius/length behaviour of the braided tubes prior to tow lockup.

6.3.2 Analytical model predictions compared to experimental findings

The analytical model developed by Cheng et al. [16] was based upon the assumption for uniform tube deformation over the entire length of the tube. The model does not account for tow sliding/contact and the frictional effects associated with such motion, fracture of the foam core, or any nonhomogeneous aspects of the foam core. A brief overview of the model is presented and the reader is encouraged to review [16] for a complete derivation of the model. Also, similar micromechanical models are presented in [20] and [21]. As previously indicated the semi-empirical model assumes uniform foam crushing and braided tube elongation after tow lockup. The assumption of a uniform foam core subjected to radial compression was also applied by the researchers in [10]. Correspondingly, the energy dissipated is the sum of the energies associated with foam crushing and tube elongation, as expressed in equation (10).

$$E_{total} = E_{foam} + E_{tube} \tag{10}$$

The energy absorbed by the aluminum foam core is a result of radial compression by the braided tube during elongation prior to tow lockup. The contact area between the tube

and the foam was assumed to be equal to the area of the lateral faces of the foam core. The total work to crush the inner foam core is equal to the energy dissipated by the foam and is presented in equation (11) as a function of the instantaneous width of the foam core.

$$E_{foam}(w) = U_{foam}(w) = \sigma_{pl} \cdot L_{foam} \cdot \left(w_o{}^2 - w^2\right) \tag{11}$$

It is important to note that the value of the core width, w, will only vary between the initial width, w_o, and the width at tow lockup. The instantaneous width of the foam core can be found from the length/radius relationship of the braided tube (equations (6) and (7)).

The braided tube will not contribute to energy absorption until tow lockup. After lockup occurs, the foam core no longer contributes towards energy dissipation and tows of braided tube will undergo plastic deformation due to extension. A bilinear force/displacement behaviour of the braided tube is assumed in the model (consistent with experimental findings, as evident in Figures 8 and 9) with the stiffness of the tube in both regions determined from experimental findings. This portion of the model requires experimental observations to determine the stiffness in each region of the force/displacement response, which follows a standard methodology as presented in [16]. In the case of the second assumed linear region of the force/displacement response the ordinate intercept is also required to be found (f_2). With this empirical information the energy dissipated by the tube during elongation is presented in equation (12).

$$E_{tube}(y) = \begin{cases} \dfrac{k_1 \cdot \left(y - L_{lockup}\right)^2}{2} & \text{if } L_{lockup} \le y \le L_{crit} \\ \dfrac{k_1 \cdot \left(L_{crit} - L_{lockup}\right)^2}{2} + \dfrac{\left(\left(k_2 \cdot \left(L_{crit} - L_{lockup}\right) + f_2\right) + \left(k_2 \cdot \left(y - L_{lockup}\right) + f_2\right)\right) \cdot \left(y - L_{crit}\right)}{2} & \text{when } y > L_{crit} \end{cases} \tag{12}$$

With the critical length, L_{crit}, being the abscissa value of the intersection point for the two linear force/displacement regions, computed using equation (13).

$$L_{crit} = \frac{f_2}{k_1 - k_2} + L_{lockup} \tag{13}$$

The sum of equations (11) and (12) during extension will provide an analytical estimate to the total energy dissipated by the aluminum foam filled braided tube.

Comparison of the analytical model predictions with the experimental findings was completed for both low density and high density rectangular foam cores contained within braided tubes. No comparison between the model predictions and the response of specimens containing a circular foam core were completed as the deformation behaviour of the circular cores was strongly dependent upon the failure of the adhesive between interior foam pucks. It was recognized that this difference in deformation would not permit a suitable comparison.

In the following analyses a comparison of the energy/displacement responses are completed. It should be noted that the analytical model predictions are offset in the displacement domain by 30 mm and 70 mm for the specimens containing low density and high density foam cores, respectively, to account for any slack, gap, or excess length of braided tube to ensure direct contact of the tube to the foam core. These displacement values were selected based upon the observed increase in energy between experimental findings and model predictions.

Figure 27 illustrates the energy versus displacement responses from experimental findings (test 1) and model predictions. Good agreement is observed with an error of 3.03% between the two measurements (over the entire displacement domain) and a validation metric of 0.97. It should be noted that this low degree of error is only achieved once an offset was applied within the displacement domain to accommodate for the initial slack of the specimen, gap, or excess length of braided tube. The author is of the opinion

that the values of the offsets used were very appropriate given the challenges associated with the assembly and loading of the specimens. Attempts to load/unload/reload were not considered as in previous research [15] such approaches resulted in observations which were not consistent to the findings from this investigation. Slight over prediction of the experimental findings was noted to occur for the model, over the majority of the displacement domain. The model indicates that tow lockup occurs at approximately 280 mm displacement as is evident with a sharp transition in the energy absorbed at this displacement. Experimental results indicate a smoother transition between foam crushing and braid plastic deformation at approximately 300 mm. Figure 23b illustrates the uniform deformation of the braided tube over the majority of its length. It is believed that as a result of the consistent deformation along the length of the tube that good correlation between experimental findings and analytical model predictions exist.

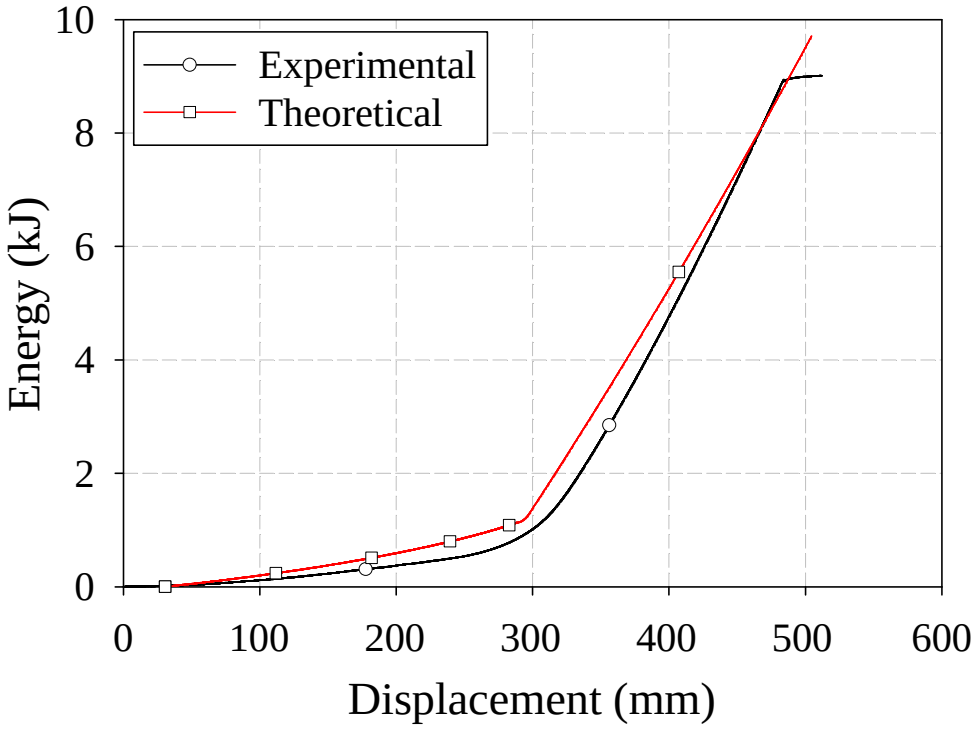

Figure 27: Comparison between theoretical model developed by Cheng [16] to experimental results for low density rectangular foam filled braided tubes.

Similar comparison was completed for high density rectangular foam filled braided tubes. Figure 28 illustrates the theoretical and experimental (test 2) response. The energy/displacement responses deviate significantly from each other throughout the entire displacement domain. The error and validation metric were found to be 16.45% and 0.85, respectively, indicating significant differences in the responses. The variation in the assumed uniform deformation behaviour of the analytical model to the non-uniform, localized deformation observed to occur in the experimental specimen is believed to be the rationale for the significant deviation. Necking of the braided tube near the vicinity of the foam core fracture locations are deformation characteristics which are not considered in the analytical model. Importantly, the higher density foam core results in an incompatibility between the core and the braided tube so that the structure no longer behaves as an energy absorption device where dissipation is based upon foam core crushing and braided tube extension alone.

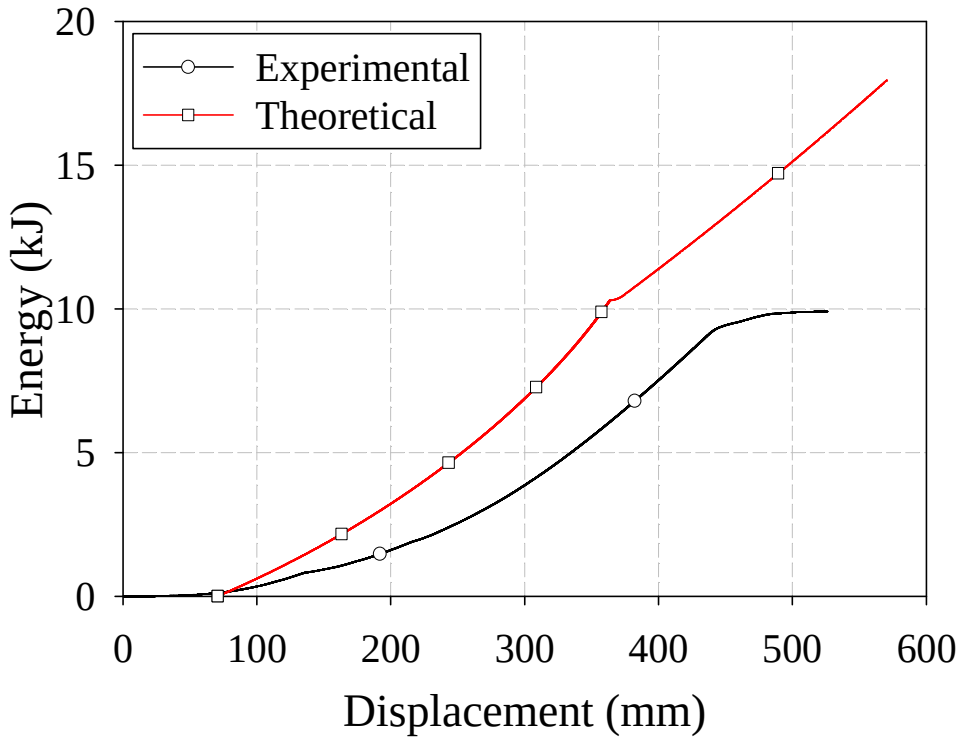

Figure 28: Comparison between theoretical model developed by Cheng [16] to experimental results for high density rectangular foam filled braided tubes.

6.4 Experimental observations and discussion for transverse tests

6.4.1 Transverse response of empty braided tubes

Quasi-static transverse tests were performed on empty braided tube specimens of approximately 330 mm in length. Figure 29 illustrates the force versus displacement and energy versus displacement response of empty tube specimens. Photographs depicting the transverse deformation process of specimen 3 are illustrated in Figure 30. Table 11 presents the average force recorded, force efficiency (FE), total energy absorption (TEA), and the specific energy absorption (SEA). The average force is computed as the area bound by the force/displacement response and the abscissa, normalized with respect to the total displacement observed within each test. The FE is computed as the average force normalized with respect to the maximum force observed in a given test. The total energy absorbed is the integral of the area bound by the force/displacement response. The SEA is the energy absorbed by the energy dissipation device divided by its mass. Five tests were completed for the empty tube configuration, with a new specimen incorporated in each test. Consistent force/displacement observations were determined for the transverse testing on the empty braided tubes, thus, for clarity and brevity, the responses of the first three tests are presented in Figure 29 below.

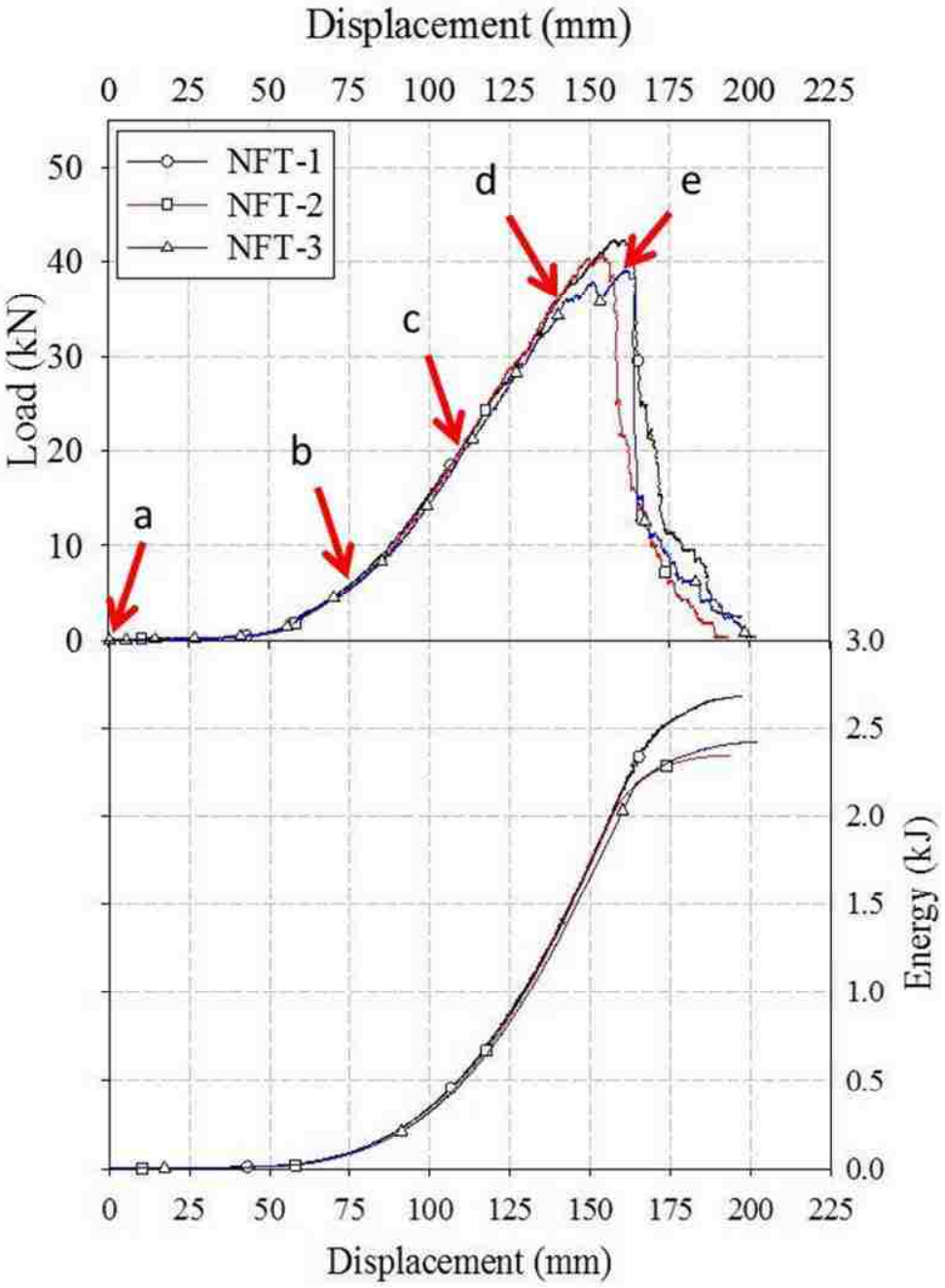

Figure 29: Force/displacement and energy/displacement responses for empty braided tube of length 330 mm.

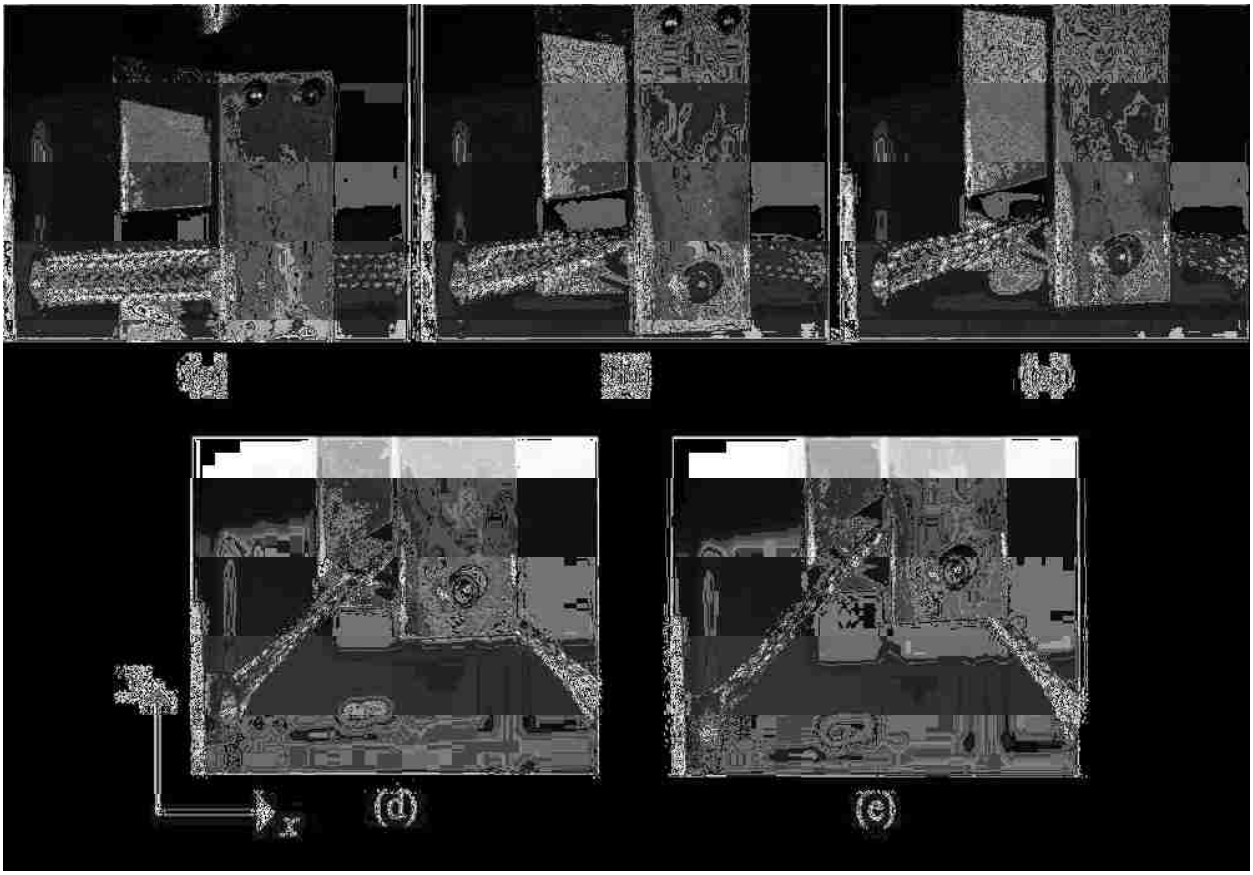

Figure 30: Photographs illustrating the transverse deformation process of empty braided tube for specimen 3.

Results illustrate that empty tubes exhibit slow load increase up to approximately 1.5 kN corresponding to displacement from 0 mm to 60 mm. This response was due to the initial and developing contact between the centre loading bar and the tow wires at the lower fibers of the braided tube. Following this condition, further contact between the tube and loading bar was observed. The angle between tows of the tube in direct contact with the loading bar decreased rapidly and underwent lockup resulting in elastic and plastic deformation of the wire strands; Figure 30(c) depicts this behaviour. Further loading induces a steep linear increase in the force/displacement response as a result of the deformation occurring within the wires forming the tows of the braided tube. At approximately 125 mm displacement a slight deviation in the linear response is noted which is most likely associated with the combined elastic/plastic deformation of the wires

forming the tows of the braided tube and highly localized wire bending at the tow contact locations. Further loading resulted in progressive failure (occurring near the annular clamps) which was observed once a peak load of approximately 40 kN was achieved at roughly 150 mm of crosshead displacement. The peak load was noted to be the ultimate failure load of the empty braided tubes.

It was discovered that when empty braided specimens were loaded in the transverse direction, a significant reduction in stiffness, compared to findings under an axial tensile loading condition, was noted. When comparing the average stiffness of empty braided tubes from [43] to the results obtained within this study, the stiffness was approximately 711.98 kN/m, for loading in the axial direction, compared to 490.69 kN/m, for loading in the transverse direction. Specific to the transverse loading condition within this investigation, the stiffness was measured in the displacement domain between the range of 75 mm to 125 mm, respectively. Additionally, the stiffness was computed through the force (obtained from the load cell) and the vertical displacement of the centre loading bar (obtained from the LVDT). The significant reduction in stiffness is a result of a combination of factors which includes (1) flattening of the braided tube at the mid-span, (2) inhomogeneity of tow scissoring, (3) and tow stack up in the vicinity of the applied load.

The nature of the transverse loading results in the development of tensile forces within the braided tube. Following the application of transverse load, two distinct regions develop along the length of the tube on either side of the centre loading bar. Tows do not demonstrate uniform lockup behaviour throughout the length of the tube. As the mid-span of the tube is displaced vertically by the centre loading bar, tows located near the lower portion of the annular clamps undergo immediate tow lockup while tows on the upper portion of the annular clamps have not yet locked. This is due to the fact that the lower fibers are undergoing a greater degree of tensile elongation due to the nature of the loading and the prescribed boundary conditions. Figure 30(a) - (e) illustrates that at the mid-span of the braided tube, the lower fibers contact the upper fibers as a result of the conformation to the circumference of the loading bar. This creates tow stack up at the

vicinity of the loading bar such that the braided tube tows do not achieve the desired scissoring effect, rather, tow bending occurs. Thus, in the transverse loading condition, uniform tow lockup throughout the entire tube is not achieved.

The energy absorption of empty braided tubes, illustrated in Figure 29, was noted to increase in a quadratic fashion as crosshead displacement increased. At approximately 50 mm of displacement, the energy absorbed began to increase as a result of tow lockup. Further transverse load application induces plastic deformation of the tows which reflects the rapid increase in energy absorption that ultimately reached approximately 2.7 kJ. The main energy absorption mechanism is plastic deformation of tows throughout the braided tube, however, a higher degree of deformation, noted to occur in the vicinity of the clamps and center loading bar, most likely results in a greater degree of localized energy dissipation at these regions.

Failure resulting from tow lockup was noted to occur at the lower portion of the annular clamps, as presented in Figure 30(d) - (e), at approximately 40 kN corresponding to displacement slightly larger than 150 mm. Referring to Figure 29, just prior to 150 mm displacement, a load softening effect is noted to occur, which was the result of the failure of individual wires within the braided tube near the vicinity of the clamp on the side of the tube where the loading bar contacted. Failure of the wires mitigated any kinematic constraints on the tows at these regions of the braided tube, and thus large gaps within the tows of the braided tube were evident in these regions. Such deformation behaviour resulted in a progressive failure where a more significant load softening effect was noted to occur.

The SEA for tests 1-3 found in Table 11 was consistent. The average SEA was computed to be 5.49 kJ/kg. When the average SEA was normalized with respect to the initial length of the specimen (330 mm); the SEA was calculated to be approximately 16.64 kJ/(kg·m).

6.4.1.1 Force analysis of empty braided tubes

Figure 31 illustrates a free body diagram of the forces acting on the empty braided tube during the deformation process. The vertical force, identified as F_v, is measured by the load cell as the centre loading bar progresses in the positive *y* direction. Symmetry about the *y* axis was applied to simplify the force analysis. The nature of the transverse loading results in a resultant tensile force through the specimen with negligible bending strength assumed. The components of the tensile force include the vertical force acting opposite (negative *y* direction) of F_v, which is identified as F_{v_Tube}, and a horizontal force identified as F_{h_Tube}. The resultant of the vertical and horizontal tube forces is identified as F_{R_Tube}, which is assumed to act along the axial direction of the straight section of the braided tube. The measure of F_v allows for determination of F_{v_Tube}. The angle θ represents the angle between the *x*-axis (horizontal) direction and the assumed line of action of F_{R_Tube}, as illustrated in Figure 5. The angle θ is computed from the initial length of the specimen in the *x*-axis direction and the displacement of centre loading bar, Δy, as presented in equation (14).

$$\theta = \tan^{-1}\left(\frac{\Delta y}{L_o/2}\right) \tag{14}$$

This angle increases from the initial undeformed tube state (where θ is 0 degrees) up to the ultimate tube deformation state (just prior to tube failure) which was generally found to be approximately 46 degrees for an empty braided tube.

The forces depicted in Figure 31 are used in the derivation of the resolved horizontal and vertical forces within the braided tube. The horizontal component of the tube tensile force is given by the relation of the initial (L_o) length of the braided tube, F_v (measured from the load cell), and Δy (the vertical displacement of the centre loading bar measured by the LVDT) through equation (15). The tube vertical component force is equal to one half of the vertical load F_v as presented by equation (16).

$$F_{h\_Tube} = \left(\frac{L_o \cdot F_v}{2 \cdot \Delta y}\right) \tag{15}$$

$$F_{v\_Tube} = \frac{F_v}{2} \tag{16}$$

Using equations (15) and (16), F_{R_Tube}, representing the magnitude of the tensile load acting through the braided tube during the transverse test, can be computed using equation (17).

$$F_{R\_Tube} = \sqrt{(F_{h\_Tube})^2 + (F_{v\_Tube})^2} \tag{17}$$

During the transverse deformation process, the total tube elongation can be computed using equation (18).

$$\delta = 2 \cdot \left(\left(\left(\frac{L_o}{2} \right)^2 + (\Delta y)^2 \right)^{0.5} - \frac{L_o}{2} \right) \tag{18}$$

Figure 32 presents the tensile load versus tube elongation from the observations acquired from test 3 and used in the above theoretical analysis. Additionally, Figure 32 also illustrates the tensile load versus tube elongation from an axial tensile test. It should be noted that the axial tensile load and tube elongation are determined directly from experimental apparatus and represent measures of the tube tensile force versus total elongation.

When comparing the force/displacement responses of the empty braided tube subjected to axial loading to empty braided tubes subjected to transverse loading, it is observed that the tensile stiffness of the braided structure is much lower in the transverse loading configuration. The tensile stiffness, for a specimen loaded in the axial direction was computed within the displacement domain between 10 mm to 40 mm while the tensile stiffness of a specimen transversely loaded was computed between 30 mm to 70 mm. The corresponding tensile stiffnesses for axial and transverse loading conditions were noted to be 711.98 kN/m and 337.63 kN/m, respectively. Specific to the transverse loading condition, the tensile stiffness is computed and not measured directly, yet such a measure

represents the tensile stiffness being the tensile force within the tube normalized with respect to the tube elongation. The reduced tensile stiffness of the structure is believed to be influenced by tow stack up at the tube mid-span and on the upper side of both clamps, while on the lower side of both clamps tow separation was noted, which would also reduce the mechanical load bearing capacity, thus reducing the stiffness. Additionally, near the vicinity of the upper portion of the clamp, yet slightly away from the clamp, a slight degree of buckling of the braided tows was noted to occur. Since the structure is in a state of compression near this location and the tows can only support a tensile load, the tows were observed to buckle as a result of the compressive forces on the upper side of the braided tube. The combination of tow stacking and localized buckling does not permit for the desired scissoring effect between neighboring tows and thus a reduced stiffness is observed. The calculated energy absorbed by the empty braided structure using the data acquired from the experimental apparatus (Figure 29), approximately equal to 2.5 kJ, is consistent to the energy absorbed by the structure if integrating the force/displacement response from Figure 32 under the transverse loading condition.

Examination of the nonlinear force/displacement response of the braided tube under axial and transverse conditions presents some interesting findings. A minor yet notable change in the mechanical response of the braided tube was noted to occur for displacements ranging from approximately 100 mm to 140 mm for specimens subjected to transverse loading and approximately 40 mm to 115 mm for specimens subjected to axial tensile loading. The linear hardening behaviour for the axially loaded specimen was noted to be a result of localized plasticity of the braided wires at contact locations between neighboring tows and also a result of tensile elongation of the entire structure. These deformations all occurred after tow lockup was well achieved throughout the entire specimen. The transverse specimen maintained a relatively constant load, of approximately 30 kN, after approximately 100 mm displacement of the centre loading bar. The relatively constant load is a result of the degree of braided tube deformation near the vicinity of the clamps. Early in the deformation process braid tows at the lower portion of the annular clamps are subjected to a large degree of elongation compared to other areas of the tube as a result of the geometrical conditions of loading. This causes

the lower portion of the tube, near the vicinity of the clamps, to experience tow lockup much earlier in the deformation process compared to other regions of the tube. At approximately 100 mm displacement these portions of the braided tube start to experience progressive failure as can be noted in Figure 29(e) near the right side clamp. The isolated failures of the braid tow strands within these regions do not permit the structure to accommodate any increase in load and thus produce a relatively constant load.

The tensile loads observed within the braided tube subjected to axial loading reached approximately 50 kN while the tensile loads observed within the braided tube subjected to transverse loading reached approximately 32 kN. The failure displacement was noted to be approximately 20 mm greater for the transverse loading case, which is associated with the progressive failure of the braided tubes on the lower side of the structure within the vicinity of the clamps. The mechanical response of empty tubes subjected to transverse loading permit a greater degree of tube elongation without a significant increase in tensile load. Contrary, the axial response of empty tube is able to sustain greater load under lower tube elongation, with only a minor degree of progressive failure observed. From these findings it is evident that the load bearing capacity of the braided tube is heavily influenced by the loading orientation.

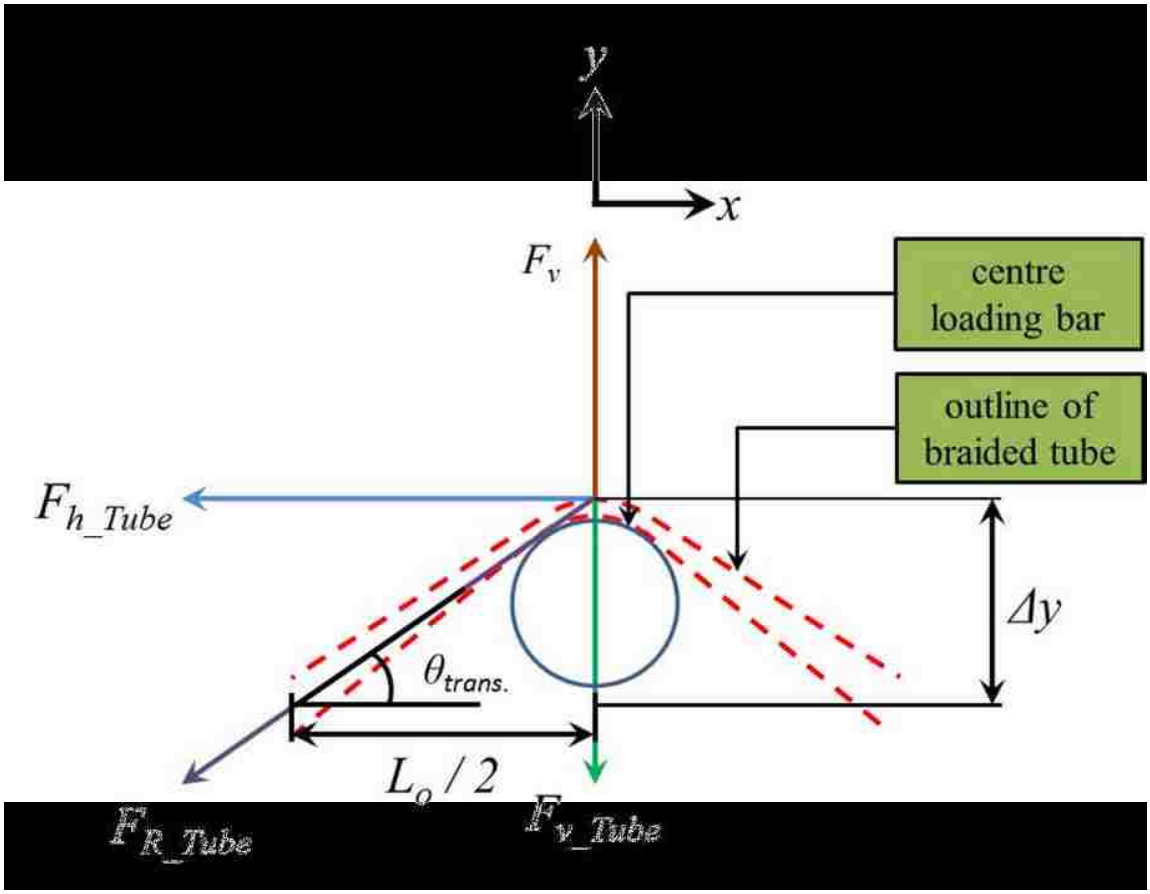

Figure 31: Front view configuration illustrating the forces acting on the empty braided tube during deformation.

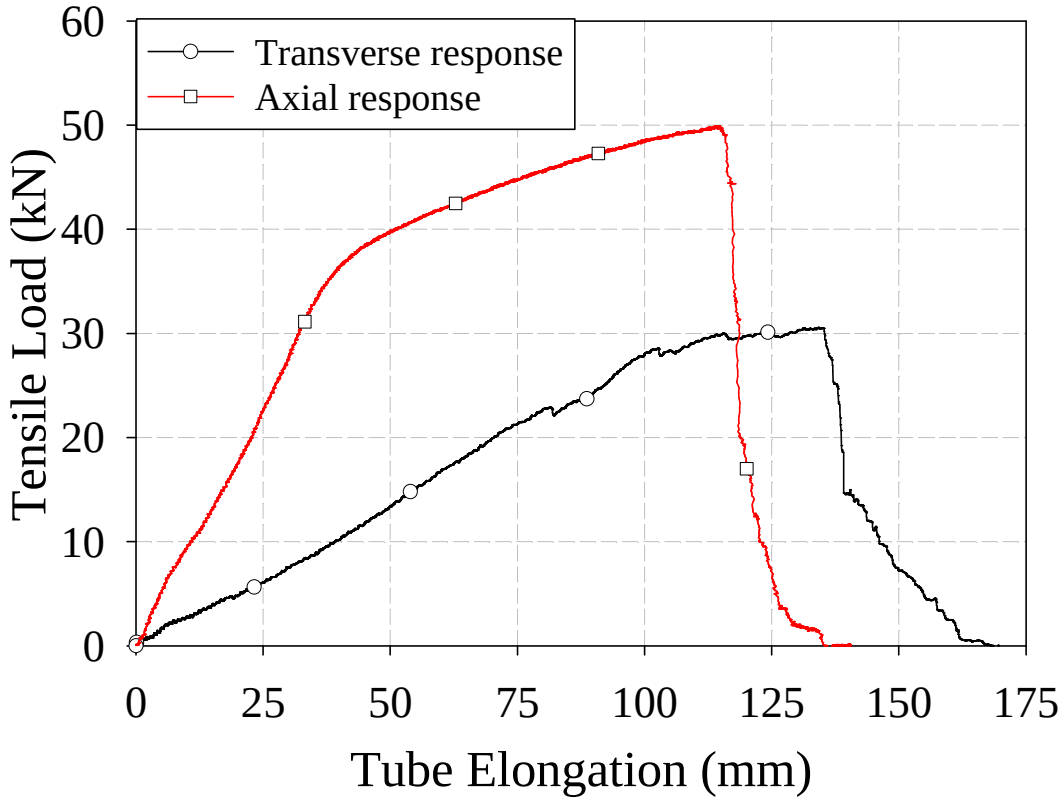

Figure 32: Tensile response as a function of tube elongation for axial and transverse loading conditions.

6.4.2 Transverse response of circular core foam filled braided tubes

This section presents the mechanical response, deformation mechanisms, and failure modes of braided tube specimens containing a circular foam core subjected to an applied transverse load. Figures 33 and 35 illustrate the transverse force versus displacement and energy versus displacement plots of braided foam assemblies. Photographs depicting the transverse deformation process of specimen 2, which utilized a high density core, are illustrated in Figure 34 and photographs of specimen 1, which utilized a low density core, are illustrated in Figure 36. Annotations in Figures 33 and 35 correspond to the images in Figure 34 and 36, respectively. Table 12 presents the average force, FE, TEA, and SEA of the braided assembly for a given test.

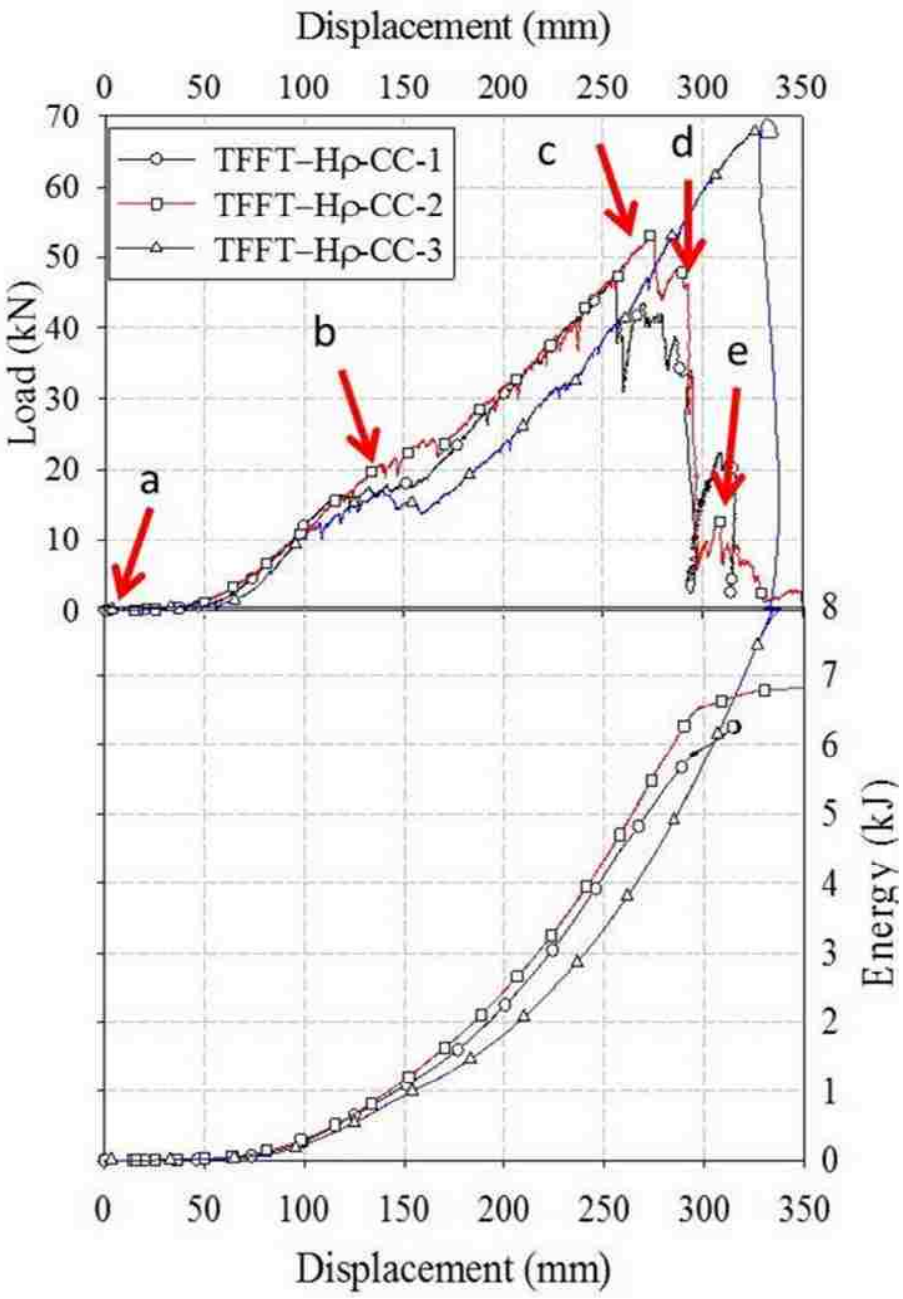

Figure 33: Force/displacement and energy/displacement responses for circular core, high density foam filled braided tube.

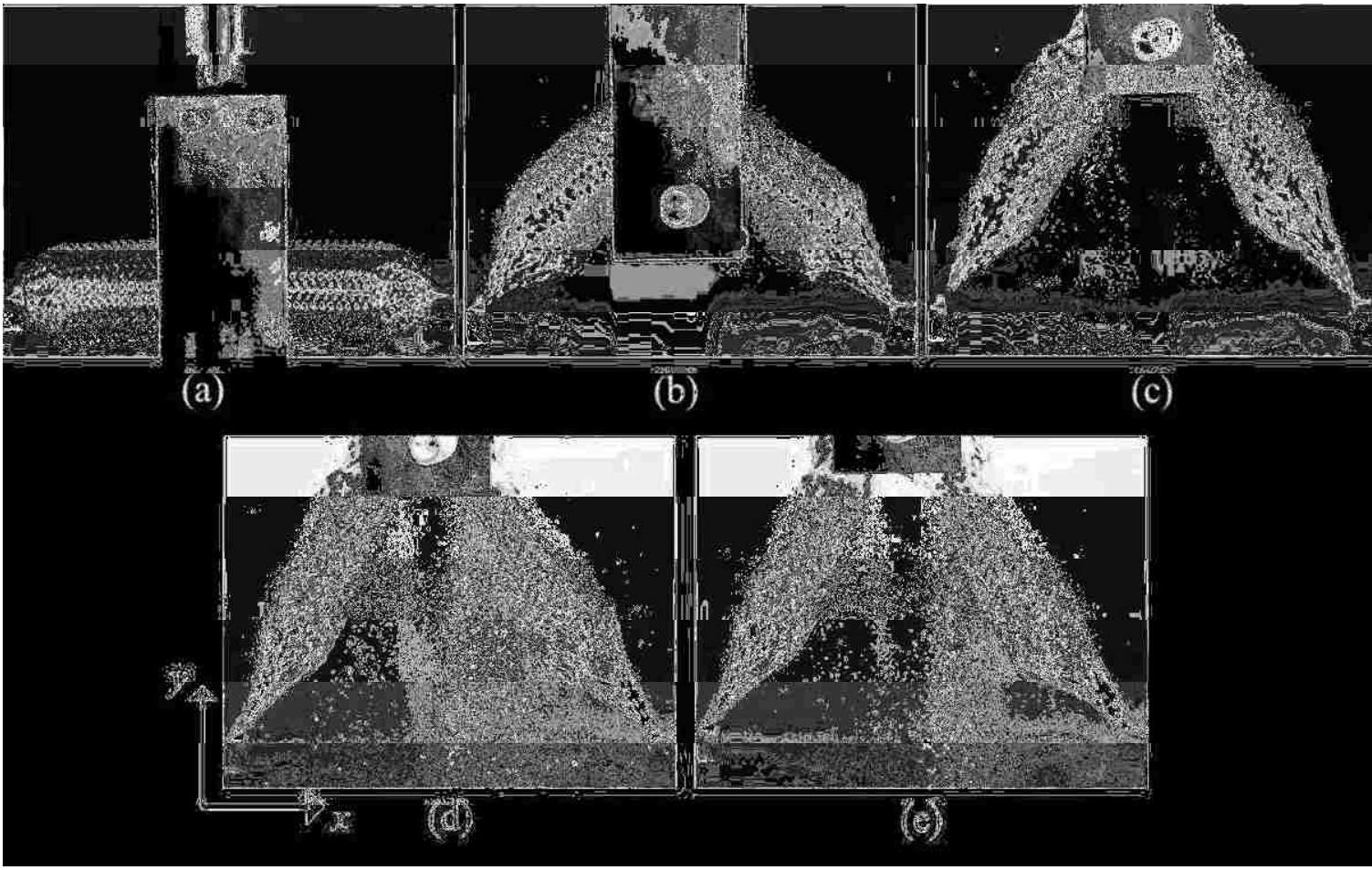

Figure 34: Photographs illustrating the transverse deformation process of the high foam circular core braided tube for specimen 2.

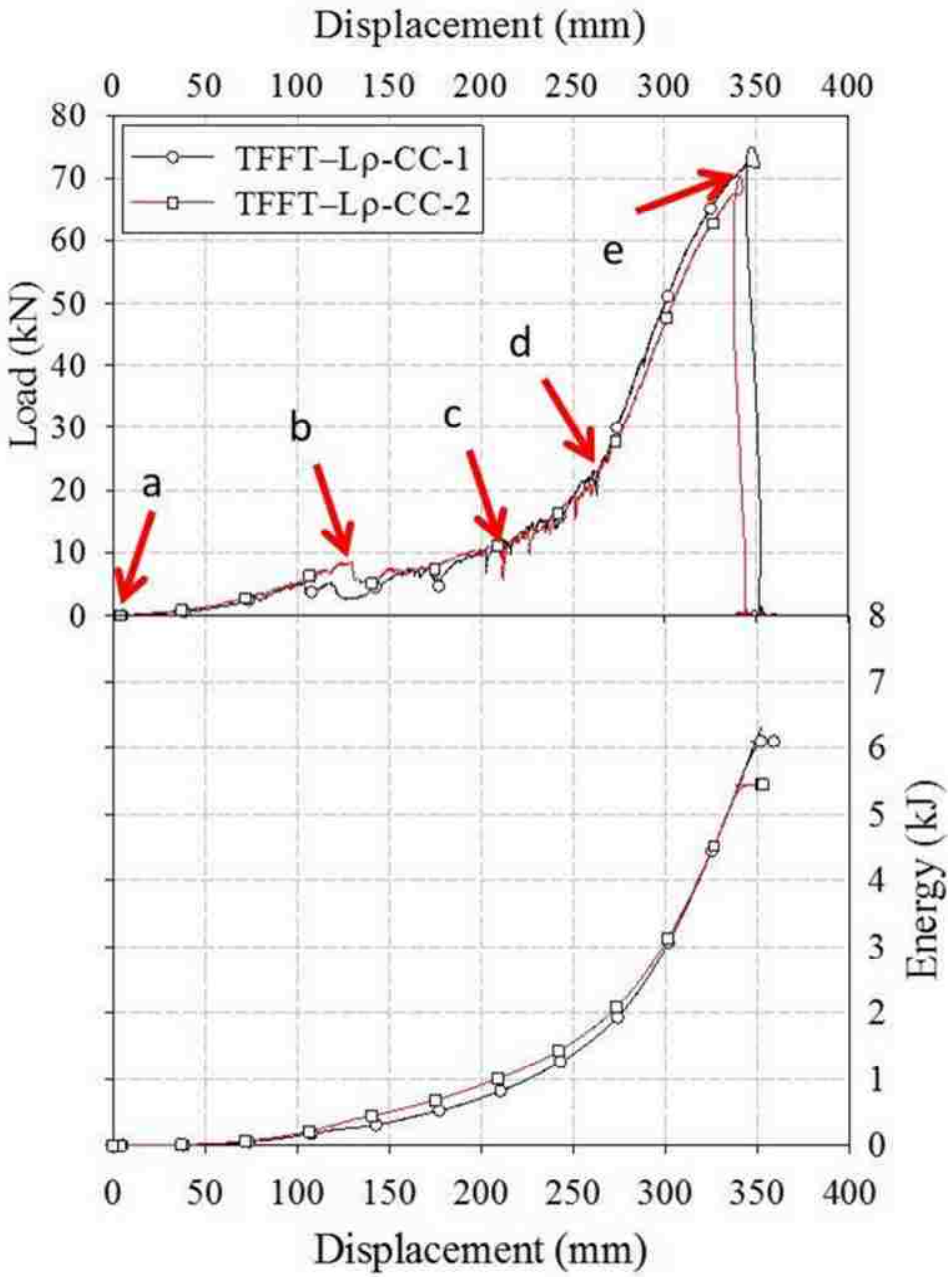

Figure 35: Force/displacement and energy/displacement responses for circular core, low density foam filled braided tube.

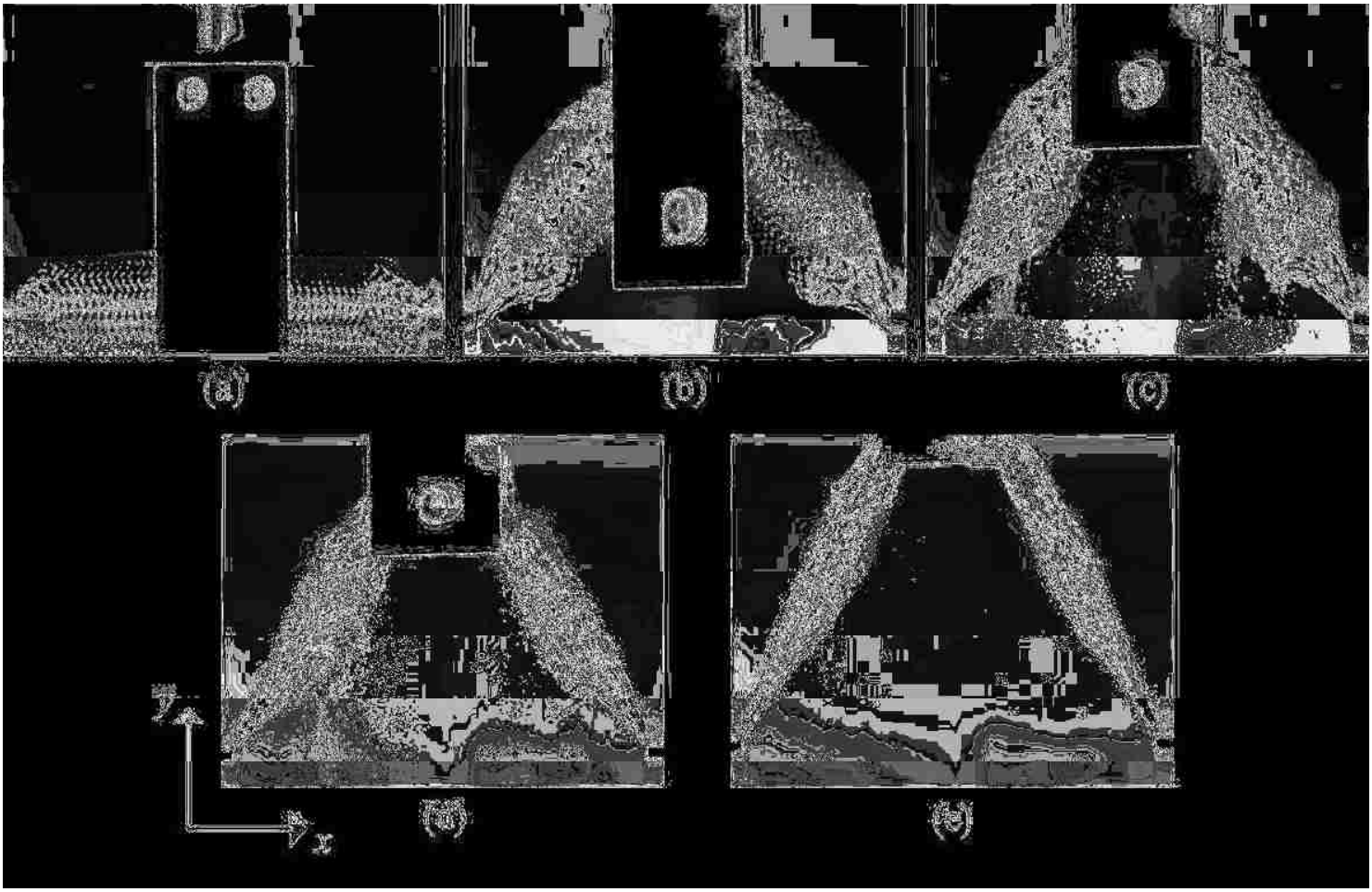

Figure 36: Photographs illustrating the transverse deformation process of the low foam circular core braided tube for specimen 1.

Photographs of the transverse deformation process illustrate immediate flattening of the braided structure at mid-span as a result of the braided tube conforming to the shape of the centre loading bar upon contact. The mechanical behaviour associated with this deformation was observed to follow a linear response up to approximately 2 kN within the displacement range of 0 mm to 50 mm. The load magnitude associated with this deformation was insignificant to the magnitude of loads observed for the remainder of the test.

Displacements beyond 50 mm, with specimens involving a circular core, resulted in occurrence of foam puck detachment, which was associated with both foam failure and breakdown of the adhesive, foam core crushing, and braid tube flattening occurring at the braided tube mid-span. The metallic foam core exhibited significant collapse at the mid-span and minor collapse within the straight sections of the braided tube which resulted in the observed oscillations within the measured load. These oscillations are independent of the foam density and occur until displacements of approximately 225 mm.

As evident in Figure 33, for the high density circular foam core specimens, the force/displacement responses exhibited a nonlinear behaviour at loads of approximately 20 kN and 125 mm of displacement. The corresponding photographs illustrating specimen deformation can be seen in Figure 34 (b)-(d). The nonlinearity is attributed to localized bending of the tube near mid-span as well as the foam crush of the cores, which have separated into two, or more, regions within the interior of the tube. Furthermore, foam crush at the ends of the cores is more pronounced due to the tight arrangements of tows in regions without foam. The displacement at the onset of nonlinearity is indicated by an arrow in Figure 33 with the letter (b). Post-test examination of the braided tube foam core assembly revealed that foam pucks located at the mid-span of the tube were completely pulverized. The foam pucks positioned within the straight sections of the braided tube assembly on either side of the centre loading bar were detached and separated from their neighboring pucks during the deformation process and typically not subjected to a similar amount of deformation.

Subsequent to the nonlinear response, a constant linear increase in the force was noted which ranged from approximately 23 kN to 45 kN corresponding displacements of approximately 150 mm to 260 mm. During this loading, the foam cores were observed to crush and a reduction in tube diameter was evident as well as stretching of the braided tube. The braided structure was observed to fail at the mid-span through a progressive deformation mode at approximately 54 kN for the second sample of three tested in this configuration. Variations in the ultimate failure strength were noted for this specimen configuration. Ultimate strengths varied from approximately 48 kN to 68 kN. Discrepancies in the observed ultimate strengths and displacements to failure are related to the high density core specimens interacting/contacting the braided tube and resulting in stress concentrations from kinking of the wires and contact. As a result of this chaotic behaviour, variations in the ultimate strength and elongations are observed.

Necking of the braided tube assembly, in regions outside of the mid-span of the specimen, did not occur for tests incorporating high density foam core specimens to any significant extent. Additionally, after the progressive failure of the braided tube assembly, it was noted that the internal foam core was not completely crushed. It is hypothesized that the compressive strength of the high density foam cores mitigates any form of localized foam crush outside of the mid-span of the specimen and inhibits thorough foam crush. As evident in Figures 34(d) and 34(e), pulverized metallic foam was noted to exist at the mid-span of the specimen and was ejected from the tube once tow failure initiated.

Figure 35 presents the force/displacement observations for the low density foam core test samples. Observations indicate that the force/displacement response increases gradually compared to specimens utilizing a high density foam core. Low density foam filled braided tubes experience complete foam crushing and tow lockup throughout the tube's length. However, a rapid reduction in the load bearing capacity of the structures occurred at approximately 7 kN corresponding to a displacement of approximately 125 mm (location "b" of the annotated force/displacement graph in Figure 35). At this point of loading decoupling of the foam pucks, near the vicinity of the structures mid-span, occurred causing a discontinuous loading response. Similar fluctuations in the loading

characteristics are apparent where foam crushing region occurred over displacements ranging from 150 mm to 250 mm. In addition, foam puck detachment and full foam crushing was noted after post-test examination of the braid tube/foam core assembly. The maximum force and total elongation are both greater than findings associated with high density foam core specimens. However, overall energy absorption capabilities were lower for specimens incorporating a low density foam core due to the lower degree of load bearing capacity for the majority of the displacement domain.

Examination of the high speed photographs associated with the loading of the low density foam filled structures (Figure 36(a)-(e)) illustrated braid tube flattening, at mid-span, which resulted in foam core crushing early in the deformation process. Localized necking of the braided tube was observed, but to a minor amount. Without the presence of any significant localized necking occurring within the braided tube, no substantial stress concentrations are imposed on the tows and correspondingly the elongation and maximum load are both increased, compared to specimens incorporating high density foam. Little or no necking occurrence in the low density foam core tests eliminates potential local stress concentrations along the length of the braided tube. Progressive failure of the braided tube assembly was noted to occur rapidly with only minor increases in the displacement. Complete pulverization of the foam core was noted.

The compressive forces generated by the diameter reduction of the braided tube are adequate to fully crush the internal foam core in a uniform and continuous fashion throughout the braided tube length. Moreover, as the braided tube is displaced in the *y*-axis direction, the tows experience tow lockup throughout the length of the tube. For specimens containing high density cores, such an observation was typically not noticed.

For comparison purposes, Figure 37 illustrates the force/displacement response representing specimens of high and low diameter cores. The regions of the force/displacement response which are highlighted indicates the displacement domain used in determining the average force. It should be noted that during the deformation process, the braided tube typically experiences elastic deformation with significant tow

scissoring while crushing the foam core. Beyond $\delta_{critical}$ plastic deformation of the braided tube tows occurs and is the main contributor to energy absorption of the structure. The average force was used in computing the FE, which is presented in Table 12. The observed mechanical response for low density foam cores, where no significant load increase occurs over a significant degree of elongation, is favoured in applications where controlled load is required, for example automotive side door beams for impact.

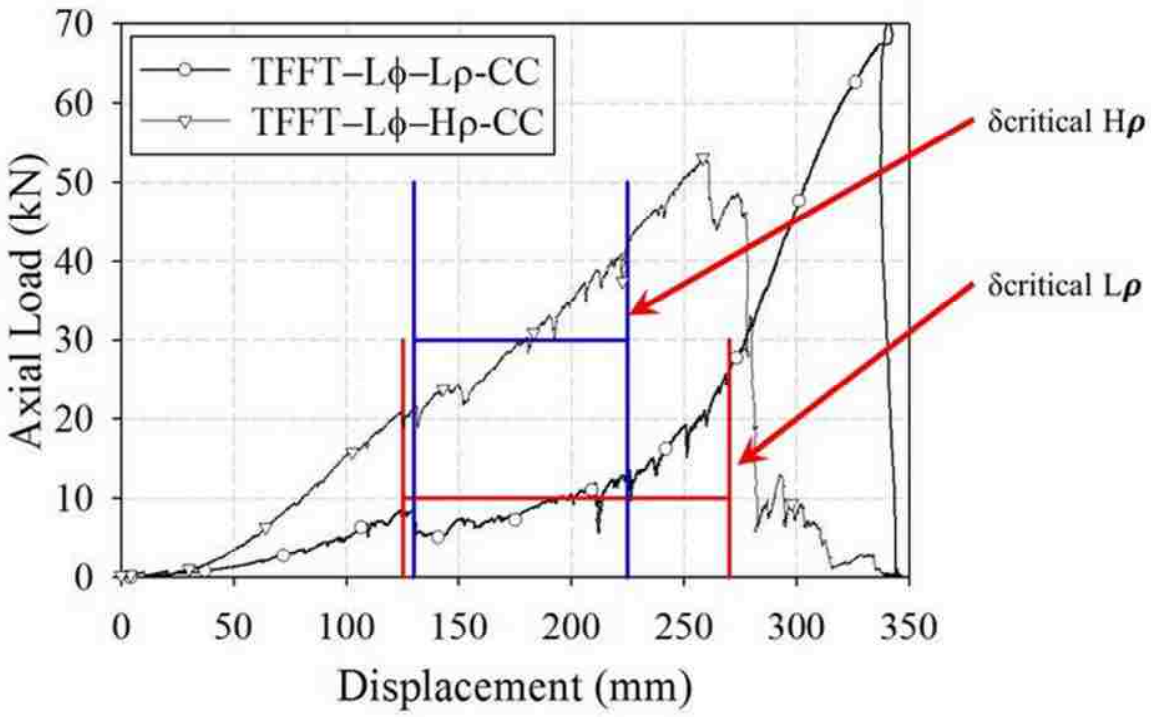

Figure 37: Overlay of high and low density profiles articulating average force for circular core prisms.

Referring to Figure 37, the force/displacement response for specimen with low density foam core exhibited a gradual nonlinear increase within the foam core crushing phase. The foam crush phase is evident in regions where a brief reduction in load occurs but the load behaviour quickly returns to previous magnitudes. The average force to crush the foam core was observed to increase in the foam crushing phase which was initiated at approximately 125 mm and terminated at approximately 270 mm ($\delta_{critical}$) of displacement. Within this range, the computed average force was 23.4 kN. Contrary, the

force/displacement response, within the foam crushing phase, for specimens containing a high density foam core increased in a rapid yet somewhat linear manner. The foam core crushing phase ranged between 130 mm to 225 mm of displacement and the corresponding measured transverse load ranged between 20 kN to 40 kN. The computed average force to crush the foam core was 24.14 kN. It was noted that the failure or catastrophic load of the structure containing low density foam core was significantly larger than specimens containing high density foam core by approximately 20 kN.

The averaged TEA for specimens containing high density foam cores and those containing low density foam cores was determined to be 7.03 kJ and 5.79 kJ, respectively. The average FE was found to be 38.2% and 23.8%, respectively.

The average force was observed to be higher, by approximately 4.68 kN, for specimens containing high density foam cores compared to specimens having low density foam cores. It was noted that the average force increased with an increase in the density of the foam core. The SEA was noted to be consistent for specimens having common high or low density foam cores; however, an increase of approximately 0.5 kJ/kg was noted for the high density foam core specimens. Similar values of the average SEA was noted between specimens encased with low density foam core and empty braided tubes (5.51 kJ/kg and 5.72 kJ/kg, respectively). The SEA for high density foam filled braided tubes was observed to be higher, by approximately 0.65 kJ/kg, when compared to empty braided tubes.

6.4.3 Transverse response of rectangular core foam filled braided tubes

Figures 38 and 40 present the force versus displacement and energy versus displacement response of specimens incorporating rectangular foam cores. Photographs depicting the transverse deformation process of specimen 3, which utilized a high density core, are illustrated in Figure 39 and photographs of specimen 1, which utilized a low density core, are illustrated in Figure 41. Annotations in Figures 38 and 40 correspond to the images in Figures 39 and 41, respectively. Table 13 presents the average force; FE, TEA, and SEA which are computed as discussed in section 5.4.2.

The force/displacement response, as depicted in Figure 38, illustrates an initial load reduction at approximately 6 kN of force and 45 mm of displacement as indicated by arrow (b). This load reduction was a result of the fracturing of the foam core due to the bending which the interior core was subjected to. Subsequent loading resulted in further fracture of the foam core causing a minor load reduction in the mechanical response at approximately 8 kN and corresponding to a displacement of 125 mm, as indicated by arrow “c”. The majority of energy absorption occurs beyond these load reductions.

For specimens incorporating high density cores, a combination of (1) braid tow scissoring, lockup and elongation at the annular clamp and mid-span regions ensues immediately followed by (2) foam fracture and (3) foam crush following the application of the transverse load. Significant crushing of the foam core was noted to occur at displacements greater than 50 mm. The deformation mechanisms of the high density rectangular cores, as presented in Figure 39, were observed to be complete foam crushing at mid-span of the structure and substantial foam crushing throughout the straight sections of the braided tube as a result of braid diameter reduction by transverse elongation without noticeable necking.

Photographic evidence of the deformation characteristics presented in Figure 39(e), illustrate that the foam core was significantly crushed to the extent that the braided tube experienced tow lockup throughout the two straight sections at either side of the centre loading bar.

For specimens utilizing low density foam core, fracture and crushing of the foam prism at the mid-span immediately occurs following the application of the transverse load as presented in Figure 41(b). Within the immediate loading stages, a minor load reduction at approximately 2 kN and 30 mm cross head displacement resulted in fracture of the foam core, depicted in Figure 40. Further loading results in foam crushing occurring over the displacement range of 50 mm to 225 mm. Photographs presenting the transverse tensile deformation process, depicted in Figure 41, illustrate complete foam pulverization occurring uniformly throughout the braided tube. The degree of diameter reduction was

more significant for low density rectangular cores compared to high density cores of similar geometry.

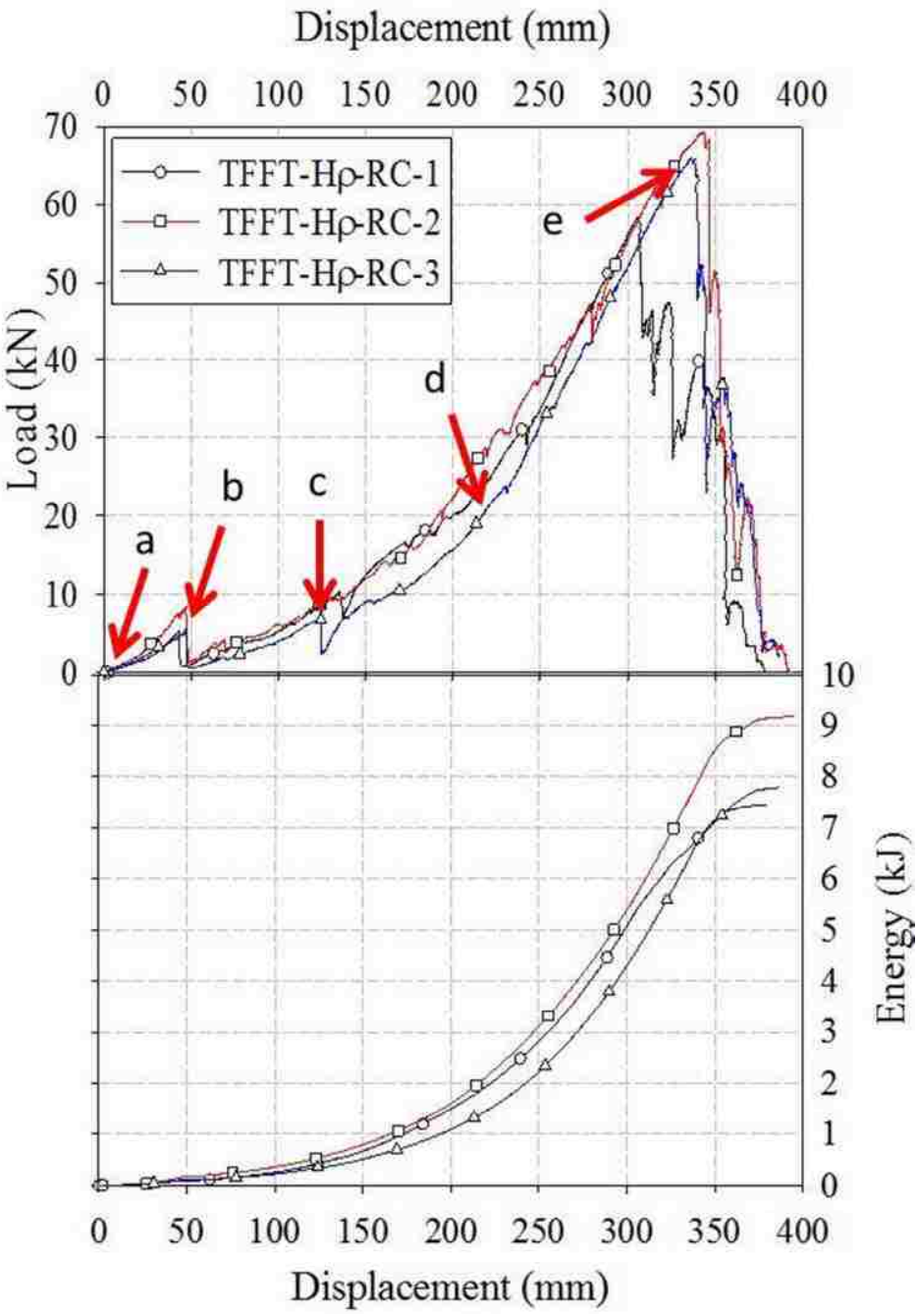

Figure 38: Force/displacement and energy/displacement responses for rectangular core, high density foam filled braided tube.

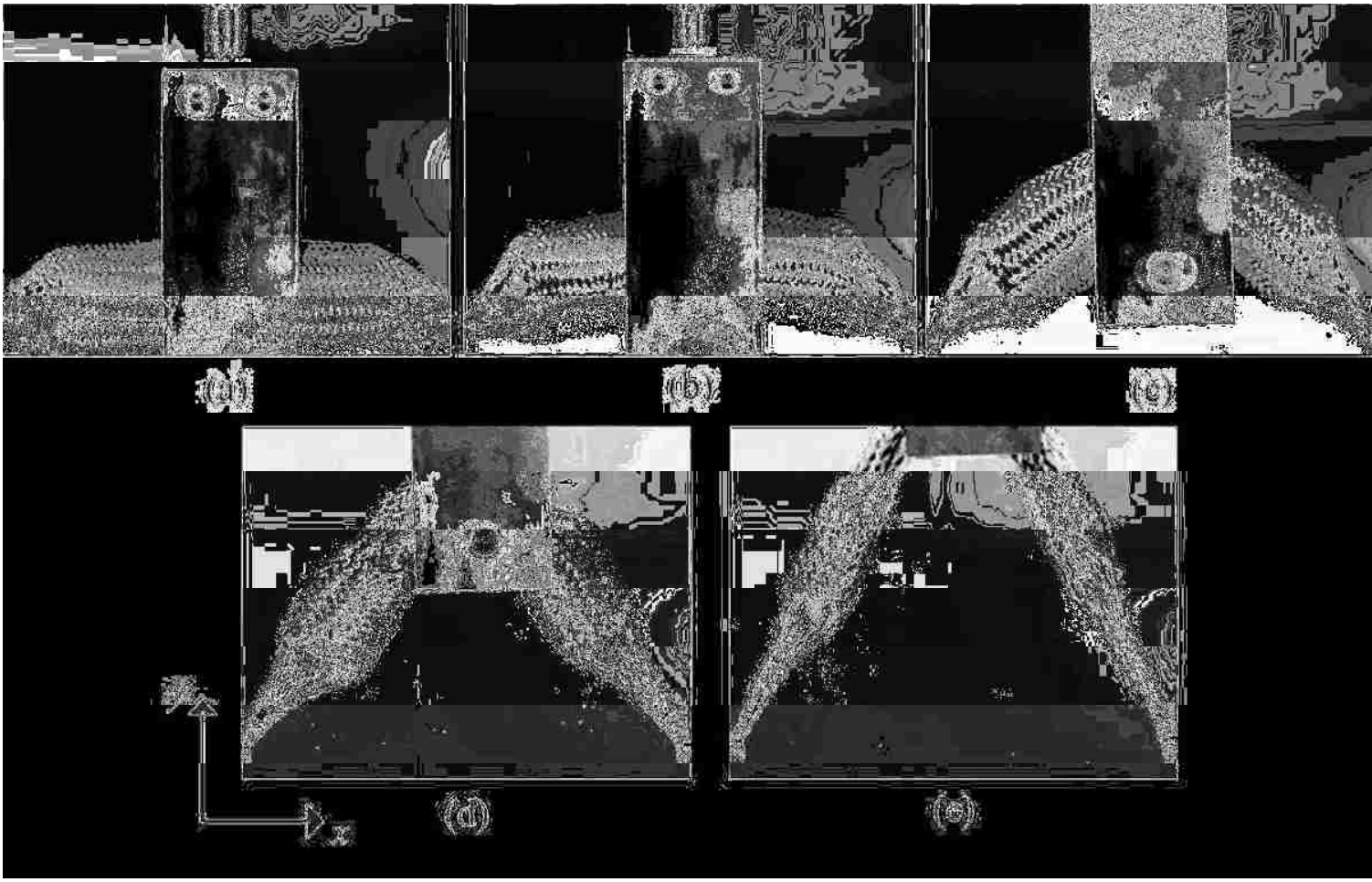

Figure 39: Photographs illustrating the transverse deformation process of the high foam rectangular core braided tube for specimen 3.

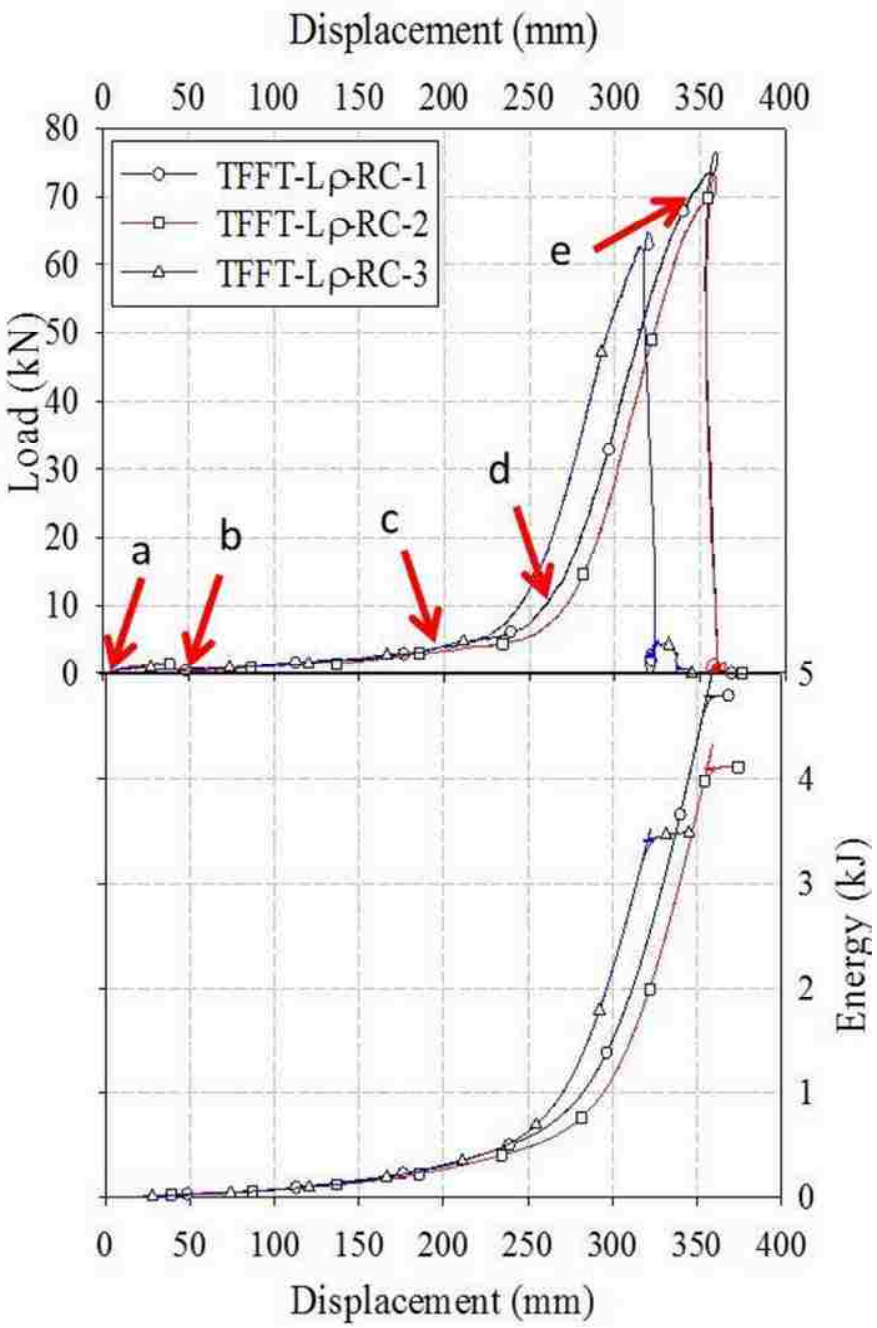

Figure 40: Force/displacement and energy/displacement responses for rectangular core, low density foam filled braided tube.

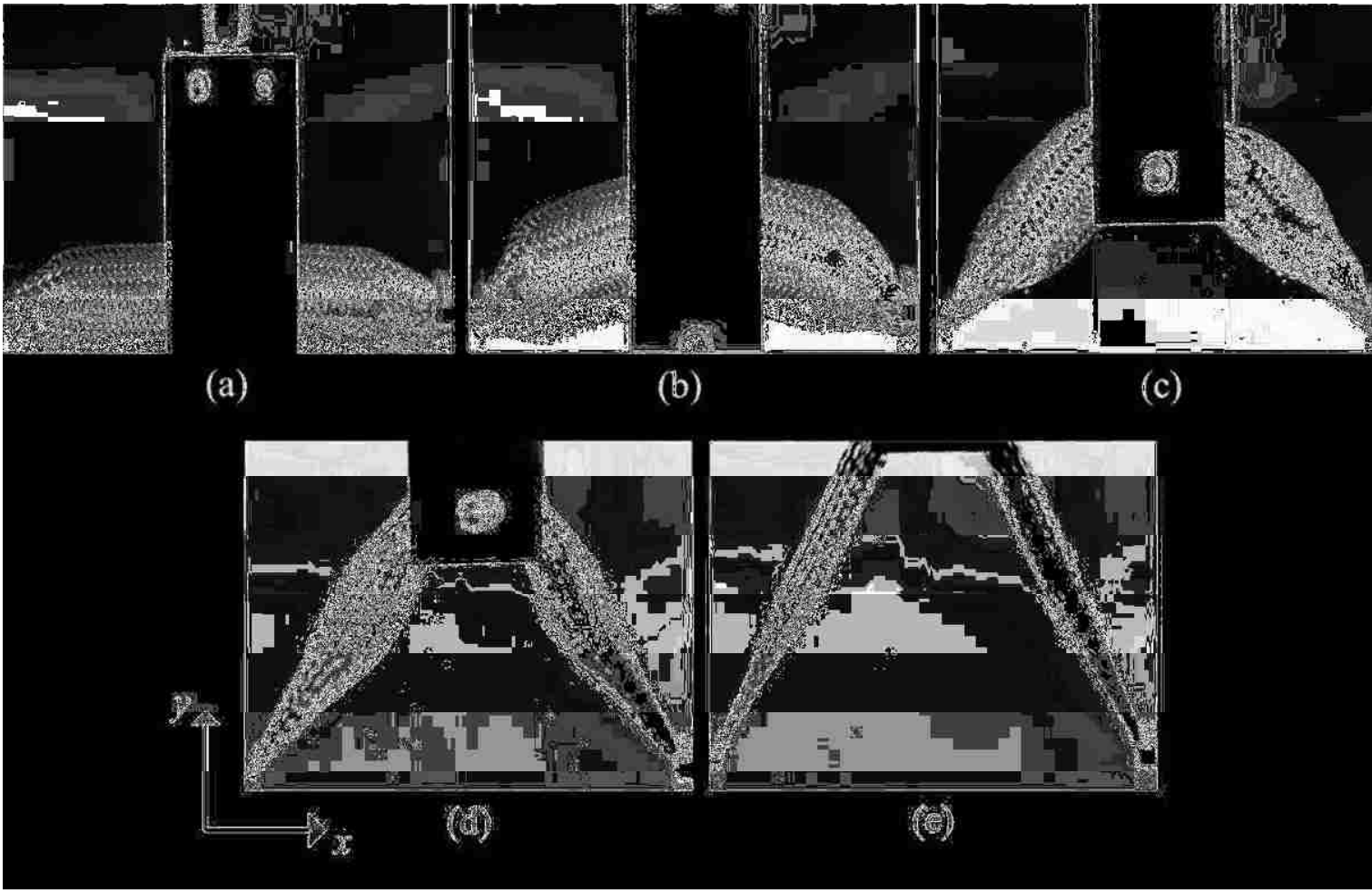

Figure 41: Photographs illustrating the transverse deformation process of the low foam rectangular core braided tube for specimen 1.

Figure 42 presents the force/displacement responses of low and high density rectangular foam filled braided tubes. Similar to Figure 37, the value of $\delta_{critical}$ is illustrated in Figure 42 as well as the range of displacement where the evaluation of the average force was computed for each specimen. The displacement at which $\delta_{critical}$ is noted for low density foam cores occurs at approximately 60 mm greater than the high density foam core specimens. The reduced mechanical strength of the low density foam core permits a greater degree of core crush without any significant increase in load. Within the displacement range used to assess the average force for braided tubes incorporating a low

density core, the mechanical response is noted to be generally linear with no significant fluctuations indicating uniform and progressive crushing of the foam core.

The photographic evidence presented in Figures 34 and 39, indicates for specimens utilizing a cylindrical or rectangular high density foam core, the elevated mechanical strength of the core does not allow for a uniform foam crushing process to occur. Correspondingly, foam puck separation, resulting in necking of the braided tube, and foam core fracture, near the vicinity of the mid-span of the structure, result in significant and notable fluctuations in the mechanical response.

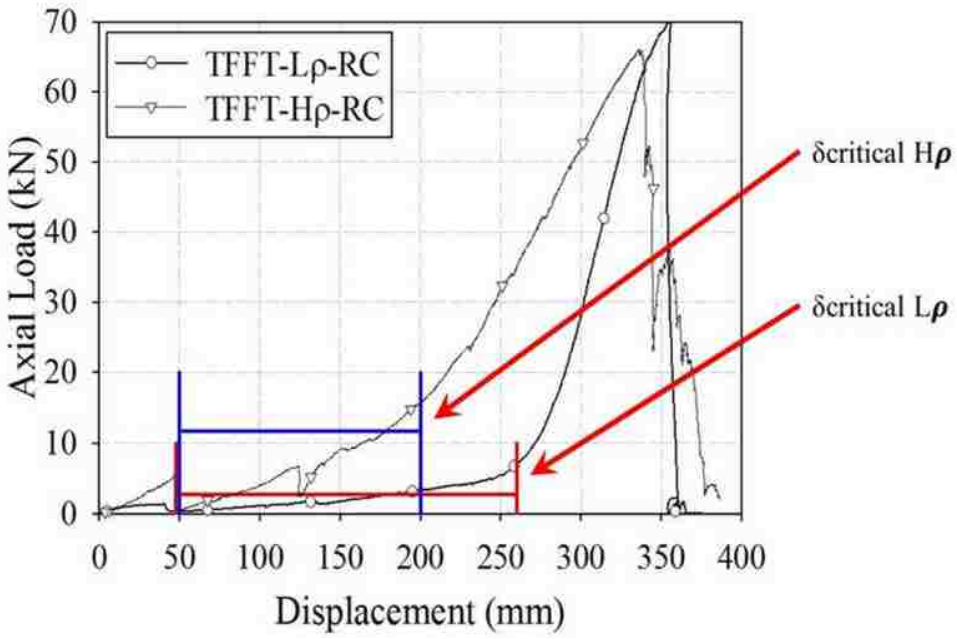

Figure 42: Overlay of rectangular core high and low density profiles articulating average force.

Experimental observations of the TEA and FE (in Table 13) for the specimens utilizing high density foam cores ranged from 7.44 kJ to 9.13 kJ and from 30.5% to 33.6%, respectively. When examining the degree of displacement required to initiate tube failure in specimens incorporating high density rectangular foam cores, it was noted that there was a slight variation of approximately 40 mm between tests 1-3 as illustrated in Figure 38. It is hypothesized that this observed variation is most likely due to geometrical

imperfections in the foam core and braided tube. The corresponding influence of these imperfections on the TEA was observed to be minor for specimens employing high density rectangular foam cores; however it did influence the FE to a greater degree. Additionally, a variation of approximately 30 mm in the displacement domain at specimen failure was also observed for the specimens utilizing low density foam cores, as depicted in Figure 40. It was found that for specimens incorporating low density foam cores, the mechanical strength of the core typically reduced the average force by approximately 55% compared to specimens incorporating high density cores as detailed in Table 13. Examination of the S.E.A values, presented in Table 13, for specimens containing high and low density foam cores indicates slight variation with no significant influence on the density of the foam core. This can be attributed to a uniform deformation throughout the tube leading to consistent observed progressive failure at the mid-span of the braided structure.

With respect to the energy absorption, the specimens containing circular foam cores proved to be more efficient in terms of SEA. Approximately 35% reduction in SEA was determined for specimens containing a rectangular core compared to circular cores. However, specimens containing rectangular foam cores were observed to be more compliant. Specimens containing rectangular foam cores were found to be less sensitive to factors such as slight misalignment or shifting of the internal foam core during the deformation process. The SEA for specimens incorporating a circular foam core was approximately 2 kJ/kg greater than rectangular cores. In most applications, it is desirable to achieve the highest SEA possible due to frequent limitations associated with structure size.

7 VARIABILITY ANALYSIS RESULTS AND DISCUSSION

A brief variability analysis of the findings presented in Tables 6, 7, 9, 10, 12 and 13 are presented within this chapter. The analysis has been completed for the findings from the compression testing of the aluminum foam specimens as well as the findings from the tensile and transverse testing of the aluminum foam filled braided tubes. Within the three figures of this section, the configuration type, for a given testing condition, is presented in Figures 43(a)–(c), Figures 44(a)–(c), and Figures 45(a)-(c). Within Figures 44 and 45, the variability in reference to Tables 9, 10, 12, and 13 is used to assess the parameters FE, TEA, and SEA on the tensile and transverse testing of aluminum foam filled braided tubes and their connection with the variability in the aluminum foam core configurations. Variations in the observed findings for the compression testing (Tables 6 and 7), tensile testing (Tables 9 and 10) and transverse testing (Tables 12 and 13) are presented within these figures. Information contained within these plots includes maximum, minimum, median, mean, and range bars for each variable for a given configuration. The range bars indicate the difference between the maximum and minimum value for each configuration. It should be noted, although a small number of transverse tests are completed for some configurations, such information is helpful to understand the variability of the mechanical response of these composite structures.

7.1 Foam compression testing

Figure 43(a) illustrates the elastic modulus as a function of configuration type for the compression test findings of the aluminum foam specimens. Regardless of core geometry, the low density foam core configurations exhibit a minor degree of variability between the three tested samples within each group. The mean values ranged from approximately 11.72 MPa, for Lρ-RC, to 36.98 MPa for Hø-Lρ-CC. Configuration groups Lø-Hρ-CC and Hρ-RC had the largest variability ranging from 97.6 MPa to 158.61 MPa and 139.81 MPa to 201.54 MPa, respectively. Although an analysis linking the foam cell size, cell shape, cell size distribution and manufacturing aspects of the metallic foam to the observed variation was not completed, it is expected that these parameters play a significant role in the observations and their variation.

Figure 43(b) illustrates that the mean of the plateau stress for the low density foam core specimens possesses a minor degree of variability. A greater degree of variation in the mean values of the plateau stress for high density foam core configurations was noted. However, with the exception of Hρ-RC, a small degree of variation within a given configuration was observed.

The densification strain as a function of configuration type, as presented in Figure 43(c), was noted to exhibit significant variation for the Lø-Lρ-CC test group. The maximum and minimum values ranged from 24.2% – 44.4% with a mean value of 34.57%. Configuration types Hø-Lρ-CC and Lρ-RC illustrated low variability, ranging between 38.6% to 40.1% and 41.2% to 43.3%, respectively. It was observed that the densification strain for all foam configurations, at low and high densities, ranged between approximately 30% and 43%.

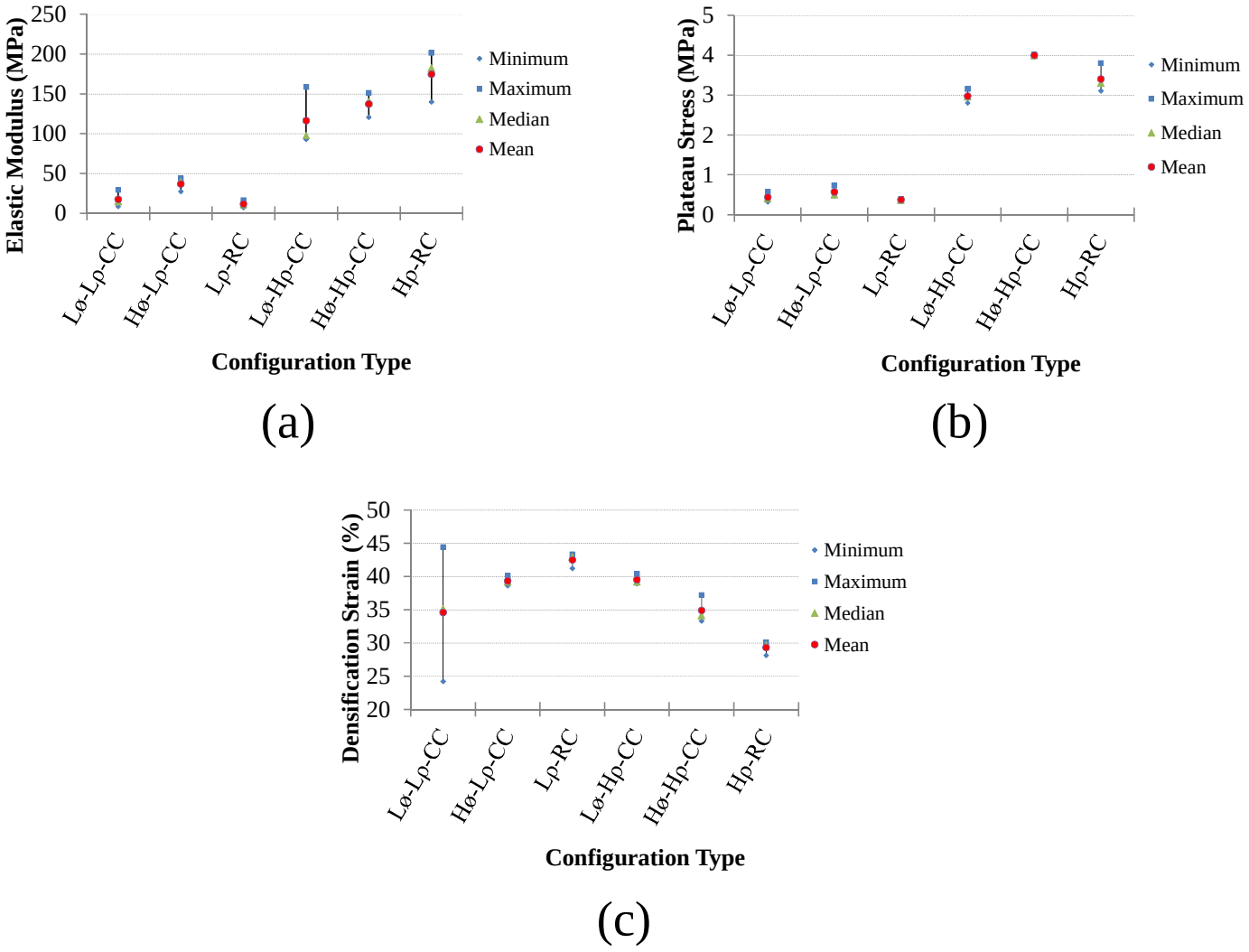

Figure 43: Maximum, minimum, median, mean and range for low and high density foam core configurations as a function of (a) elastic modulus, (b) plateau stress, and (c) densification strain observed from compression testing of the metallic foam.

7.2 Tensile testing of aluminum foam filled braided tubes

Figure 44(a) presents the findings of TFE as a function of configuration type. A lower mean value of the TFE for all low density foam core configurations was noted when compared with the high density foam core configurations. However, a greater degree of variation in the high density configurations was observed to exist. For the low density foam core configurations the mean values of the TFE was observed to range from 1.63%

to 14.23%. The range of TFE for the Lρ-RC configuration exhibited the lowest degree of variation having values ranging between 1.24% and 2.08% with a mean of 1.63%. For the high density foam core configurations the TFE was noted to range between 28.03% to 71.28%. For the high density foam core configurations a minor degree of variability, within each configuration, was noted to exist, although this was somewhat larger than the low density foam configurations.

Figure 44(b) presents the values of the TEA versus configuration type for foam filled braided tubes. The TEA for all specimen configurations was noted to vary between approximately 6.5 kJ and 11 kJ. While a lower degree of variation was observed for the low density configurations, which were observed to exist within the range of approximately 7.5 kJ to 9 kJ, the high density configurations varied within this range and beyond both lower and upper values. As noted in the manuscript, these inconsistencies are most likely associated with a significant interaction effect between the high density foam cores and the braided tube. The minor degree of variability observed between low density configurations provides indication that the low density test samples exhibit a consistent mechanical response.

Figure 44(c) indicates that the low density foam core configurations exhibited a very consistent mean SEA ranging from 7.94 kJ/kg to 7.98 kJ/kg. Importantly, the SEA for the lower density foam configurations exceeded those values of all specimens which utilized a high density foam core. Furthermore, the low density foam cores provide SEA improvements of the entire structure because of their crushing characteristics as mentioned in Section 3.3. The mean values of the SEA for the high density foam core configurations was noted to vary between approximately 5 kJ/kg and 6 kJ/kg, although a greater range of the SEA was noted within each high density foam specimen configuration grouping.

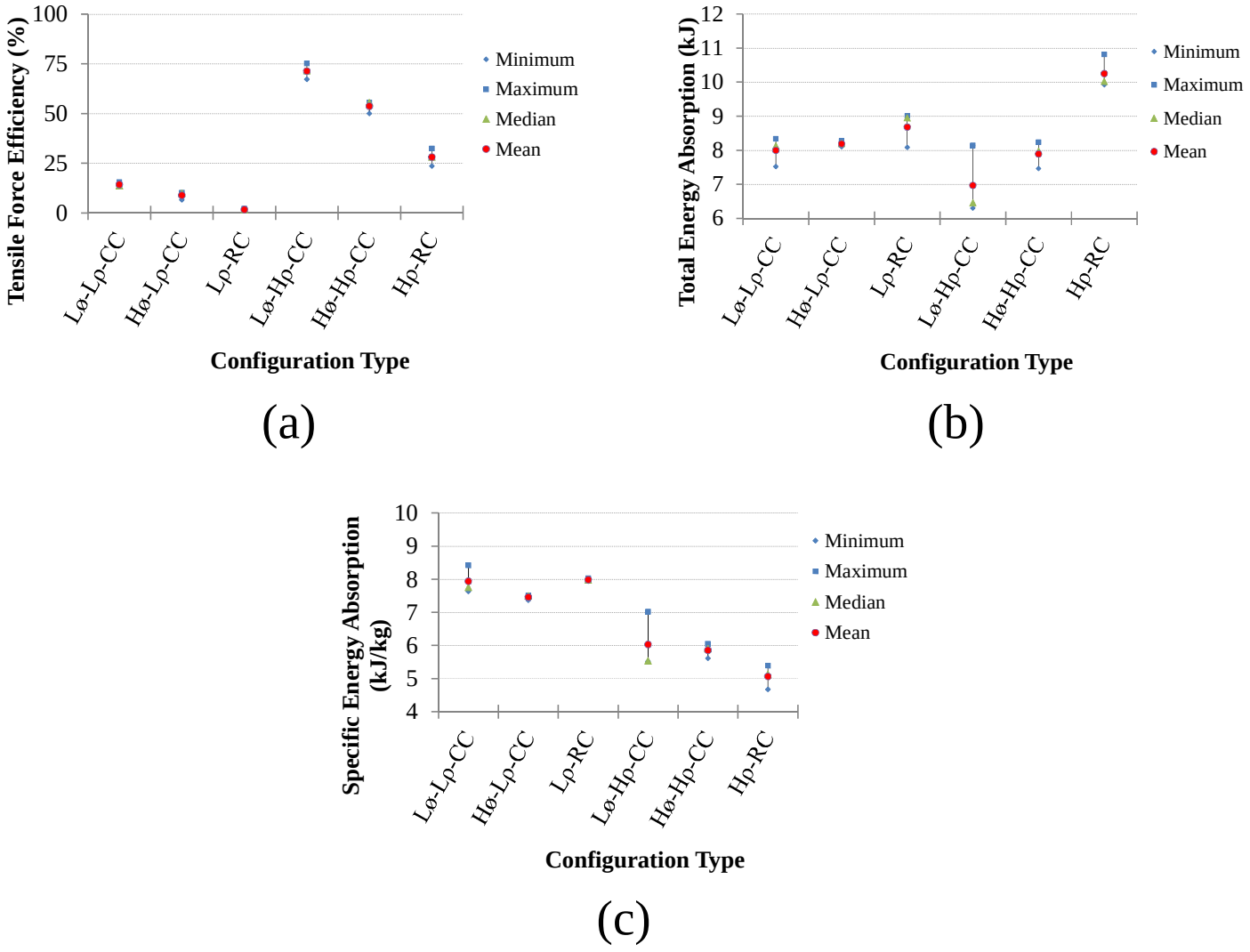

Figure 44: Maximum, minimum, median, mean and range for low and high density foam filled braided tube configurations as a function of (a) TFE, (b) TEA and (c) SEA

7.3 Transverse testing of aluminum foam filled braided tubes

Figure 45(a) presents the findings of FE as a function of configuration type. It was observed that for all specimens incorporating low density foam cores exhibited lower mean F.E compared to all specimens incorporating high density foam cores. The range of mean values varied between 17% to 38%. A greater degree of variation in the high density configurations was evident. For the low density foam core configurations the

mean values of the FE was observed to range from 16.20% to 24.20%. The range of FE for the Lρ-RC configuration exhibited the lowest degree of variation having values ranging between 16.20% and 18.6% with a mean of 17.07%. For the high density foam core configurations the FE was noted to range from 30.50% to 41.60%. For the low density foam core configurations a minor degree of variability, within each configuration, was noted to exist. It is important to note that specimens incorporating rectangular (high and low density) foam cores illustrated a lower mean value compared to specimens utilizing circular (high and low density) foam cores.

Figure 45(b) presents the values of the TEA versus configuration type for foam filled braided tubes. The mean TEA for all specimen configurations was noted to vary between approximately 4 kJ and 8.5 kJ. The degree of variation between low density configuration and high density configuration was observed to be approximately 3.51 kJ to 6.16 kJ and 6.19 kJ to 9.13 kJ, respectively. The variation range, for both low and high density configurations, is consistent at 2.65 kJ and 2.94 kJ. No conclusions can be stated regarding the variation as a function of core type (either cylindrical or rectangular prism).

Figure 45(c) indicates that there exist somewhat similar values of the mean SEA as a function of foam core geometry type. For example, similar values of the SEA for low and high density rectangular configurations, namely 3.81 kJ/kg and 4.14 kJ/kg, respectively, were observed. Similarly, low and high density circular configurations exhibited similar values of their mean SEA, being 5.72 kJ/kg and 6.15 kJ/kg, respectively. Thus, it is evident that circular foam core configurations exhibit an elevated SEA compared to the other foam core configuration considered in this research.

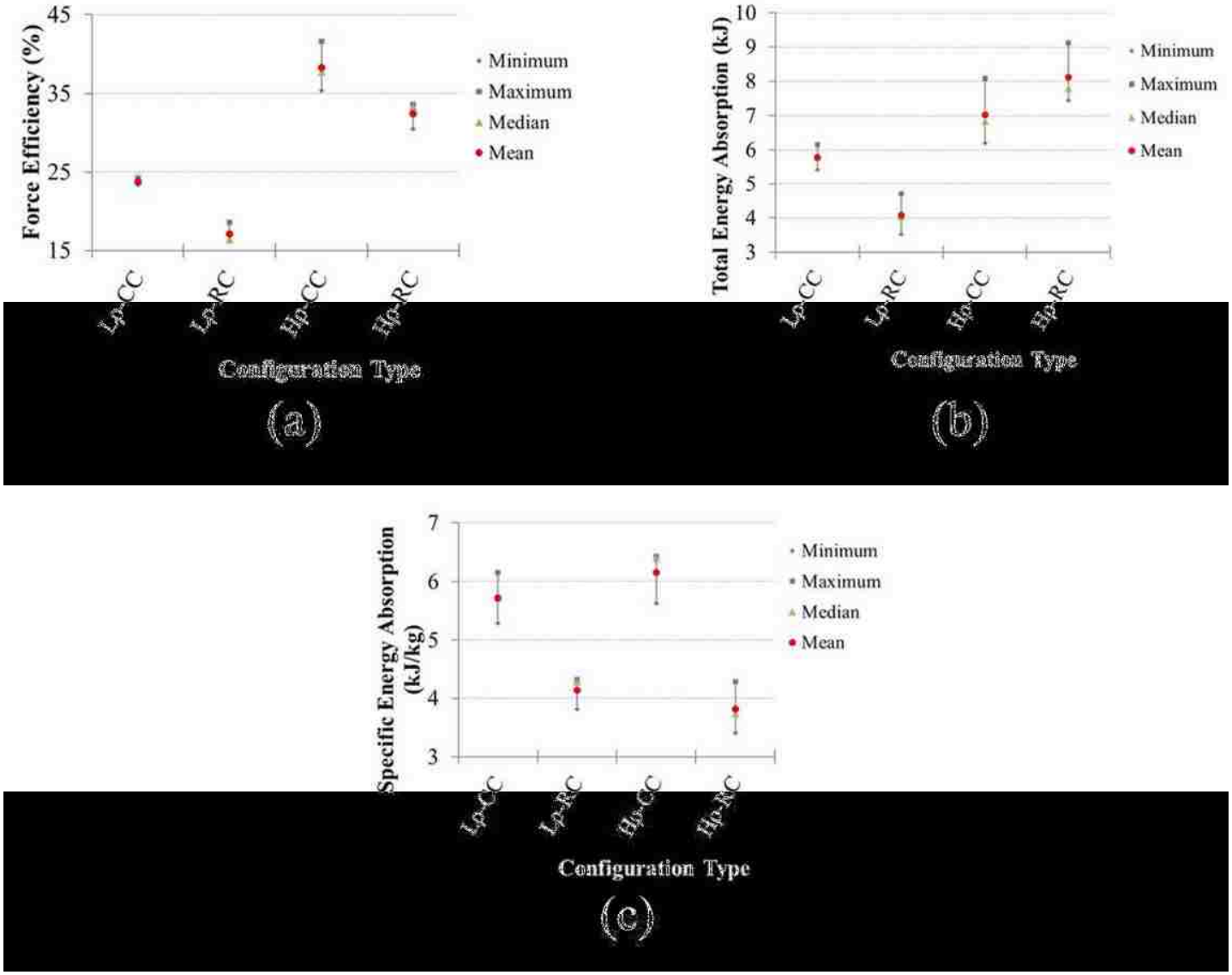

Figure 45: Maximum, minimum, median, mean and range for low and high density foam filled braided tube configurations as a function of (a) FE, (b) TEA and (c) SEA

8 CONCLUSIONS

8.1 Conclusions for uniaxial testing of aluminum foam filled braided tubes

This experimental investigation involved an analysis of the braid/foam system for energy absorption under uniaxial deformation. The use of digital tracking software ProAnalyst was used to track the tube deformation to obtain a radius versus length relationship to validate the analytical model developed by Cheng et al. [16]. High speed photographic images provided an examination of the tow kinematics and deformation during tube elongation. In addition, circular and rectangular foam cores were employed in this research to understand the full behaviour of the system upon elongation. The main findings from the investigation include the following:

1. The dominant failure mode for circular foam cores is neck propagation due to failure of adhesive resulting in decoupling of foam pucks within the braided tube. This increases local stresses, decreases effective crush length, and provides insufficient energy absorption.
2. The dominant failure mode in specimens containing a rectangular foam core is the combination of core and braided tube.
3. Total energy absorption for the tubular system ranged from approximately 4.34 kJ to 10.81 kJ. The majority of energy absorption occurred post lock up.
4. Post processing of high speed video footage validated Cheng's theoretical model during pre-lockup. When comparing Cheng's theoretical predictions versus experimental results of braided tube radius versus length, an error of 1.69% was achieved with a 98% validation metric.
5. Low density rectangular foam cores resulted in a uniform deformation crushing throughout the majority of the braided tube. When comparing the experimental energy versus displacement response of the braided tube obtained within this investigation, a strong agreement to the model developed by Cheng, was noted. A percentage error of 3.03% and a validation metric of 0.97 were noted to occur between the experimental and theoretical findings.

6. High density rectangular foam cores suffered from localized necking where foam fracture occurred and the mismatch between the higher density foam core and braid tube resulted from a deviation to the analytical model from [14]. Thus, for specimens incorporating a high density aluminum foam core the analytical model should not be used in engineering analysis.

8.2 Conclusions for transverse testing of aluminum foam filled braided tubes

A significant amount of information regarding the mechanical response, failure mechanisms, and energy absorption capabilities of empty braided tubes as well as cylindrical and rectangular foam core geometries encased in braided tubes under quasi-static transverse loading conditions has been achieved through the experimental tests conducted in this research. Digital images were used to examine the local deformation field providing tow kinematics and mechanisms of failure during the event. Furthermore, the use of the long stroke testing machine proved to be beneficial in obtaining knowledge in overall system behaviour. The main findings are presented below.

1. Tube specimens containing low density circular foam cores were observed to fail in the vicinity of the annular clamps. The failures observed in the clamped regions are believed to be attributed to a large degree of tow scissoring and elongation within the region which lead to early progressive failure of the tows. It should be noted that failure occurred at either the left or right side clamp. Tube specimens utilizing high density circular foam cores were observed to fail at the mid-span of the assembly. It is hypothesized that due to the limited amount of foam crushing observed in high density foam tests away from the centre loading bar, highly localized foam crush and fracture at the mid-span, the large degree of tow scissoring, stack up, and bending, also occur at the mid-span near the centre loading bar, resulted in a progressive failure of the braid tows.
2. The average TEA for specimens containing high density circular foam cores and those utilizing a low density circular foam core was determined to be 7.03 kJ and 5.79 kJ, respectively.

3. The average force to crush the interior core and the overall force efficiency of the structures containing high and low density circular foam cores was computed to be 24.14 kN with an F.E of 38.2% and 23.4 kN with an FE of 23.8%, respectively.
4. No significant variation in the SEA was found between specimens encased with high and low density foam cores.
5. The failure mode of specimens containing rectangular foam cores was observed to result from a combination of factors. The fracture of the foam core at the mid-span of the tube resulted in foam crushing and braid tow lockup early in the deformation process. Additionally as the assembly was further deformed, an increasingly larger degree of tow bending was observed at the centre loading bar. Progressive failure of the braid tows was observed at the mid-span of the structure as a result of the combination of tow elongation and bending.
6. The TEA and FE for specimens utilizing high density rectangular foam cores ranged from 7.44 kJ to 9.13 kJ and from 30.5% to 33.6%, respectively.
7. The average force for specimens incorporating low density rectangular foam cores reduced by approximately 55% compared to specimens with high density foam core.
8. The presence of aluminum foam within the braided tube significantly increases the energy dissipation characteristics of the structure compared to an empty braided tube. Increases in the energy absorption up to approximately 3.6 times those findings from an empty braided tube were observed when utilizing an aluminum foam core.
9. A slight variation in the SEA was noted for both specimens with high and low density foam cores with no significant influence on foam density.
10. During the transverse deformation process both the circular and rectangular foam cores were observed to behave in a unique fashion. Specimens containing circular cores were observed to experience foam puck separation, while specimens containing rectangular cores were noted to experience foam core fracture. The failure mechanisms of the braided structure subsequent to foam core separation

and fracture result in braid tow elongation and tow bending at mid-span which influenced the structure's strength and maximum energy absorption capacity.

RECOMMENDATIONS FOR FUTURE WORK

The following recommendations represent areas of future research opportunities to further develop aluminum foam filled braided tubes.

1. Conduct dynamic loading tests in the transverse orientation for empty and foam filled braided tubes. It would be essential to understand the mechanical performance and energy response under high speed impact conditions. In addition, examine any rate dependent phenomena occurring during testing such as frictional effects between scissoring tows and dependence of foam core density.

2. Research and experiment the types of joining methods for braided tubes. It would be essential for future work and for applicable use in the industry to understand how to join (e.g. welding, adhesives, etc.) stainless steel braided tubes to other materials such as steel alloys, aluminum, any other composites. Future research should consider the stresses that could possibly be generated at the edge of the specimen if proper boundary conditions are not applied. Thus, the global stress-strain measurements will provide low strength and stiffness values because of edge effects if proper boundary conditions are not applied.

REFERENCES

[1]. Utilities and energy management department. Walking and working surfaces program. University of Texas at Austin, 2007.

[2]. Bureau of Labor Statistics. Employed persons by detailed industry, sex, race, and Hispanic or Latino ethnicity, 2012 (Household Data Annual Average, Table 18), 2012. Accessed on September, 2013. http://www.bls.gov/cps/cpsaat18.pdf

[3]. Bureau of Labor Statistics. Workplace injury and illness in 2011. Accessed on September, 2013. http://www.bls.gov/news.release/osh.nr0.htm.

[4]. Smartrisk. The Economic Burden of Injury in Canada. Toronto, ON, 2009.

[5]. Goh Y M and Love P E D. Adequacy of personal fall arrest energy absorbers in relation to heavy workers. Safety and Science 2010; 48: 747-754.

[6]. Ilcewicz L. Past experiences and future trends for composite aircraft structure. CS & TA, Composites – Federal Aviation Administration, 2009.

[7]. Ecomagination. General Electric annual report, 2009.

[8]. U.S. Department of Defense. Casualty Summary by Reason. DOD Personnel and Military Casualty Statistics, Center, Defense Manpower Data.

[9]. iCasualties.org. Operation Enduring Freedom, Fatalities by Nationality, 2009.

[10]. WHO. World report on road traffic injury prevention - summary. Geneva: World Health Organization, 2004.

[11]. Murray C J and Lopez A D. The Global Burden of Disease: a comprehensive assessment of mortality and disability from diseases, injuries and risk factors in 1990 and projected to 2020. Cambridge, MA, Harvard School of Public Health, (Global Burden of Disease and Injury Series, volulme I), 1996.

[12]. Whitcomb J D and Kelkar A D. Modeling and performance evaluation of braided composites," FAA annual report of Grant No. DTFA03-01-C00033, 2002.

[13]. A&P Technology Inc. "Frequently asked questions," available at http://www.braider.com [accessed in June 2013].

[14]. Basavaraju D. Design and analysis of a composite beam for side impact protection of a sedan, Master of Science Thesis, Wichita State University, 2005.

[15]. Altenhof W, Powell C, Harte A M, Gaspar R. An experimental investigation into the energy absorption and force/displacement characteristics of aluminum foam filled braided stainless steel tubes under quasi-static tensile loading conditions. International Journal of Crashworthiness, 2005;10:1:21-31.

[16]. Cheng Q, Altenhof W, Jin S Y, Powell C, Harte A M. Energy absorption of aluminum foam filled braided stainless steel tubes under quasi-static tensile loading conditions. International Journal of Mechanical Sciences, 2006;48:1223-1233.

[17]. Cox B and Davis J. Knitted composites for energy absorption under tensile loading, Composites Part A: applied science and manufacturing, 2001; 32:91–105.

[18]. Muralidhar B A. Tensile and compressive behaviour of multilayer flax-rib knitted preform reinforced epoxy composites. Materials and Design, 2013; 49:400-405.

[19]. Goyal D. Analysis of 2x2 braided composites, Master of Science Thesis, Texas A&M University, 2003.

[20]. Harte A M, Fleck N, and Ashby M. Energy absorption of foam-filled circular tubes with braided composite walls. European Journal of Mechanics–A/Solids, 2000;19:31–50.

[21]. Harte A M, Fleck N. On the mechanics of braided tubes in tension. European Journal of Mechanics–A/Solids, 2000;19:259–275.

[22]. Harte A M, Fleck N, and Ashby M. Deformation and failure mechanisms of braided composite tubes in compression and torsion. Acta Materialia, 2000; 48:6:1259-1271.

[23]. Rawal A, Saraswat H, and Kumar R. Tensile response of tubular braids with an elastic core, Composites Part A, 2013; 47:150-155.

[24]. Hopper R H and Grant J W. Mechanics of a hybrid circular braid with an elastic core, Textile Research Journal, 1995; 65:12:709–22.

[25]. Abbott G M. Force-extension behavior of helically wrapped elastic core yarns, Textile Research Institute, 1984; 54:3:204–23.

[26]. Schutze R. Lightweight carbon fibre rods and truss structures, Materials and Design, 1997;18:4/6:231-238.

[27]. Borvik T, Hopperstad O S, Reyes A, Langseth M, Solomos G, and Dyngeland T. Empty and foam filled circular aluminum tubes subjected to axial and oblique quasi static loading. International Journal of Crashworthiness, 2003; 8:5:481-494.

[28]. Saggar P. Experimental study of laminated composite tubes under bending. Master of Science Thesis, The University of Texas, Arlington, 2007.

[29]. Nageswara R J , Wu Z, Chang F K, and Goldberg R K. Lateral crashing of tri-axially braided composite tubes, Earth and Science, 2008.

[30]. Littell J D, Binienda W K, Roberts G D, Goldberg R K. Characterization of damage in triaxial braid composites under tensile loading. NASA Center for Aerospace Information, 2009; NASA/TM-2009-215645.

[31]. Gan C, Gibson R F, and Newaz G M. Analytical/experimental investigation of energy absorption in grid-stiffened composite structures under transverse loading. Society for Experimental Mechanics, 2004, 44:2:185-194.

[32]. Li X T, Binienda W K, and Littell J D. Methodology for impact modeling of triaxial braided composites using shell elements. Journal of Aerospace Engineering 2009; 22: 310–317.

[33]. Littell J D, Binienda W K, and Arnold W A. Effect of microscopic damage events on static and ballistic impact strength of triaxial braid composites. Composites A, 2009; 40: 1846–1862.

[34]. Zhang Y, Sun B, and Gu B. Experimental characterization of transverse impact behaviors of four-step 3-D rectangular braided composites, 2012; 46(24):3017-3029.

[35]. Tonkovich A, Li Z, DiCecco S, Altenhof W, Banting R, and Hu Hand. Experimental observations of tyre deformation characteristics on heavy mining vehicles under static and quasi-static loading. Journal of Terramechanics, 2012; 49:215–231.

[36]. Ashby M, Evans A, Fleck N, Gibson L, Hutchinson J W, and Wadley H N G. Metal Foams – A Design Guide, Butterworth-Heinemann, 2000;8-9.

[37]. Harte A M and Altenhof W. Uses for Stabilized Aluminum Foam in Crashworthiness and Strengthening Applications, SAE paper no. 2003-01-1295, Society of Automotive Engineers, 2003.

[38]. Degischer H P. Innovative light metals: metal matrix composites and foamed aluminium, Materials and Design, 1997;18:4/6:221-226.

[39]. Xia X, Feng H, Zhang X, and Zhao W. The compressive properties of closed-cell aluminum foams with different Mn additions, Materials and Design, 2013; 51:797-802.

[40]. Cymat Technologies Ltd. Aluminum Foam Technology Applied to Automotive Design, 2002, Mississauga, Ontario, Canada.

[41]. Xcitex Inc. ProAnalyst User Manual, 2004, Cambridge, MA, U.S.A.

[42]. Oberkampf W, Trucano T. Verification and validation in computational fluid dynamics. Prog Aerospace Sci 2002; 38:209–72.

APPENDIX A: ENGINEERING PRINTS

A1 Engineering prints for individual members of the testing apparatus

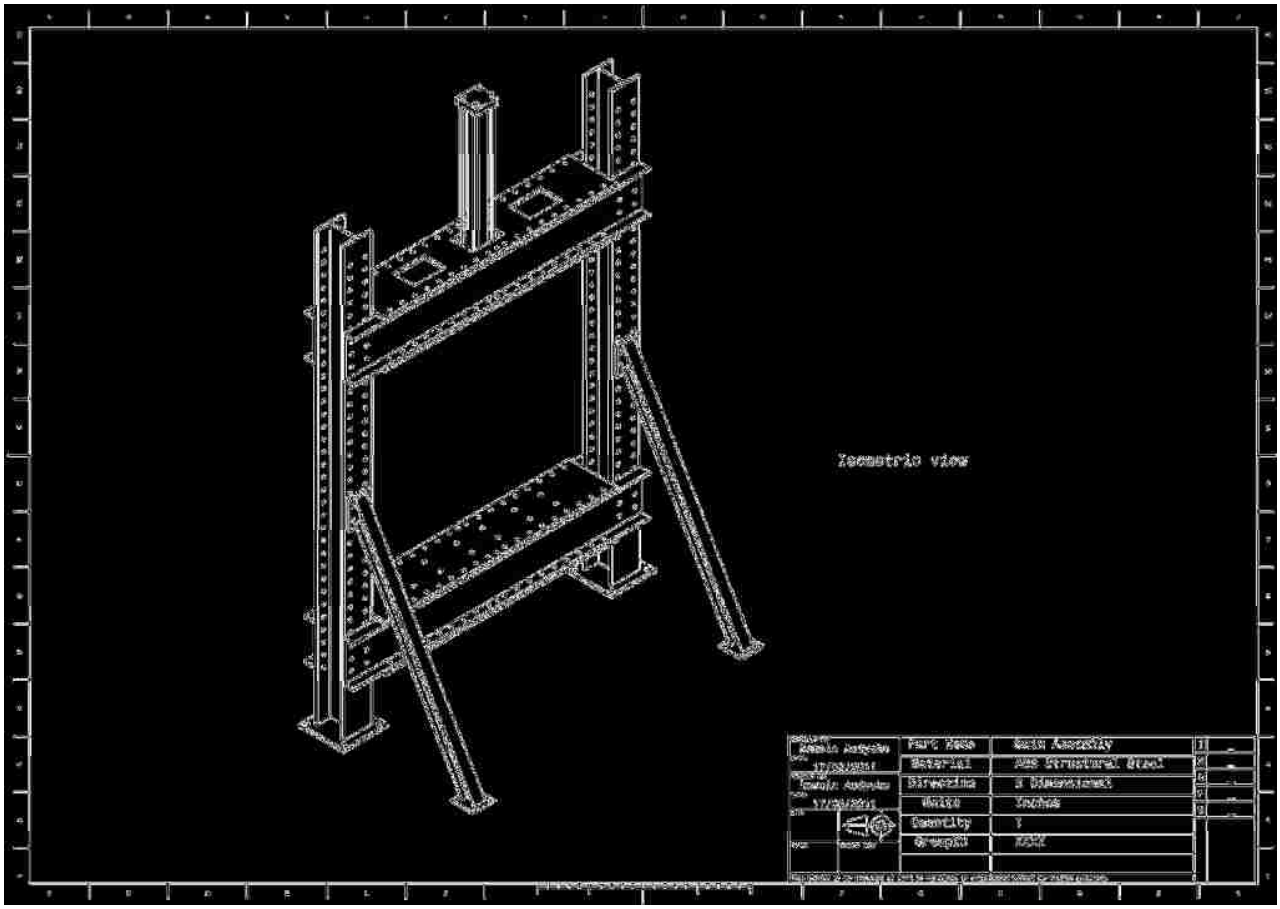

Figure A1.1: Main assembly of the testing apparatus.

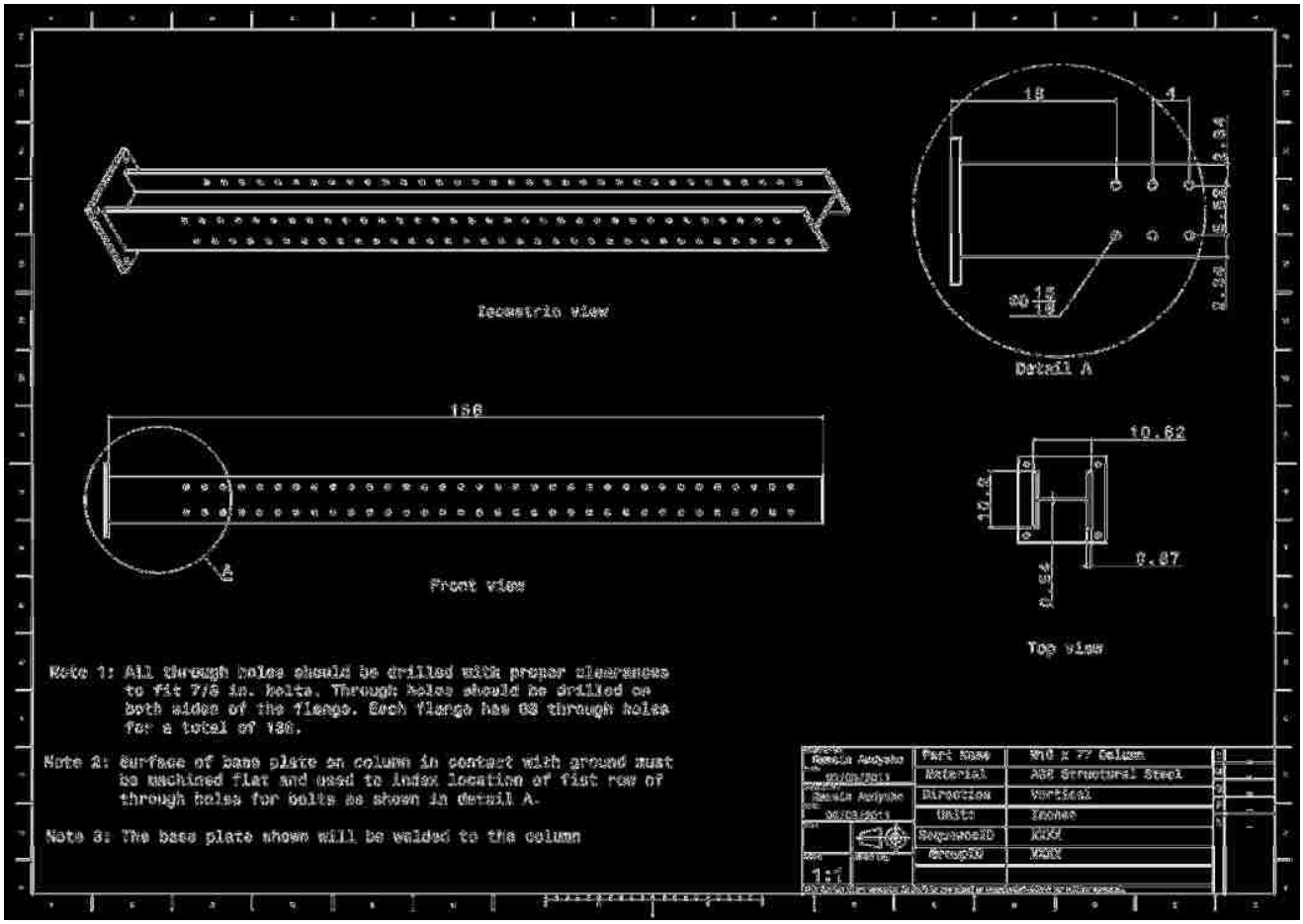

Figure A1.2: W10 x 77 column.

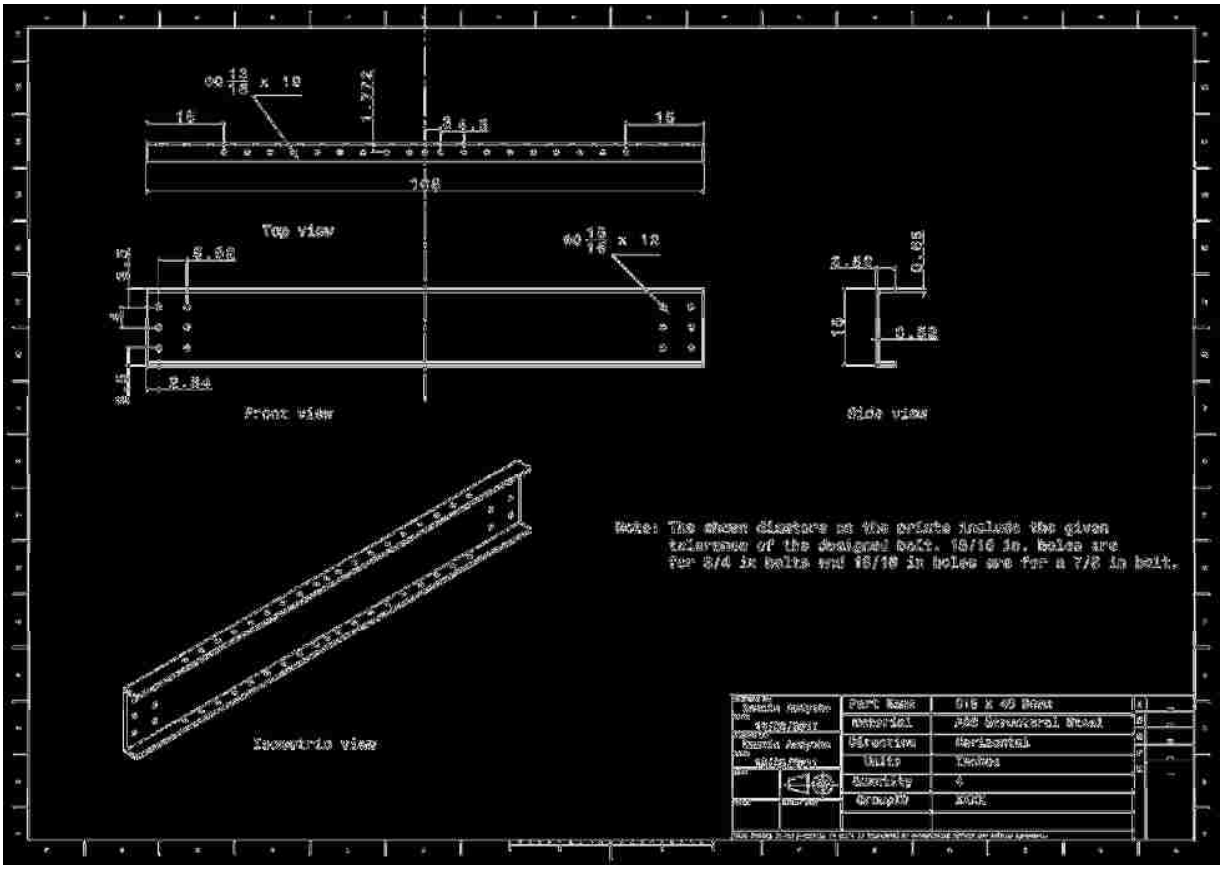

Figure A1.3: C15 x 40 beam.

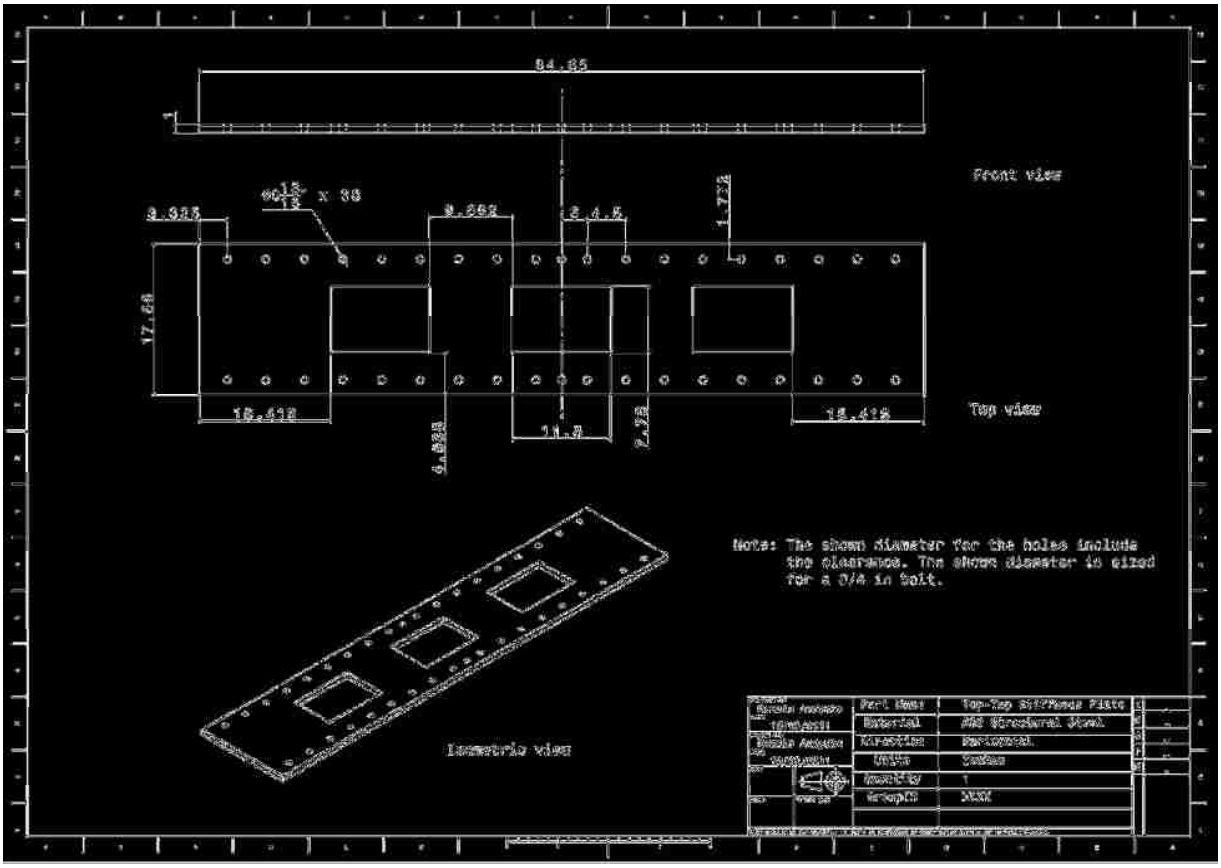

Figure A1.4: Top-top plate stiffeners.

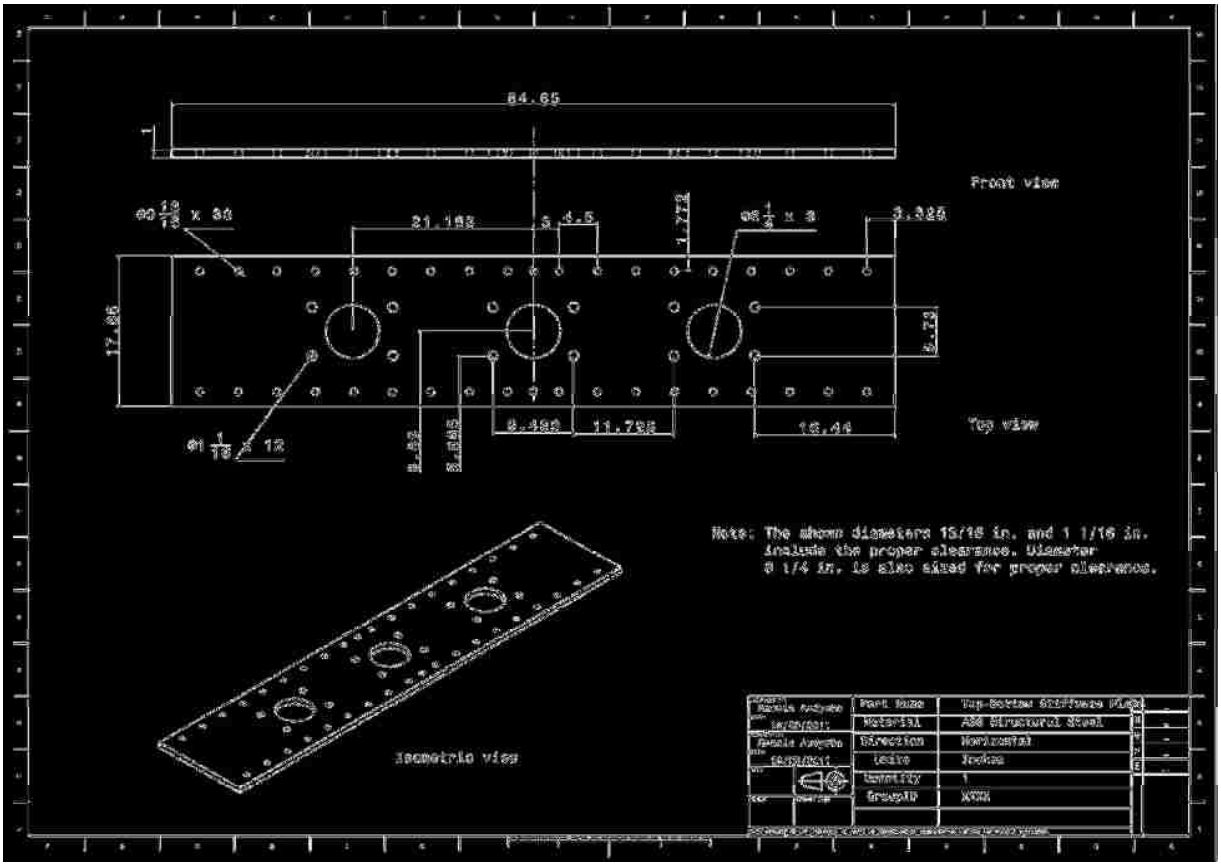

Figure A1.5: Top-bottom plate stiffeners.

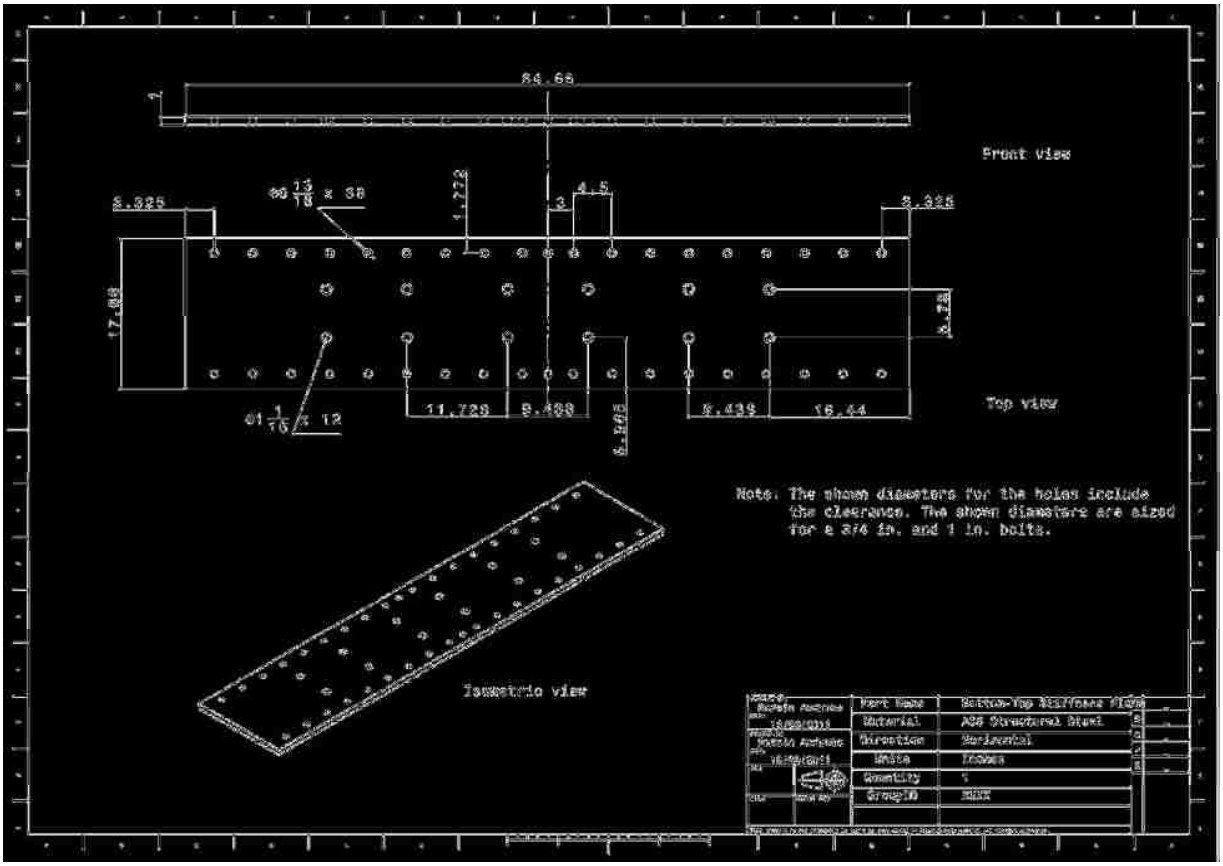

Figure A1.6: Bottom-top plate stiffeners.

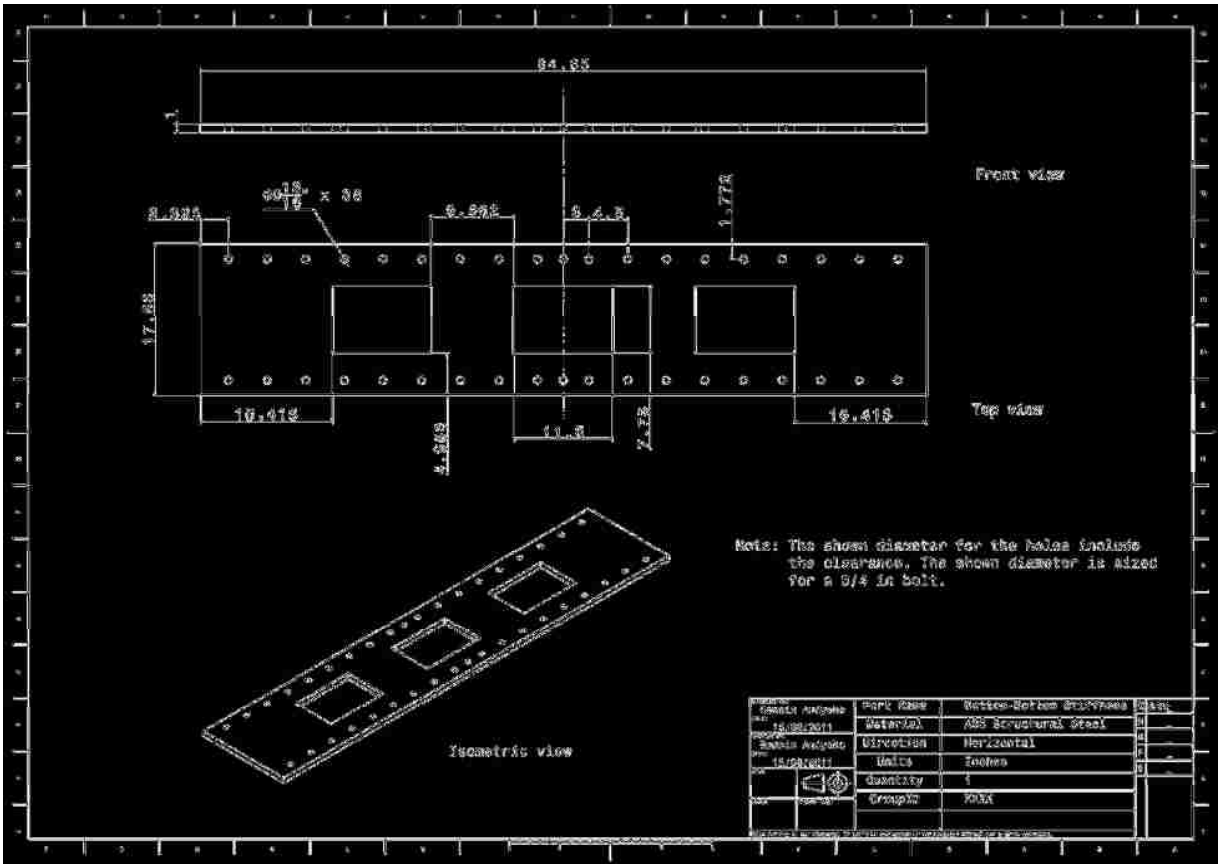

Figure A1.7: Bottom-bottom plate stiffeners.

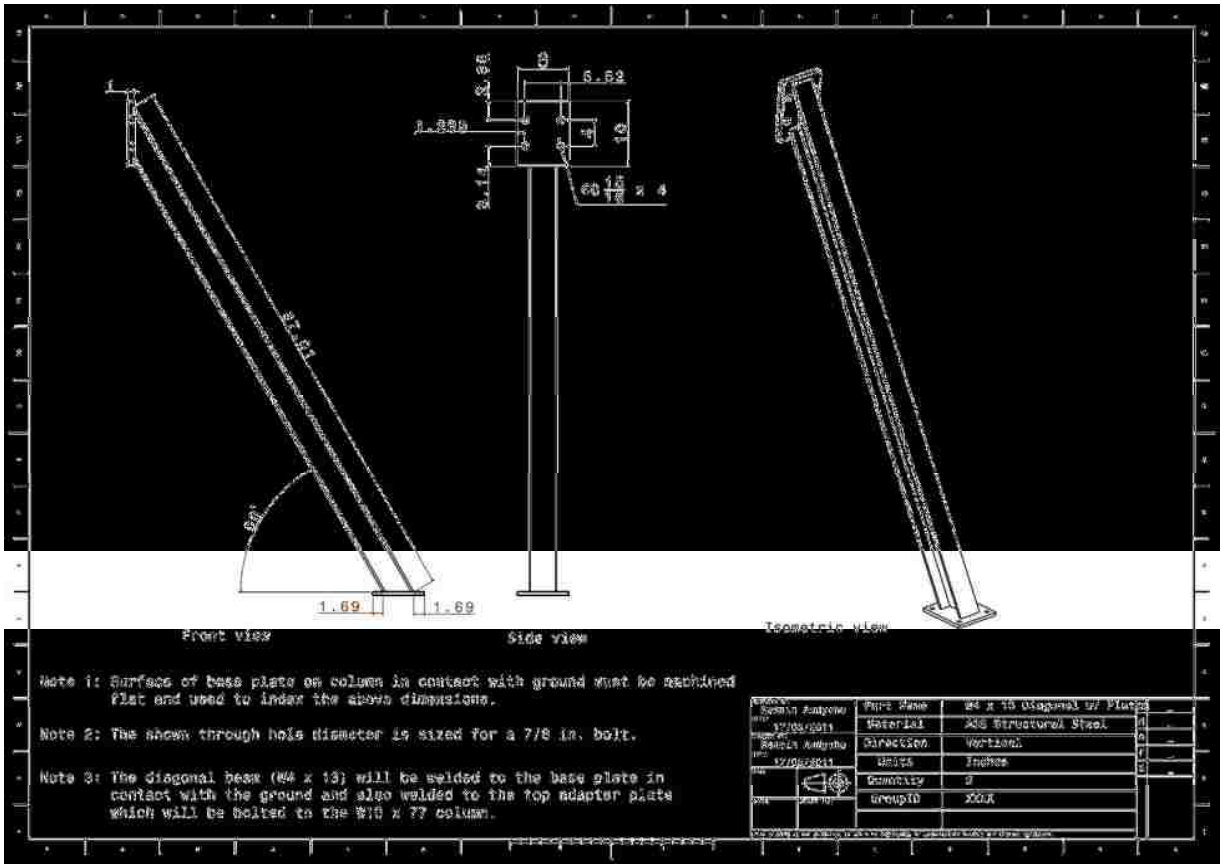

Figure A1.8: W4 x 13 diagonal column with connecting plate.

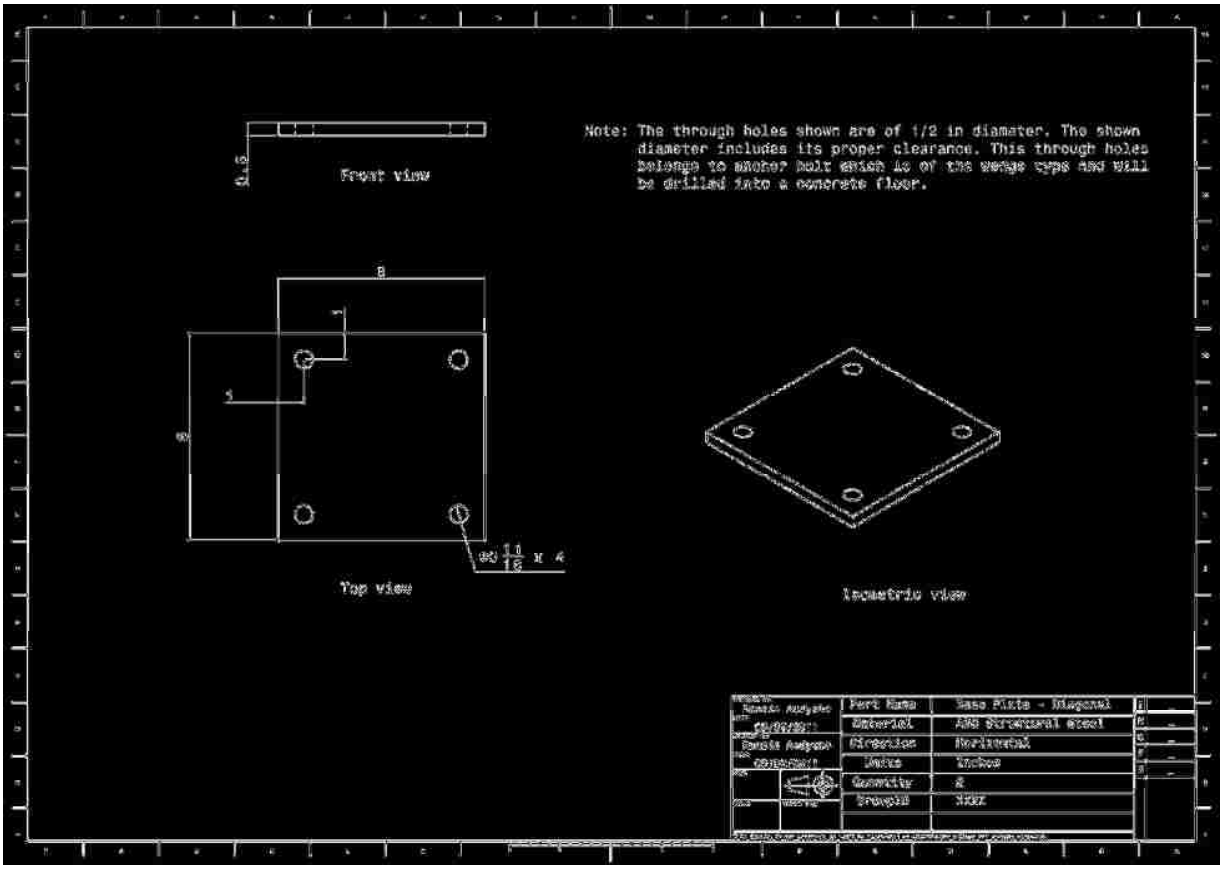

Figure A1.9: Base plate for diagonal W4 x 13 column.

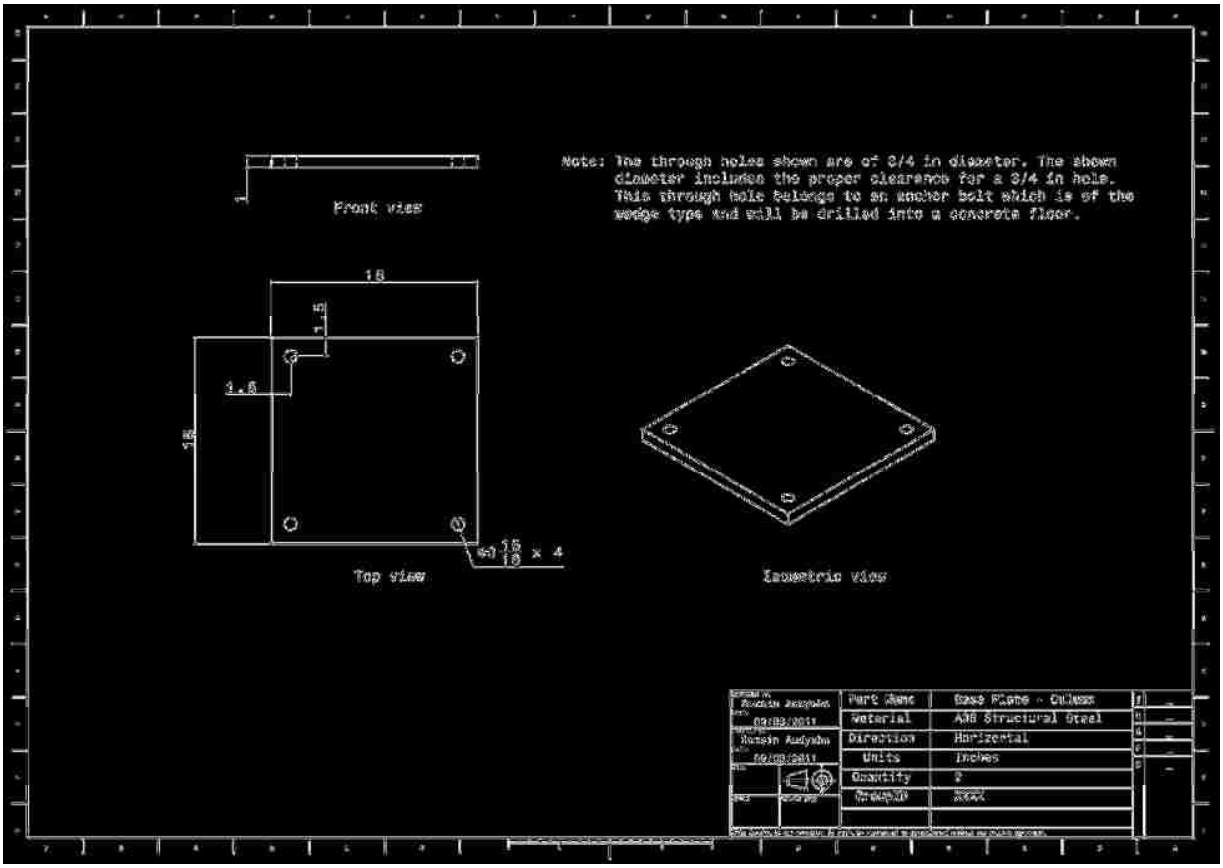

Figure A1.10: Base plate for W10 x 77.

A2 Engineering prints for individual members of the upper axial fixture

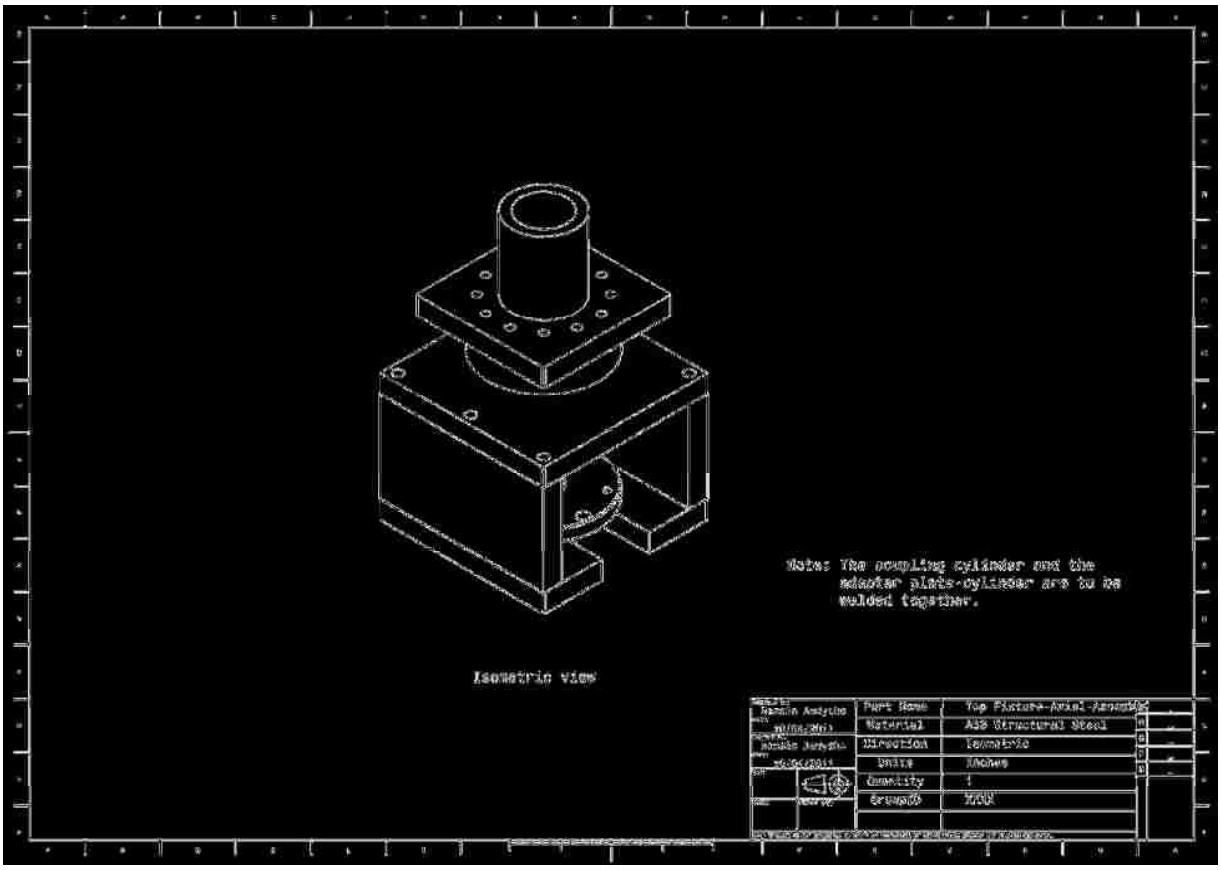

Figure A2.1: Assembly of the top axial fixture.

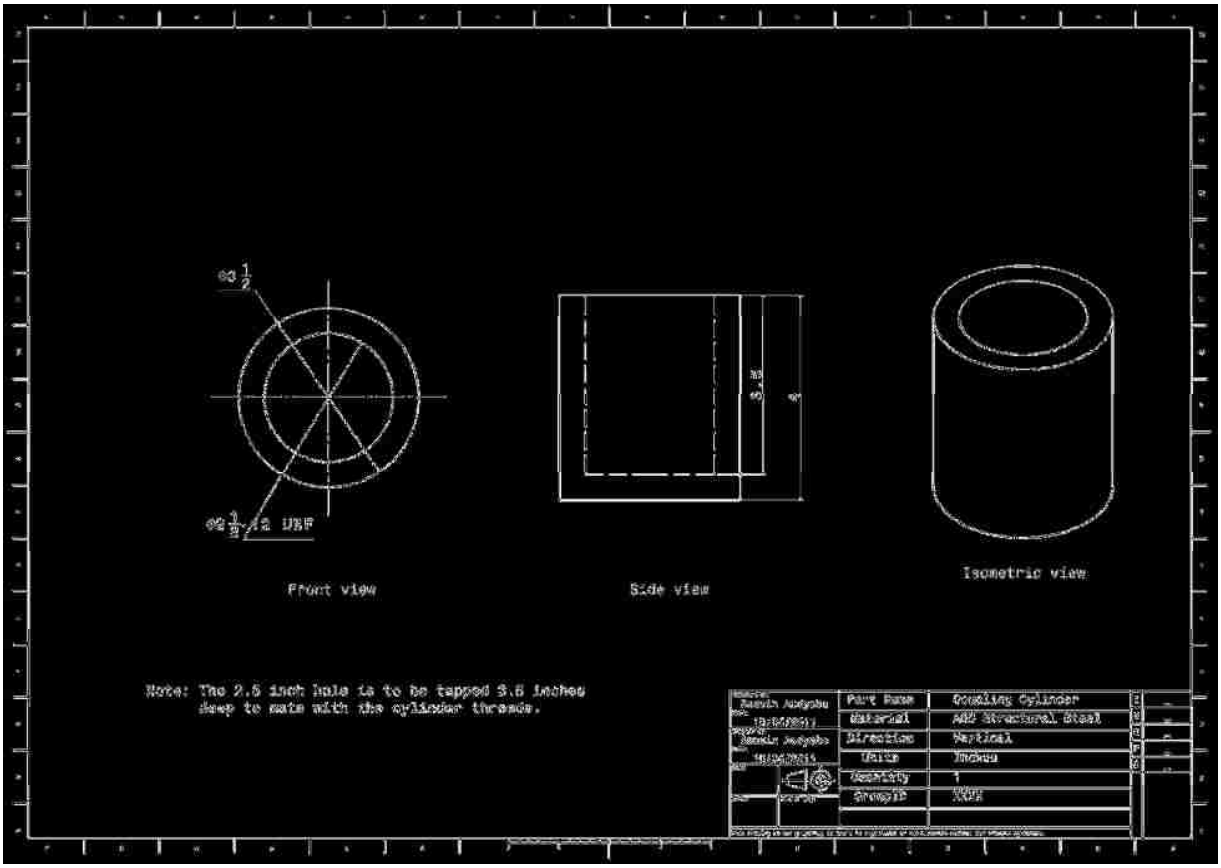

Figure A2.2: Coupling adapter threading into the hydraulic cylinder.

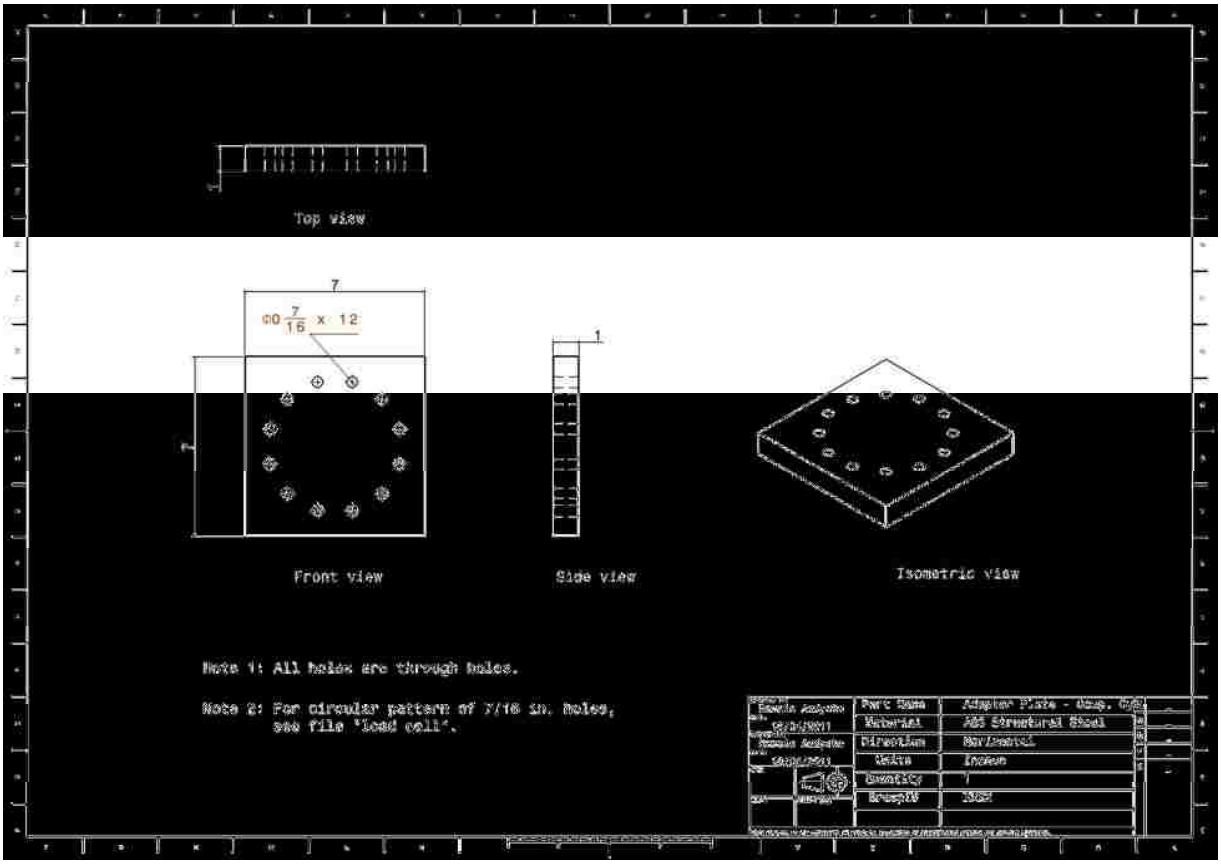

Figure A2.3: Adapter plate welded to coupling cylinder.

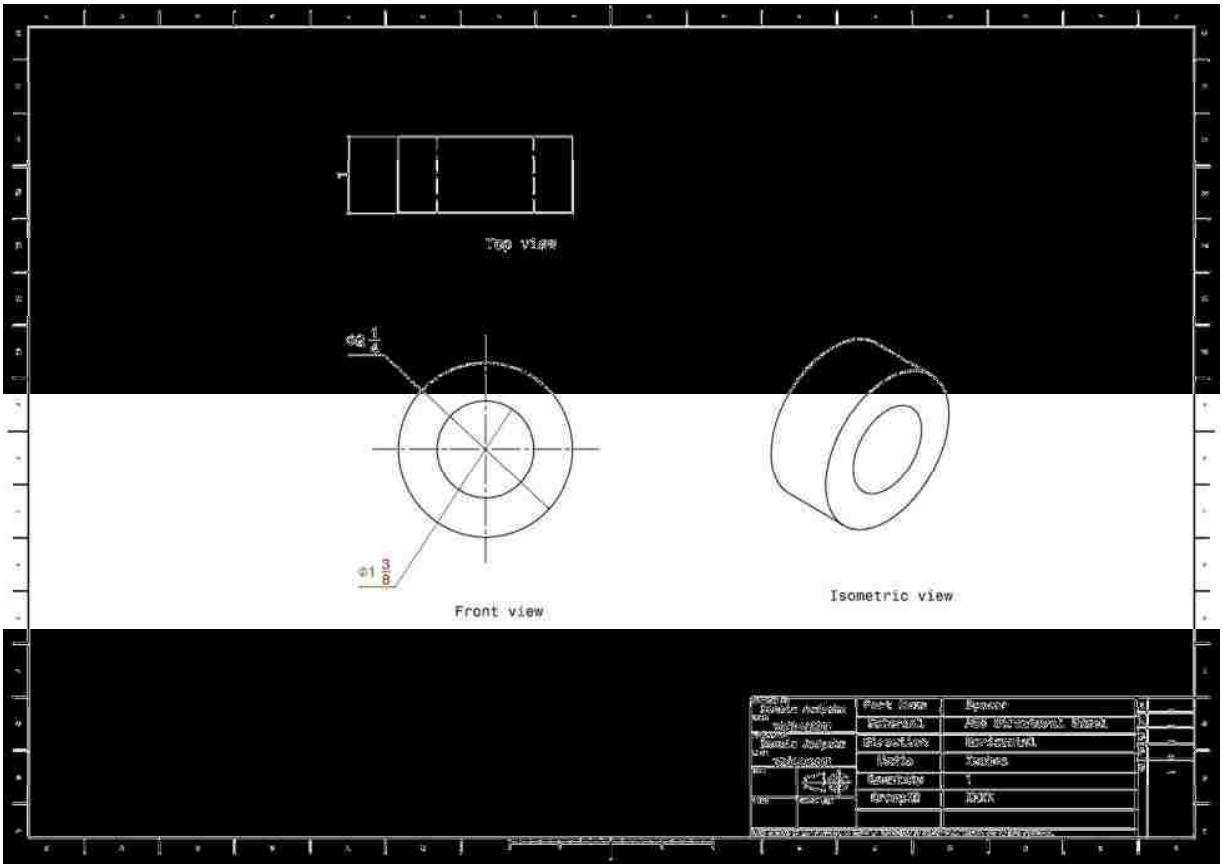

Figure A2.4: Spacer to clear the interference of load cell bolt pattern.

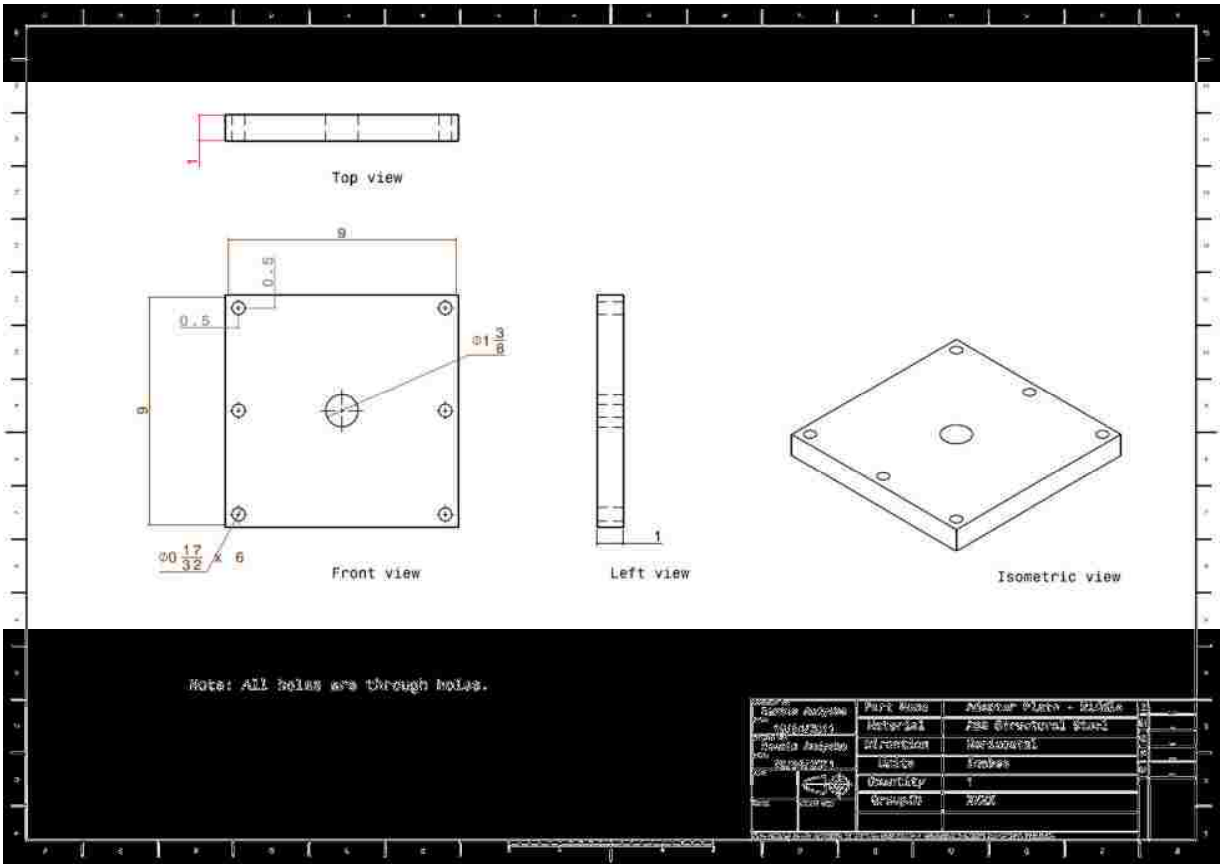

Figure A2.5: Adapter plate - middle.

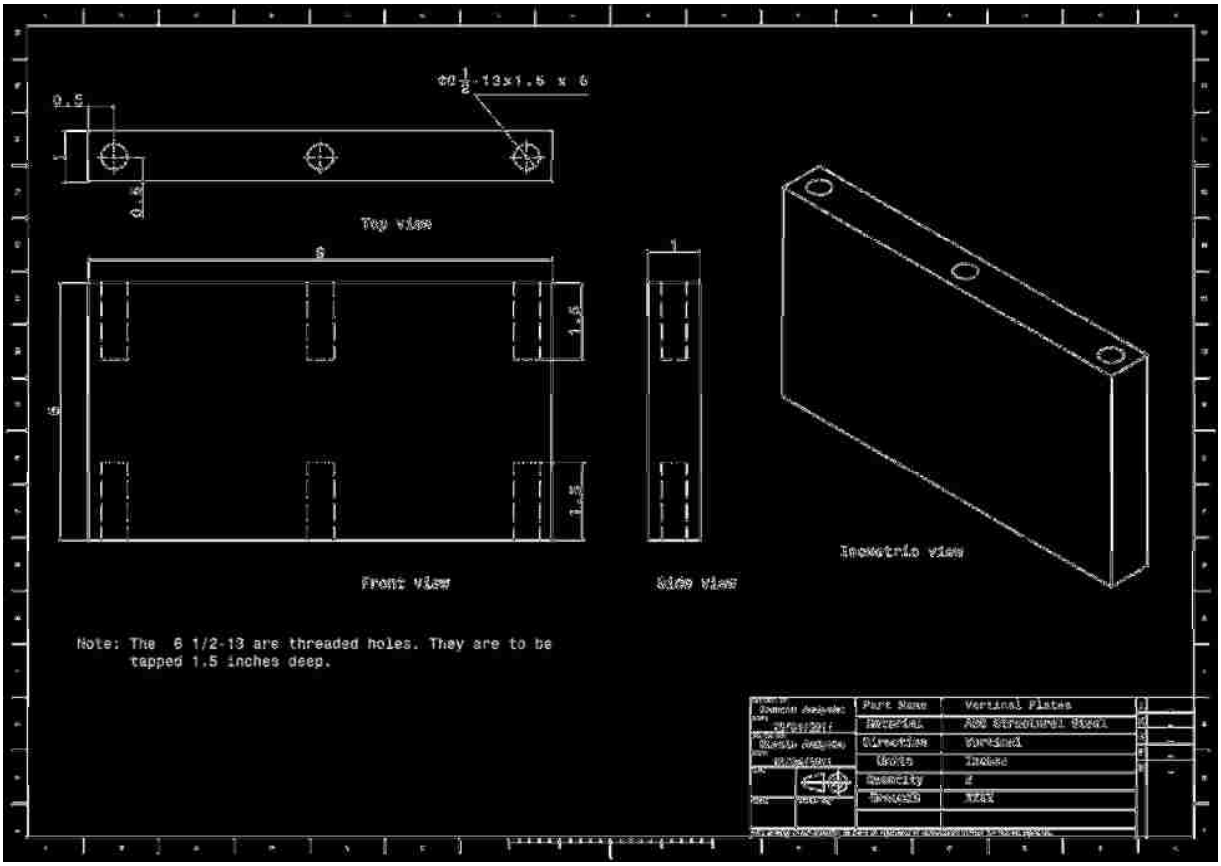

Figure A2.6: Vertical plate.

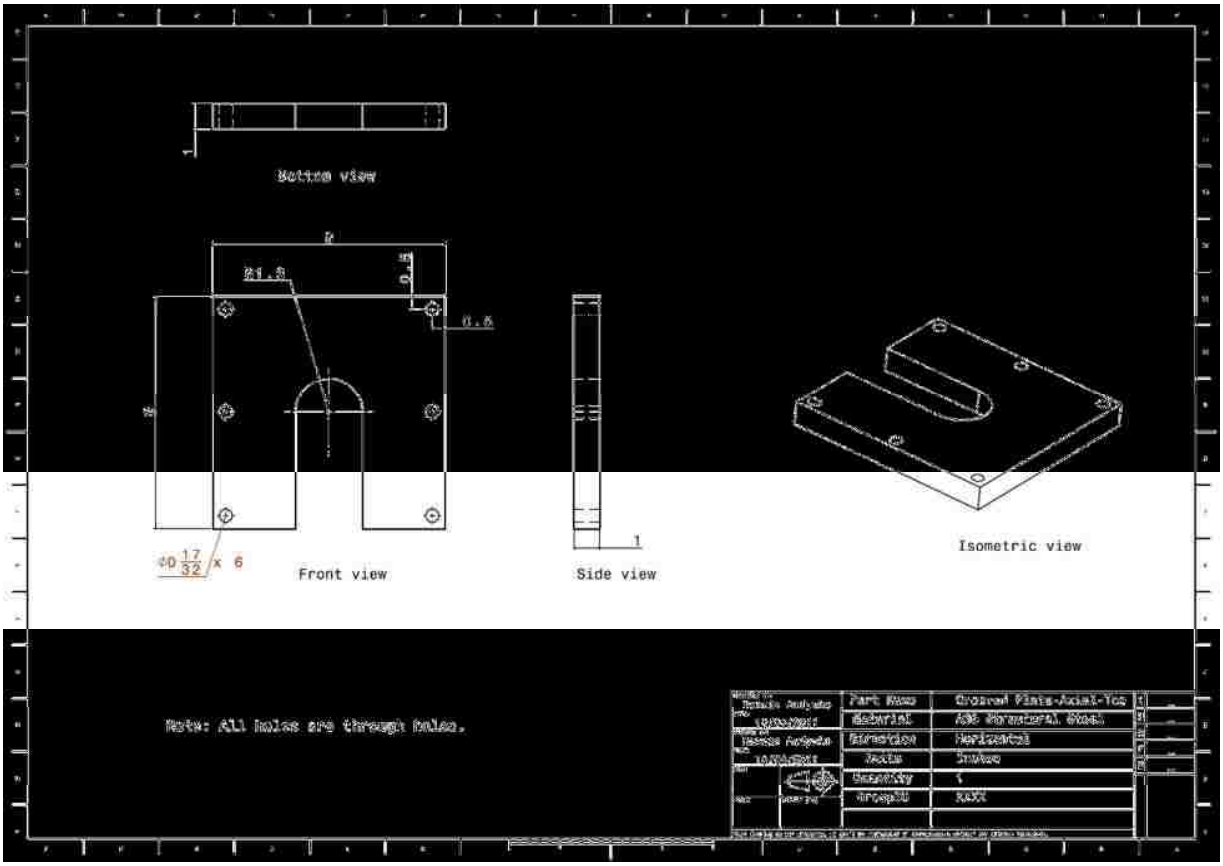

Figure A2.7: Grooved plate – axial top.

A3 Engineering prints for individual members of the lower axial fixture

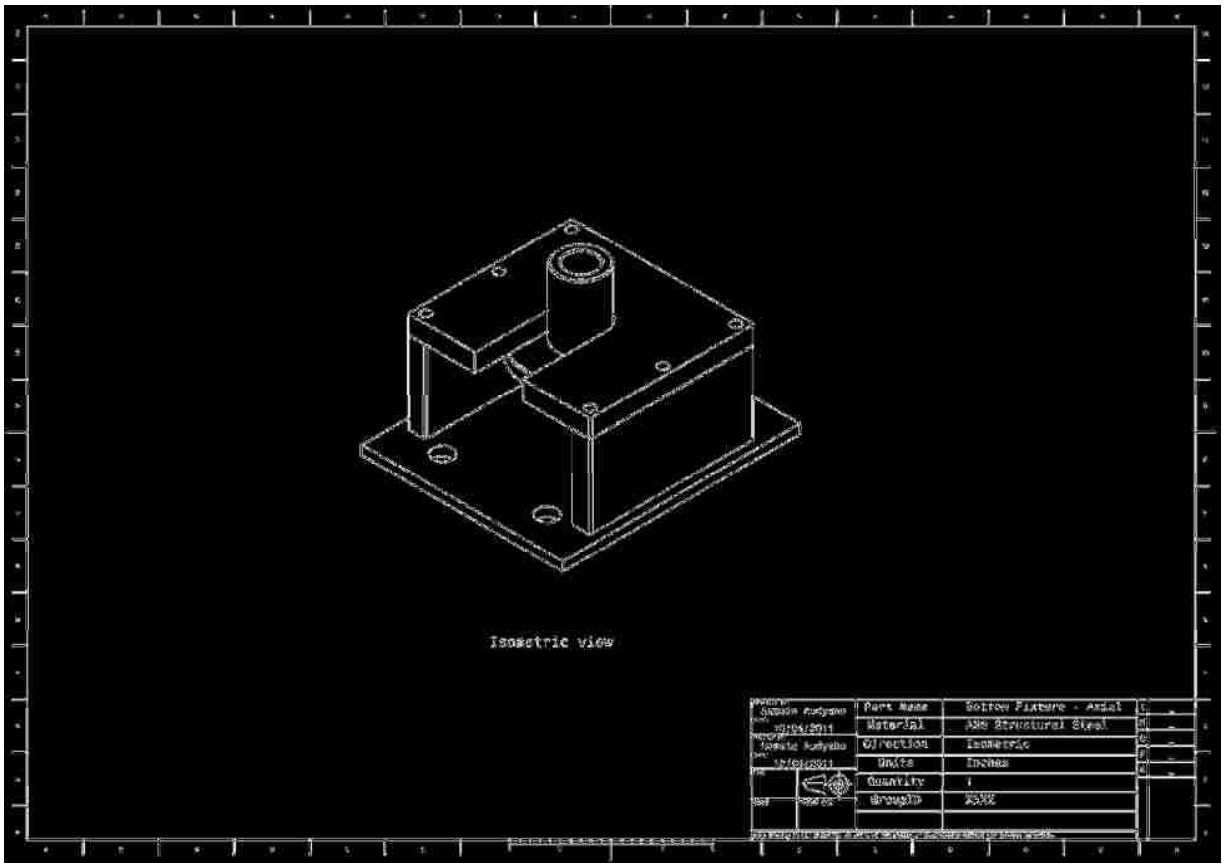

Figure A3.1: Assembly of the lower axial fixture.

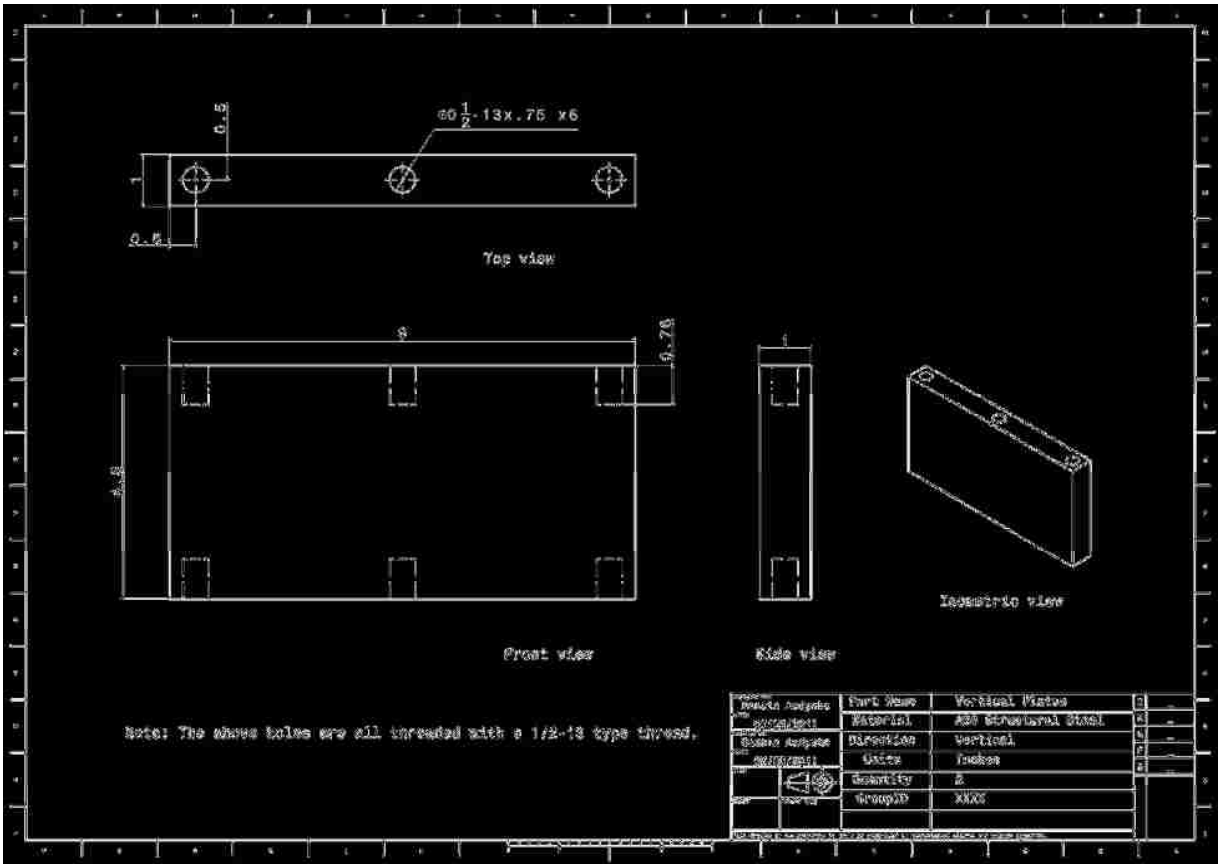

Figure A3.2: Vertical plate for lower axial fixture.

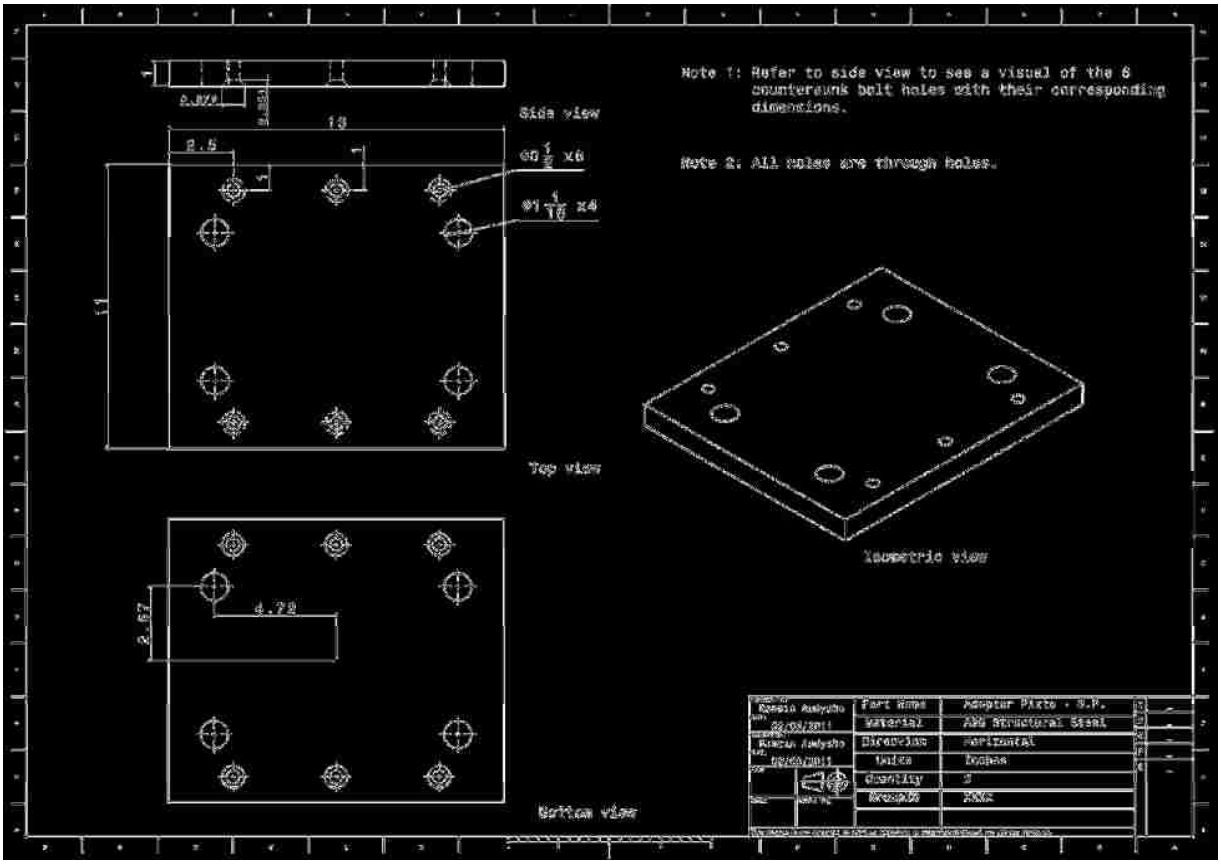

Figure A3.3: Adapter plate for lower axial fixture bolted to bottom-top plate stiffeners.

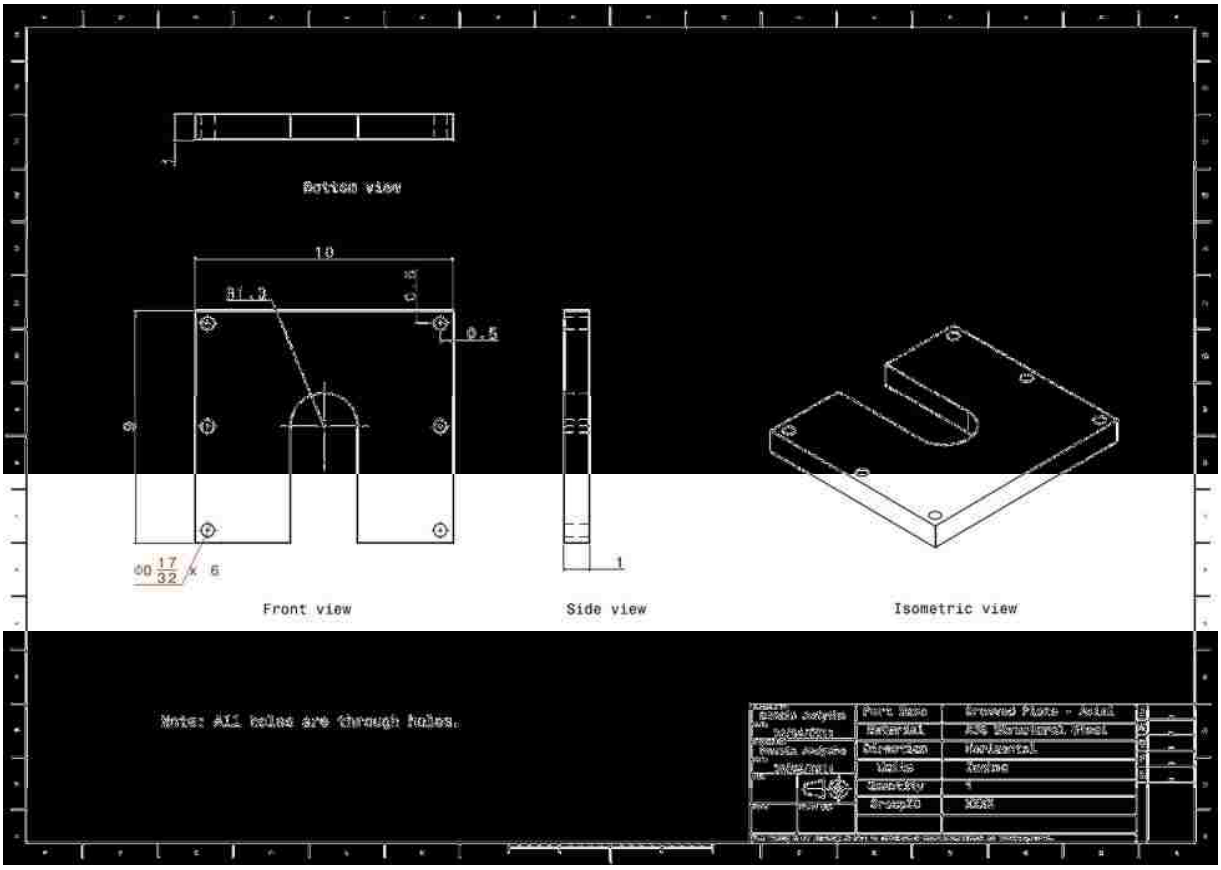

Figure A3.4: Grooved plate for lower axial fixture.

A4 Engineering prints for individual members of the transverse fixture

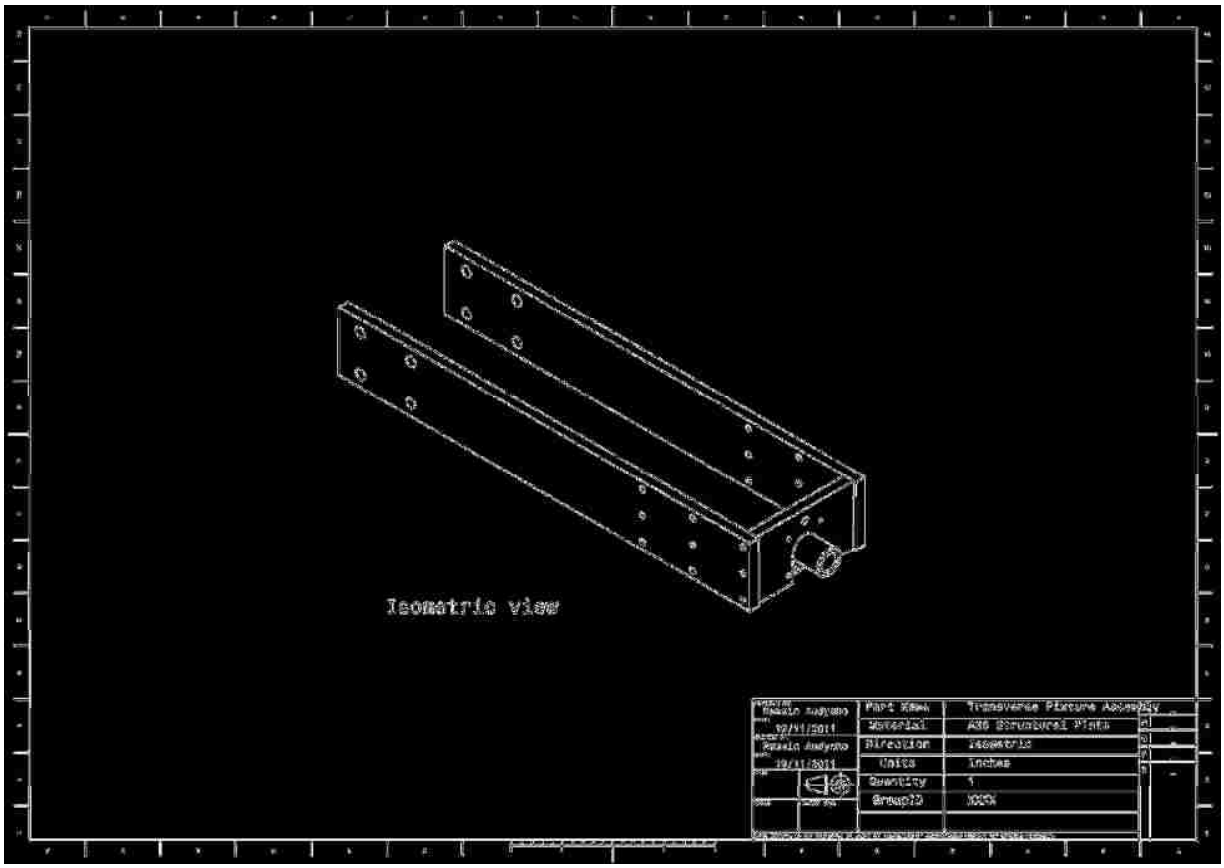

Figure A4.1: Assembly of the transverse fixture.

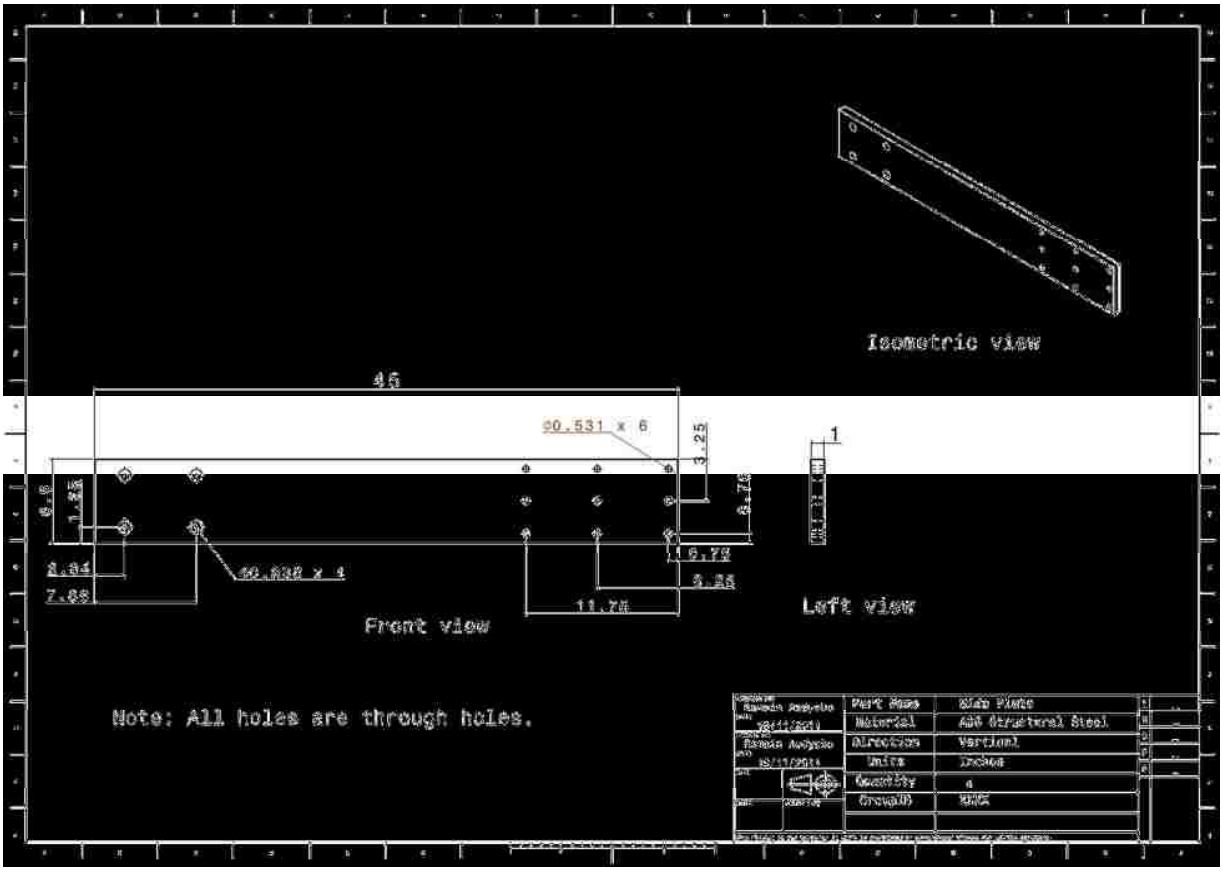

Figure A4.2: Side plates of the transverse fixture.

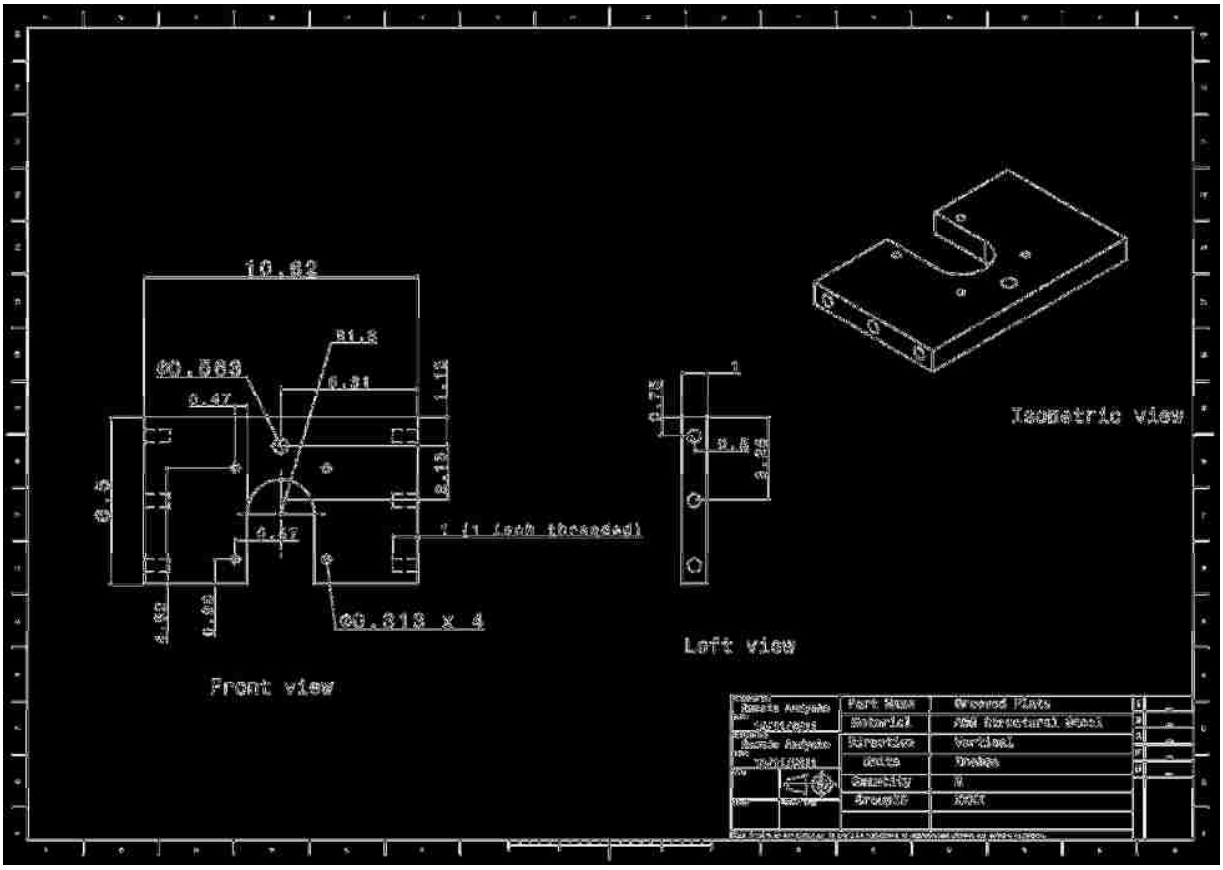

Figure A4.3: Grooved plates for the transverse fixture.

A5 Engineering prints for individual members of the centre fixture

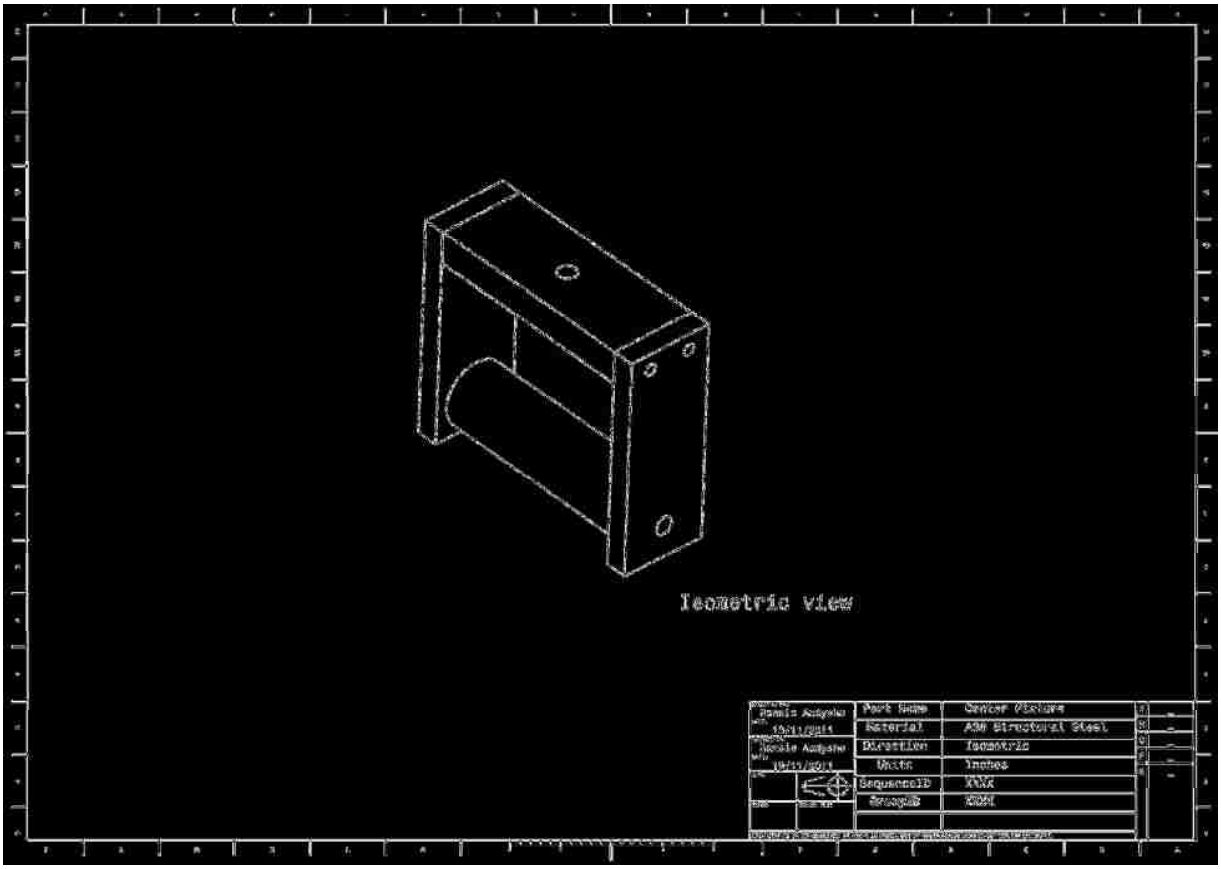

Figure A5.1: Assembly of the centre fixture for transverse testing.

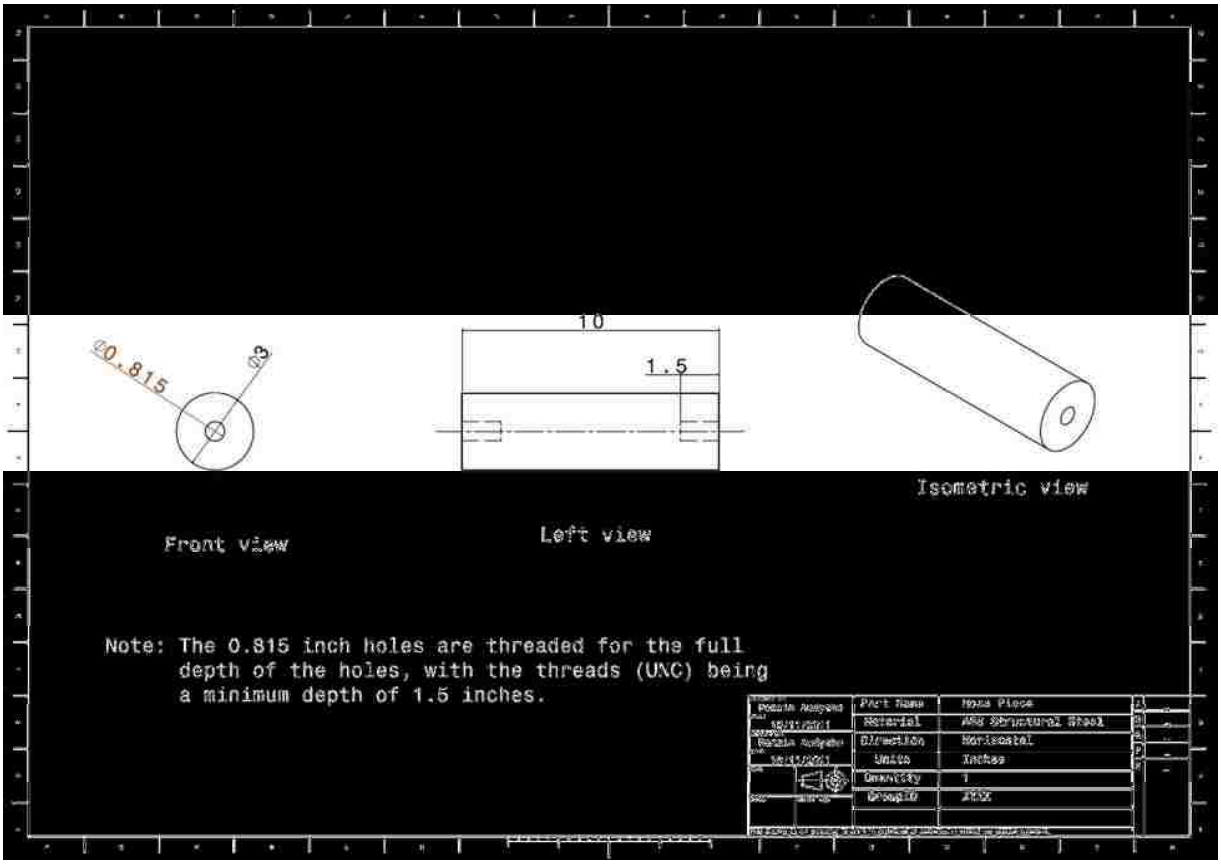

Figure A5.2: Centre loading bar for transverse testing.

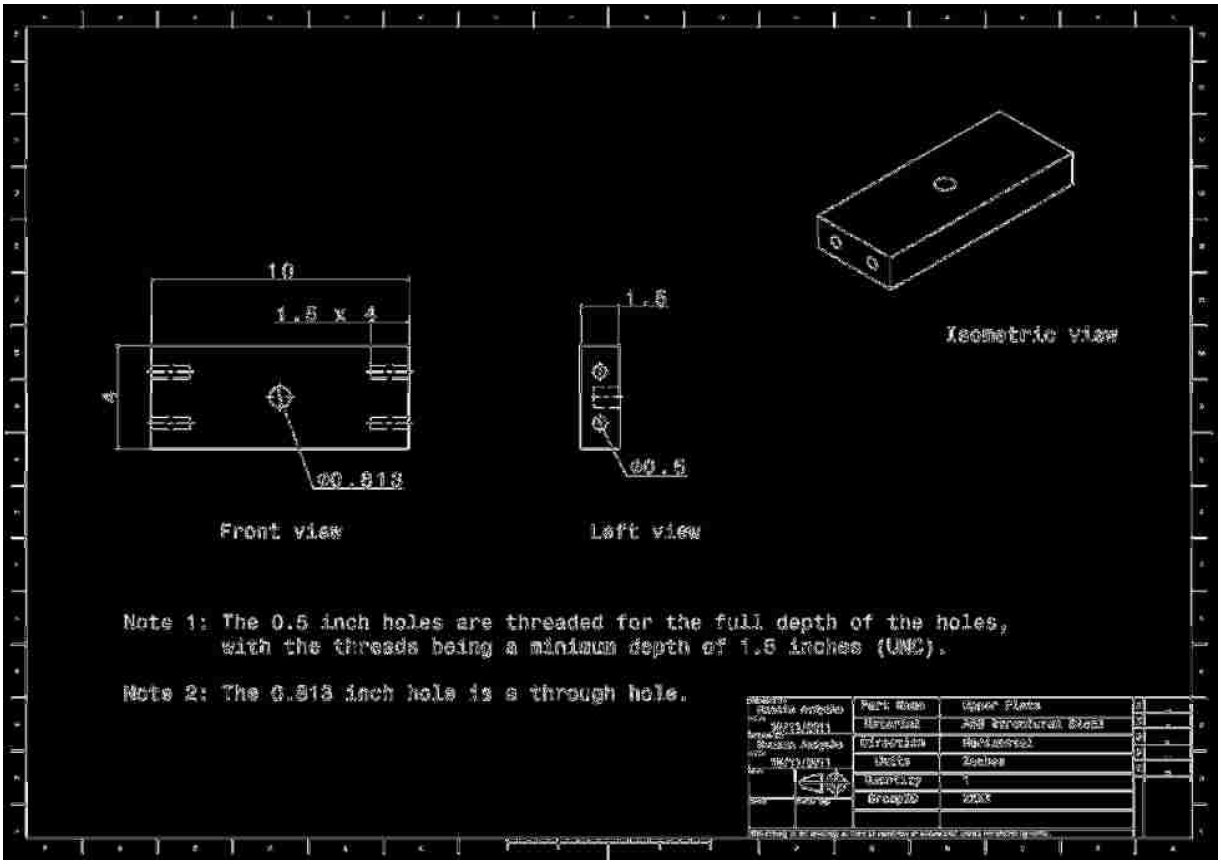

Figure A5.3: Upper plate for the centre fixture.

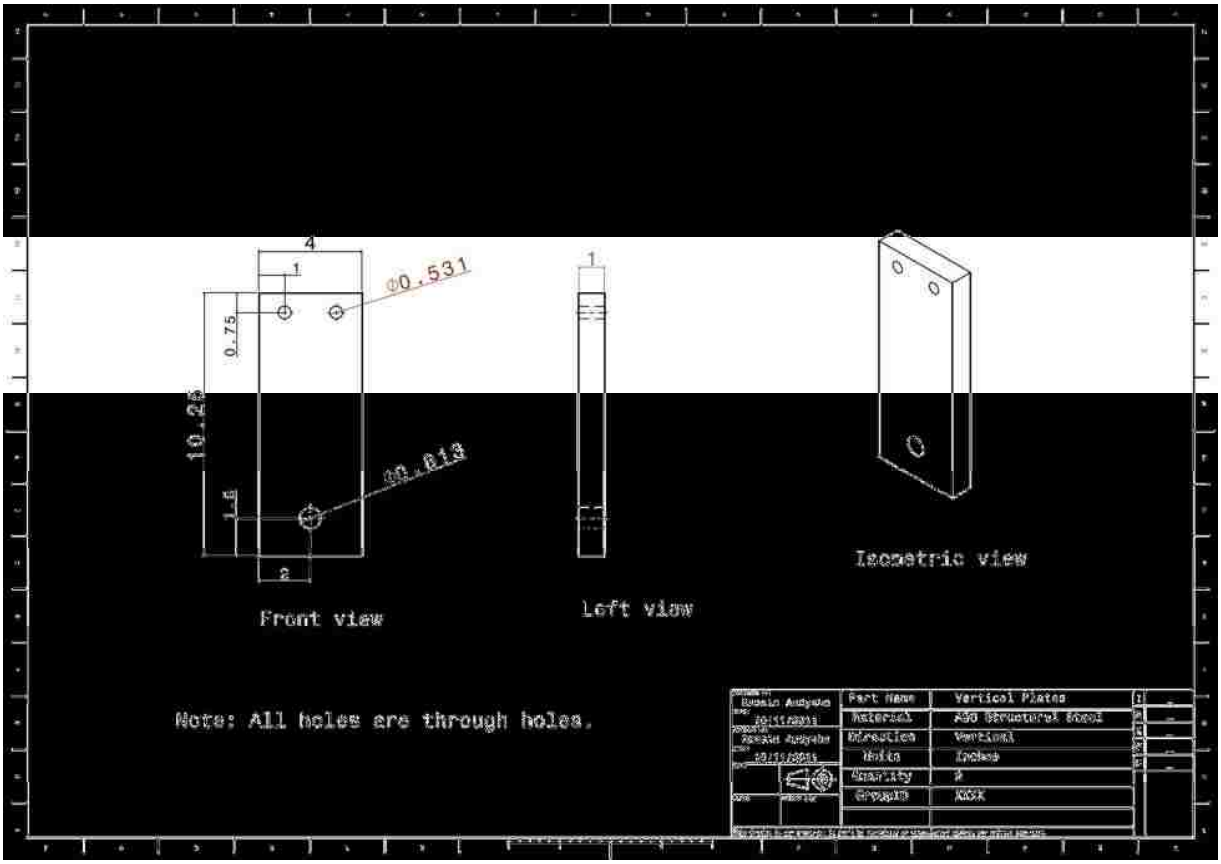

Figure A5.4: Vertical plates for the centre fixture.

APPENDIX B: PRESS CODE

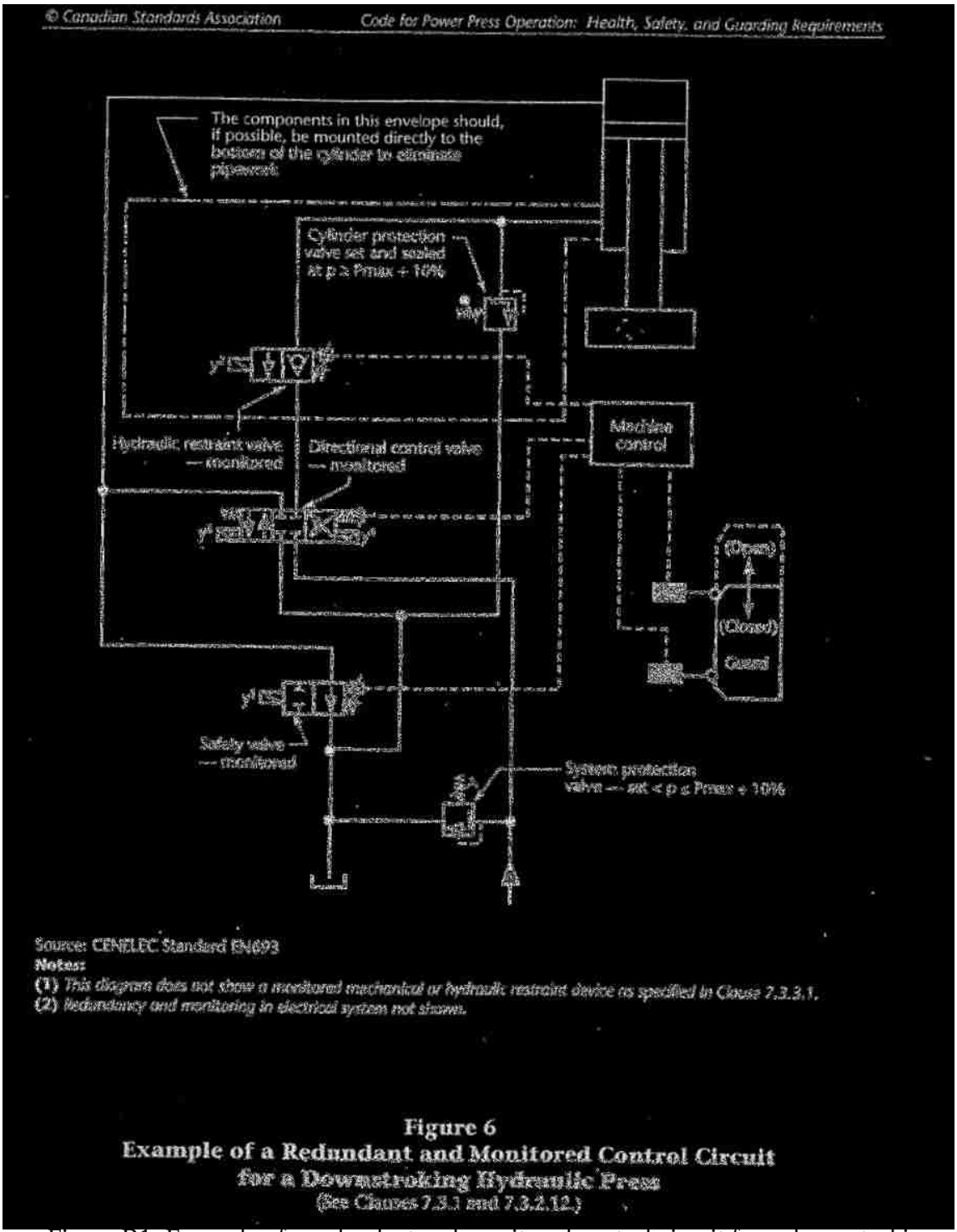

Figure B1: Example of a redundant and monitored control circuit for a down stroking hydraulic circuit.

APPENDIX C: FINITE ELEMENT MODEL RESULTS OF THE TESTING APPARATUS

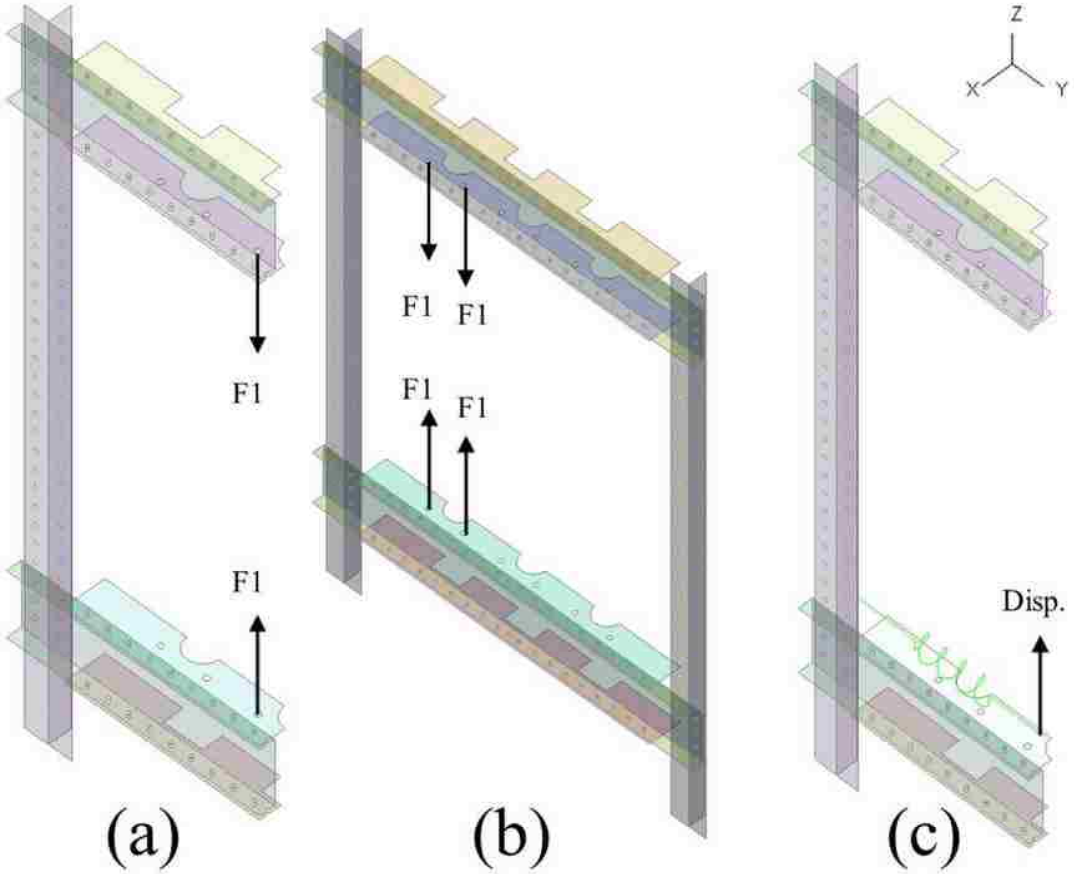

Figure C1: Loading conditions for (a) axial, (b) offset, and (c) transverse configurations. The parameter F1 is the applied load of 87.5 kN. Parameter Disp. denotes the prescribed elongation (approximately 250 mm) of the discrete element.

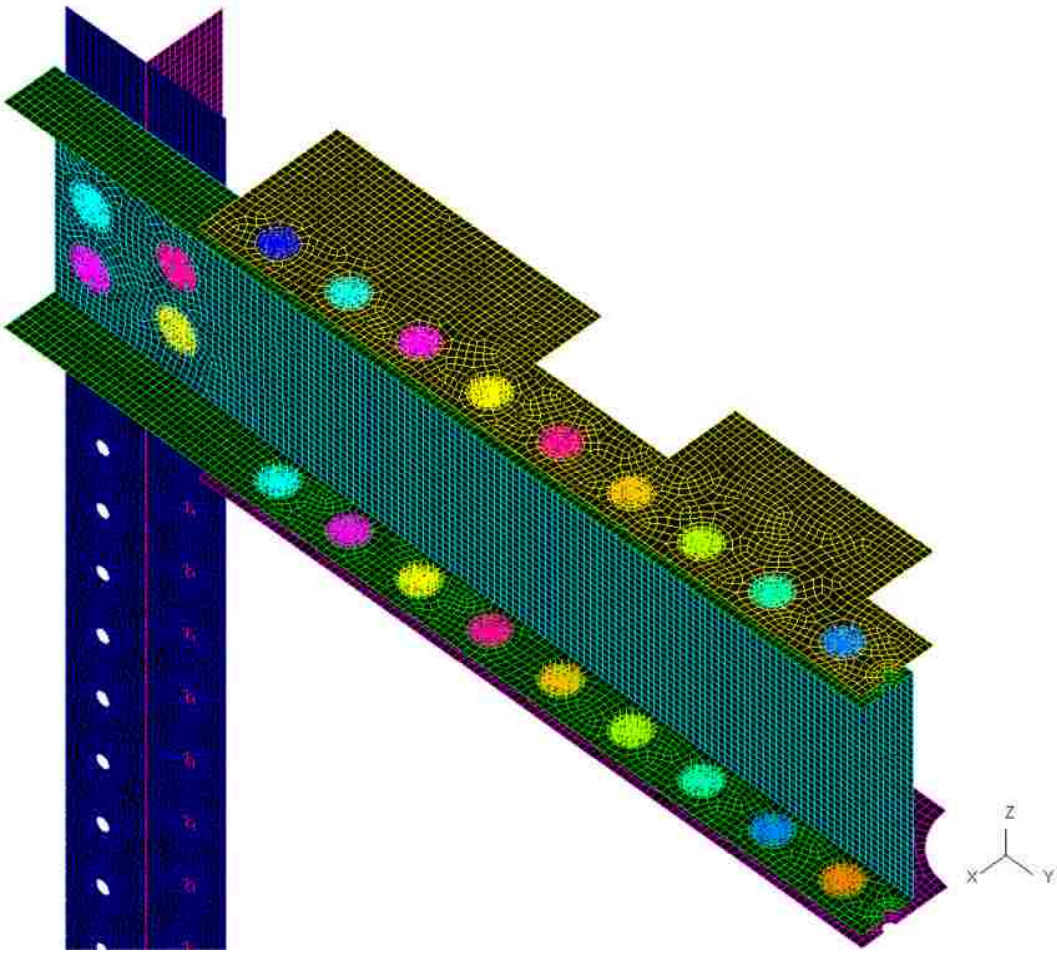

Figure C2: Quarter model illustrating discretization and CNRBs.

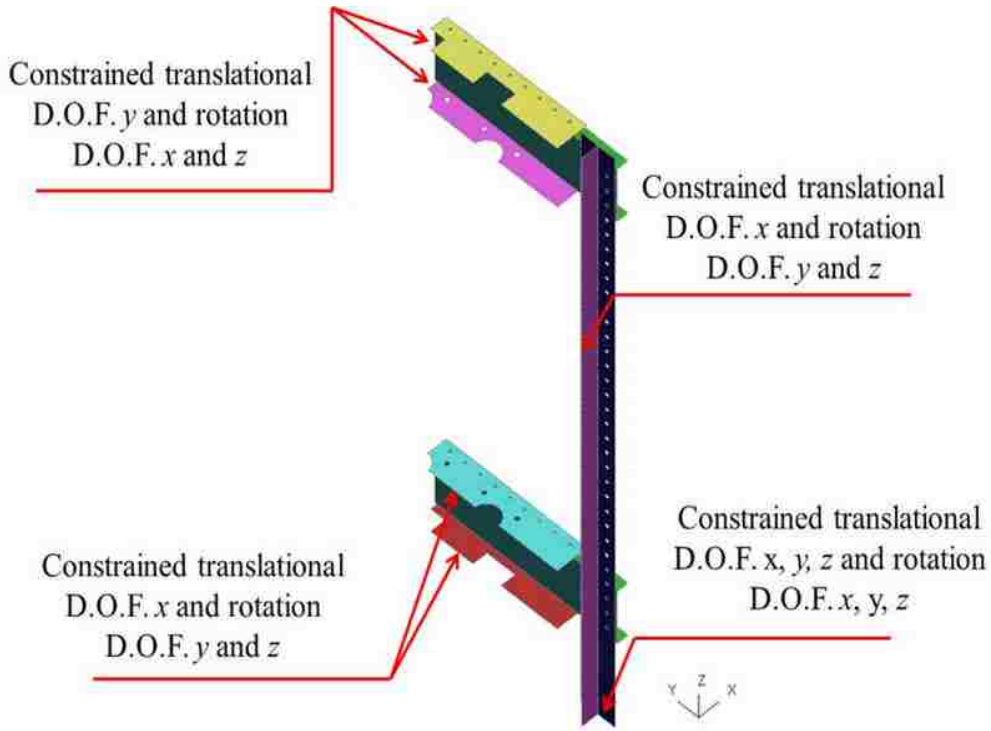

Figure C3: Boundary conditions of FE model

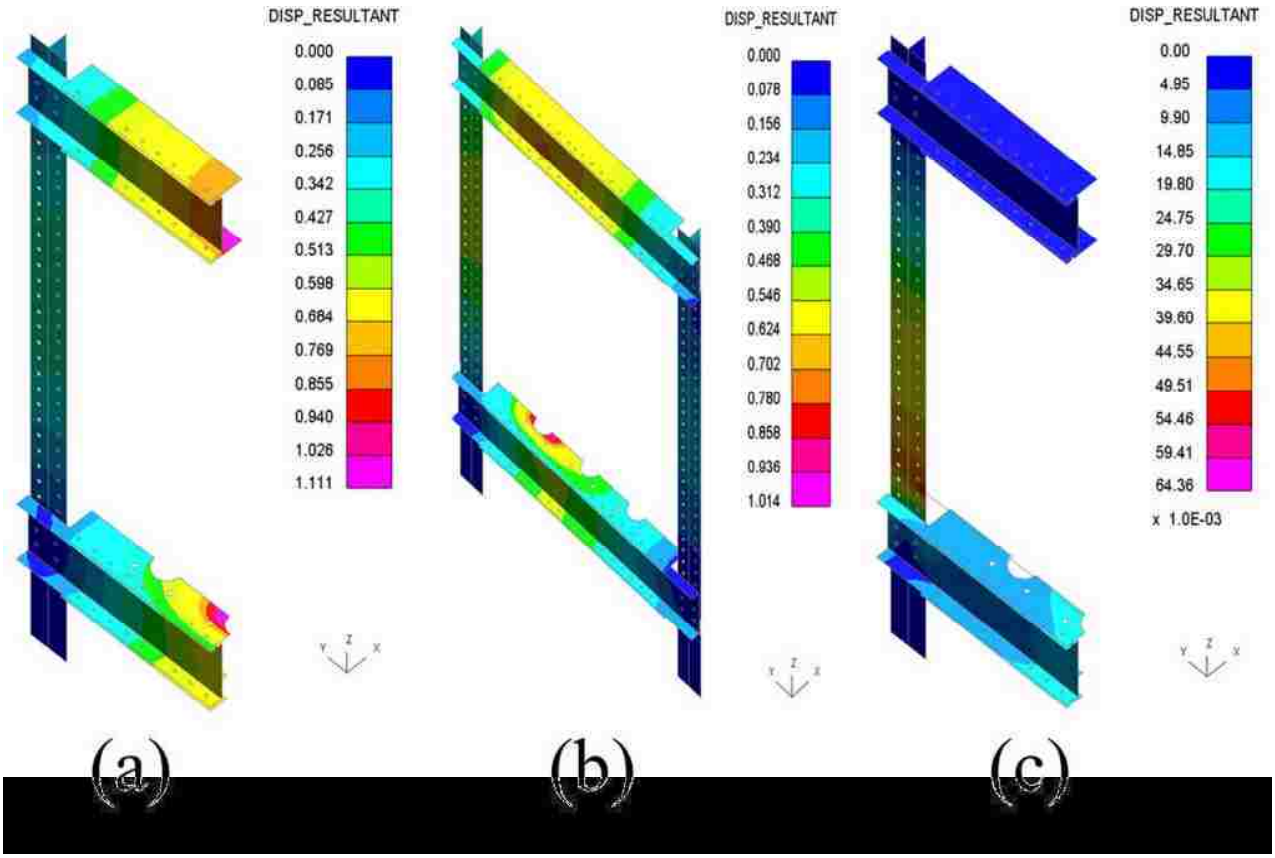

Figure C4: Displacement at ultimate state of (a) axial, (b) offset, and (c) transverse loading conditions. All units are in mm.

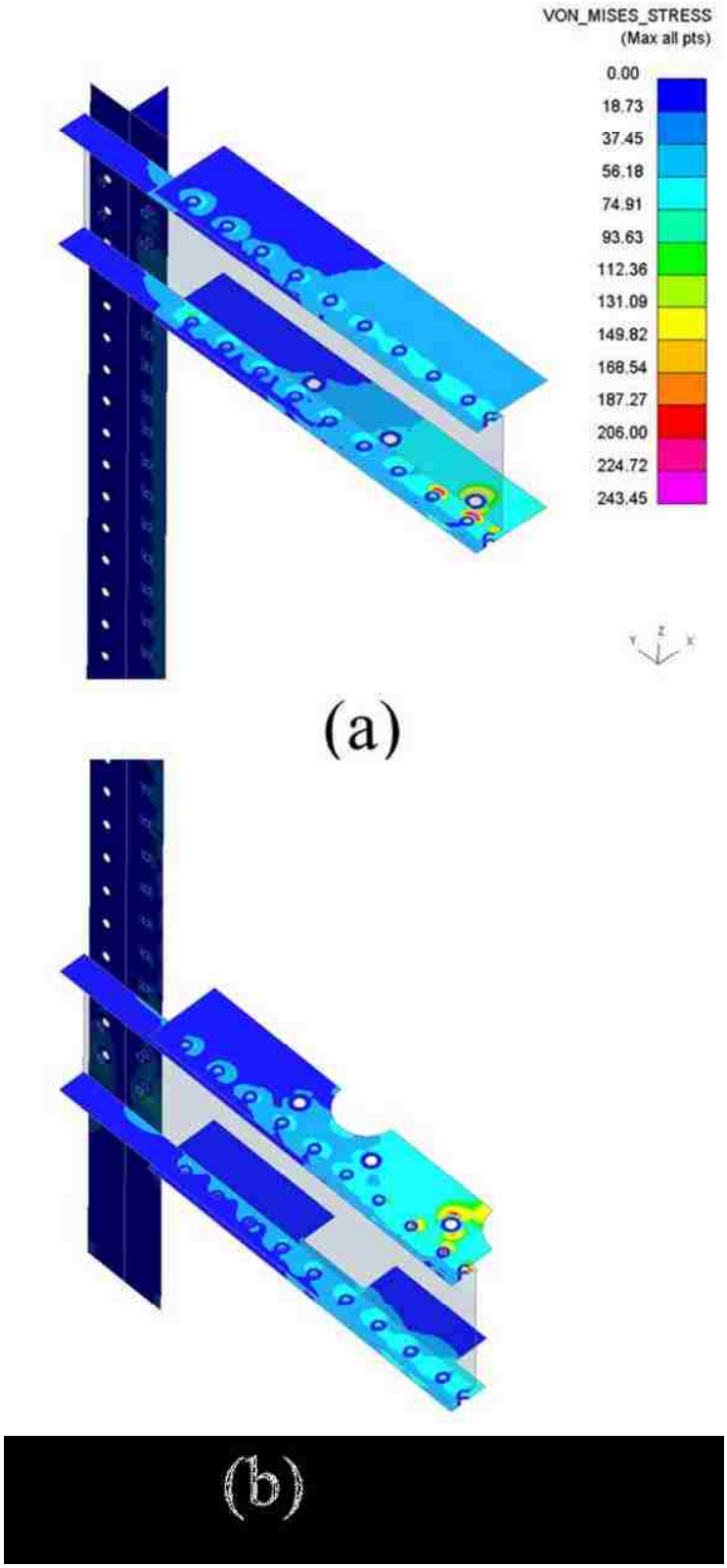

Figure C5: Von Mises stress contour plot of loading area (a) upper portion and (b) lower portion of the machine. All units are in MPa.

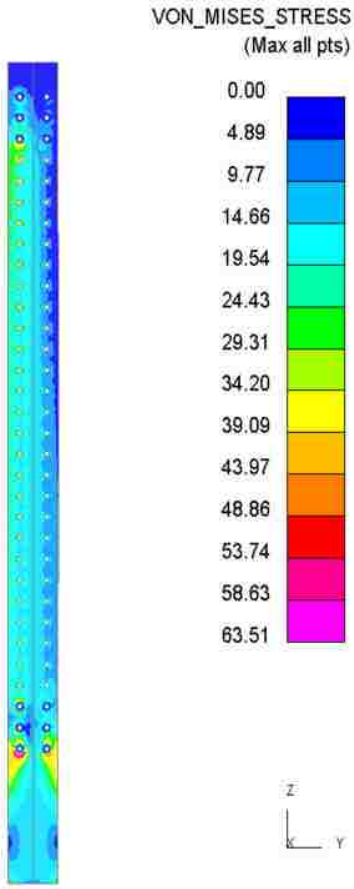

Figure C6 (a): Von Mises stress distribution of column at ultimate state. All units are in MPa.

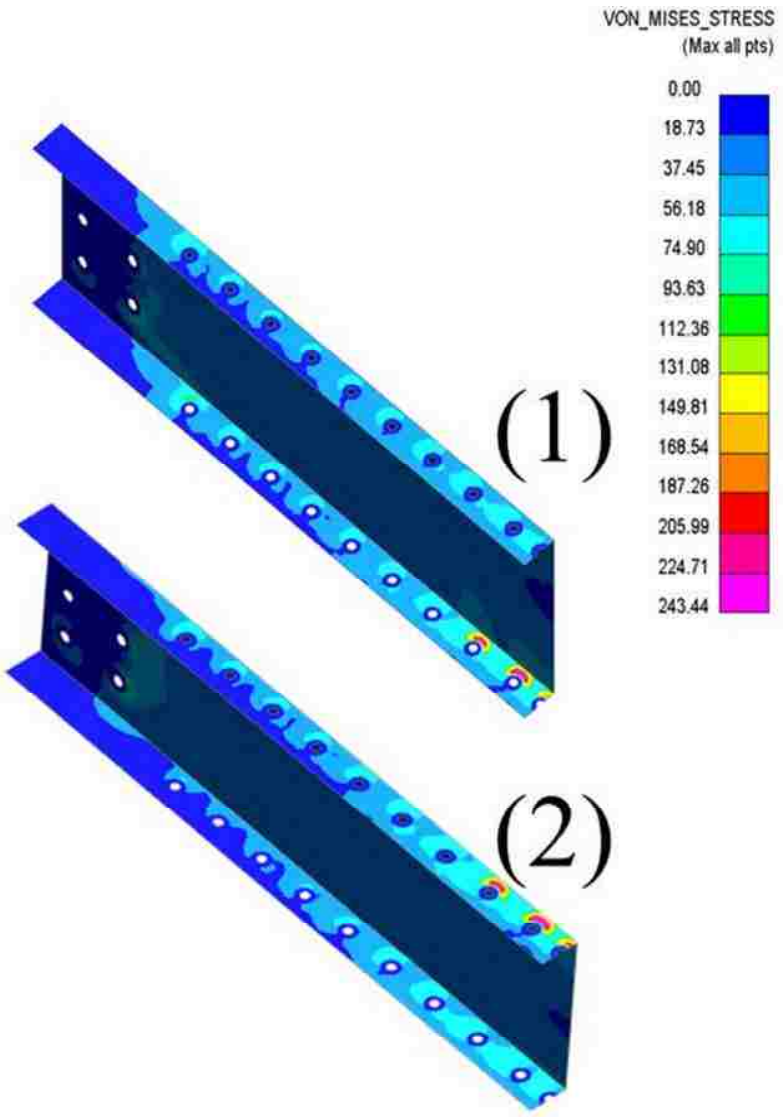

Figure C6 (b): Von Mises stress distribution of (1) upper beam and (2) lower beam at ultimate state. All units are in MPa.

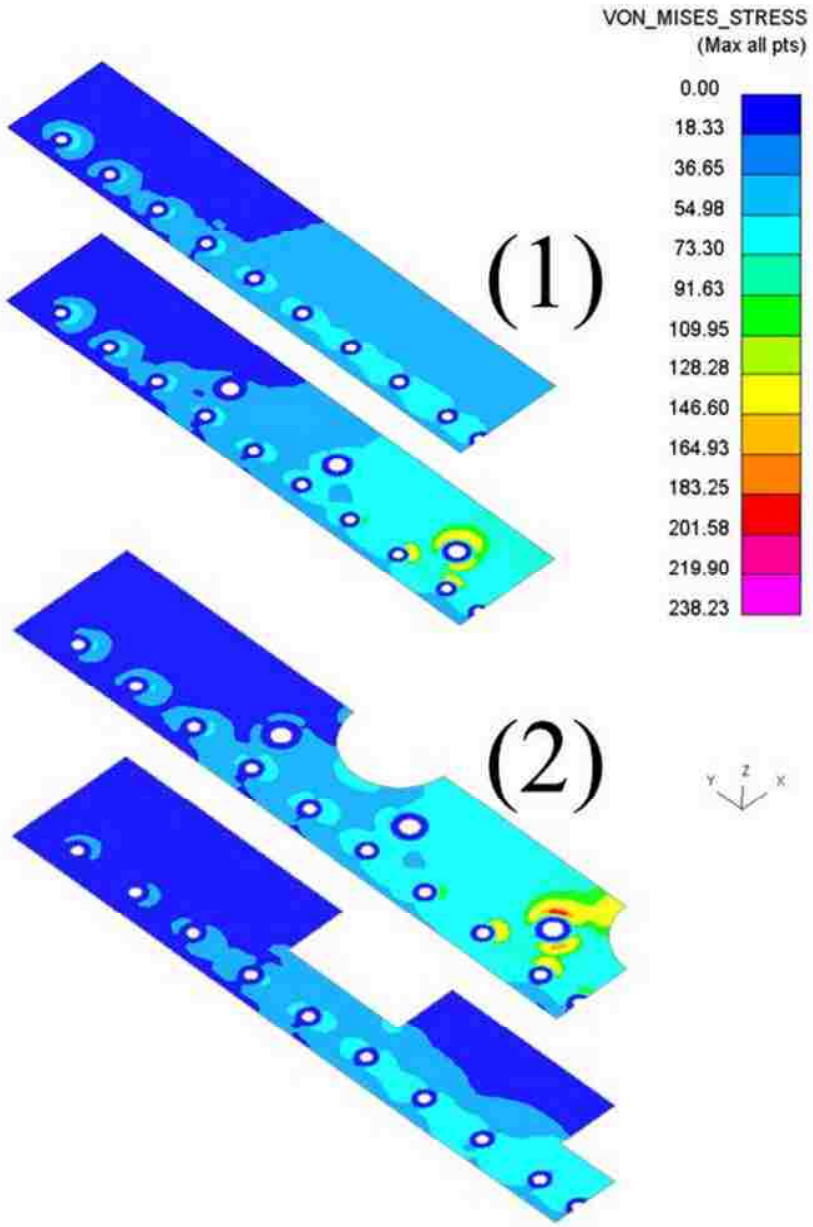

Figure C6 (c): Von Mises stress distribution of (1) upper portion plate stiffeners and (2) lower portion plate stiffeners at ultimate state. All units are in MPa.

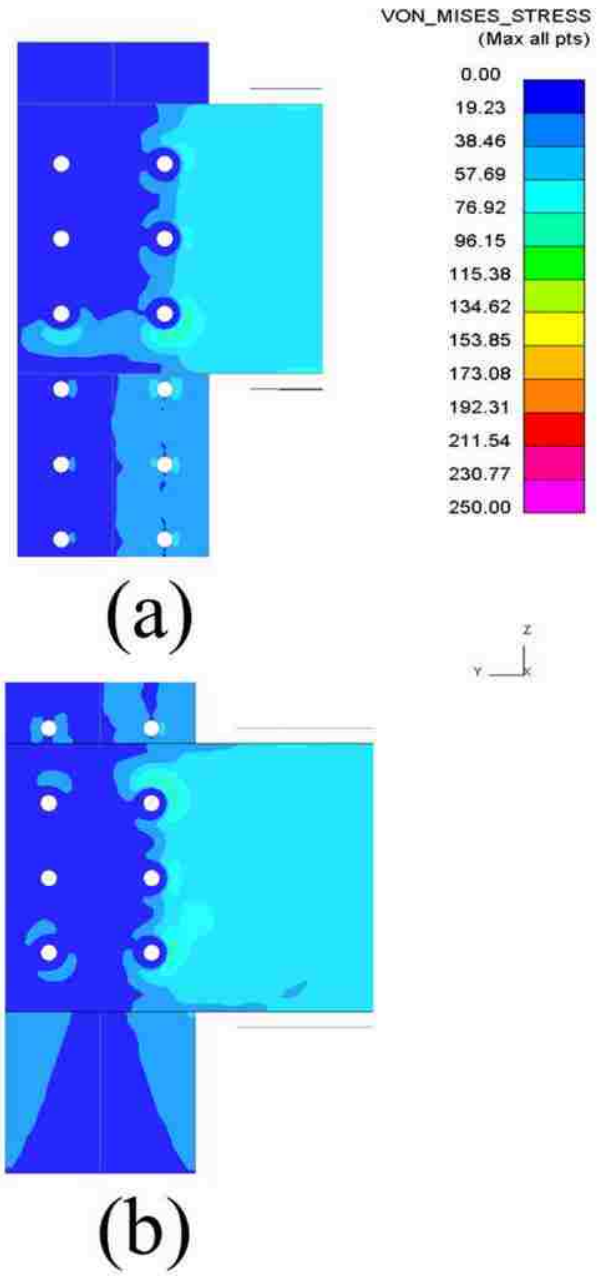

Figure C7: Stress distribution, under axial loading condition, of eccentric bearing connection at (a) upper portion and (b) lower portion of the machine. All units are in MPa.

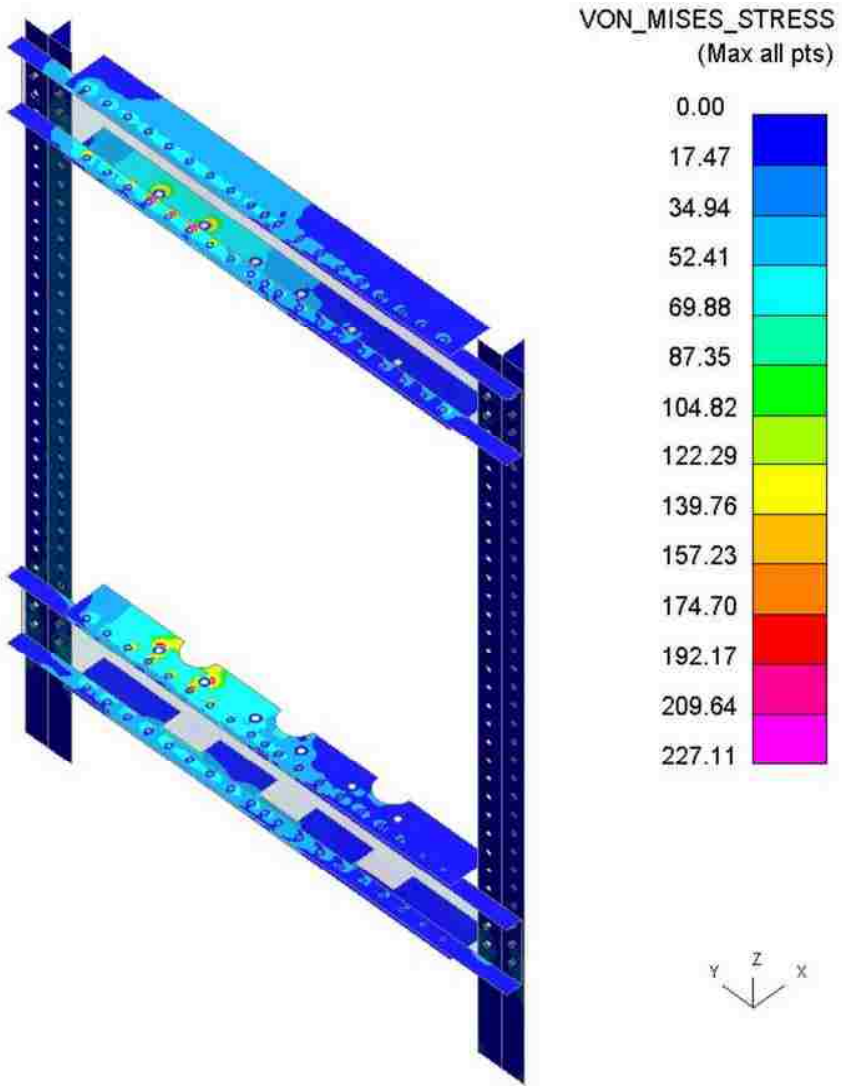

Figure C8: Von Mises stress distribution of the testing apparatus during offset loading condition. All units are in MPa.

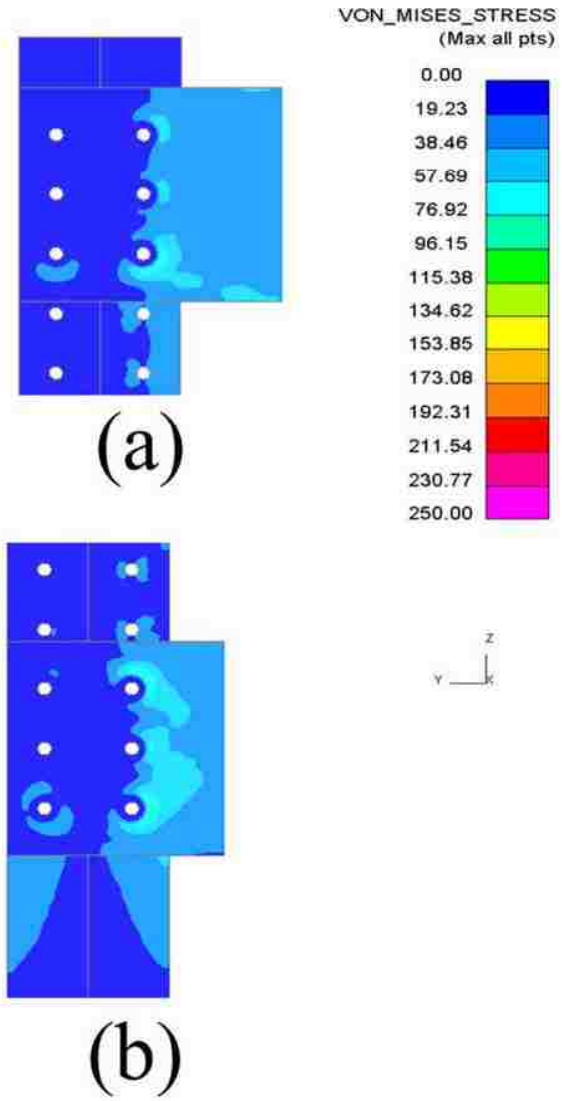

Figure C9: Stress distribution, under offset loading condition, of eccentric bearing connection at (a) upper portion and (b) lower portion of the machine. All units are in MPa.

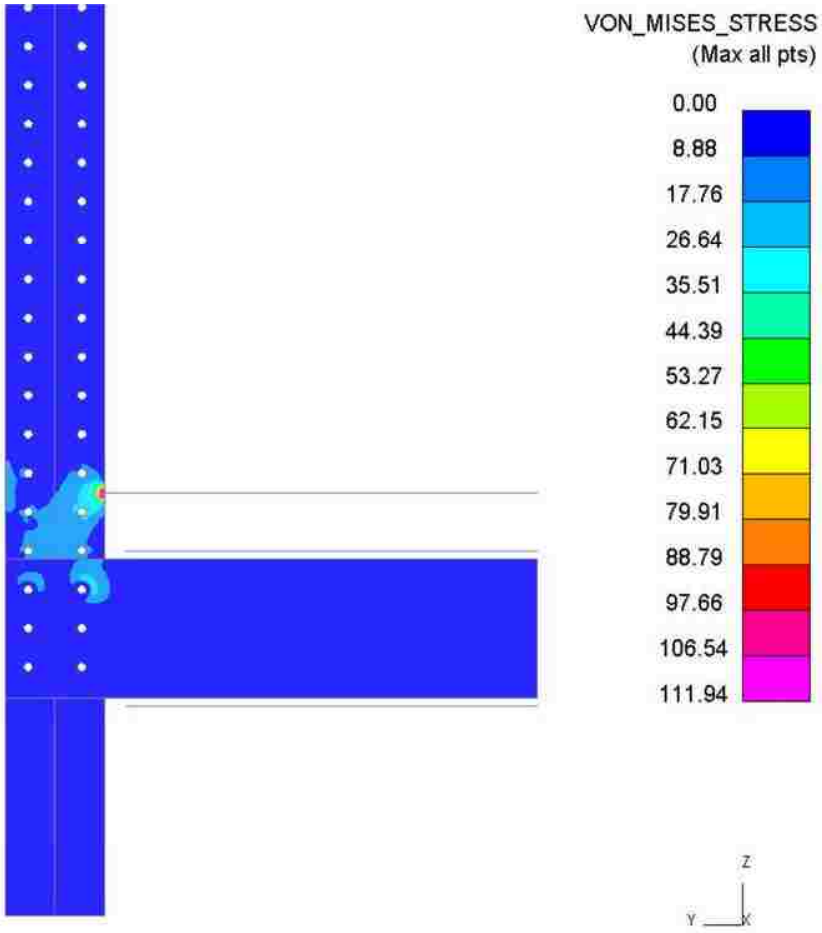

Figure C10: Von Mises stress distribution of the testing apparatus under transverse loading condition. All units are in MPa.

APPENDIX D: ENGINEERING STRESS VERSUS STRAIN RESPONSES OF FOAM CORE CONFIGURATIONS

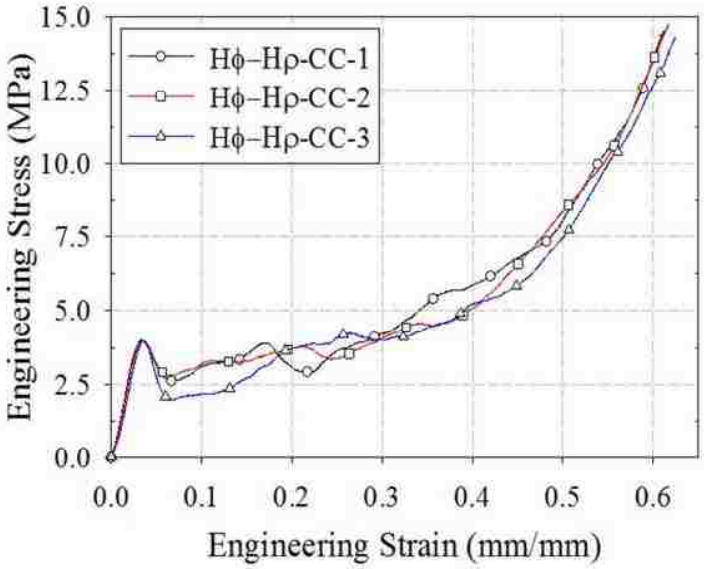

Figure D1: Stress/strain response of high diameter high density circular cores.

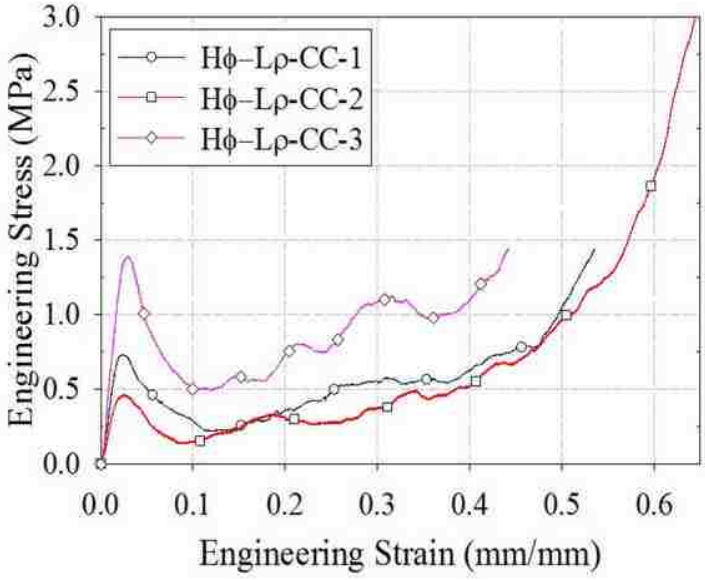

Figure D2: Stress/strain response of high diameter low density circular cores.

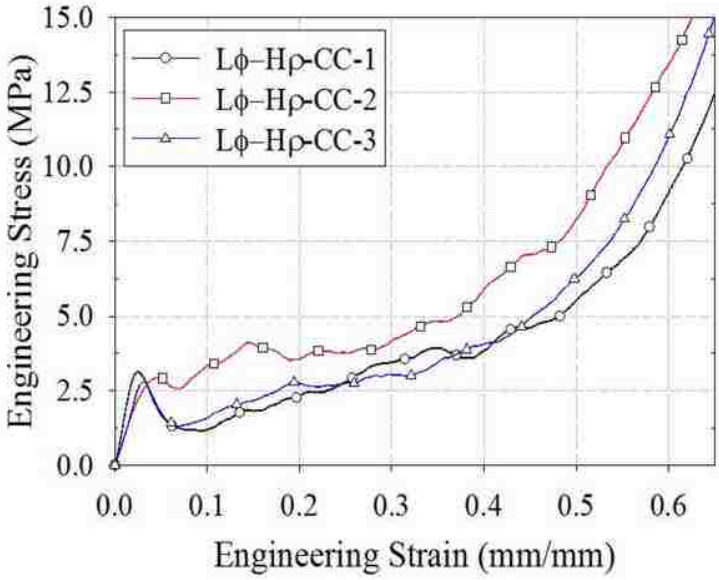

Figure D3: Stress/strain response of low diameter high density circular cores.

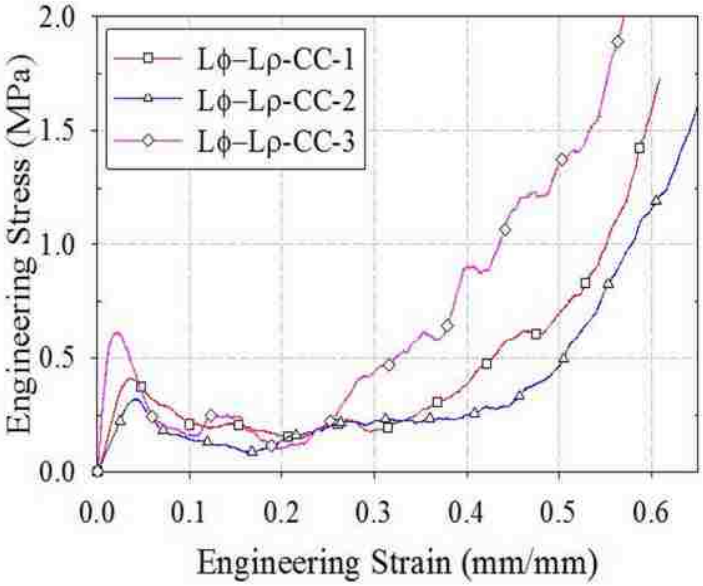

Figure D4: Stress/strain response of low diameter low density circular cores.

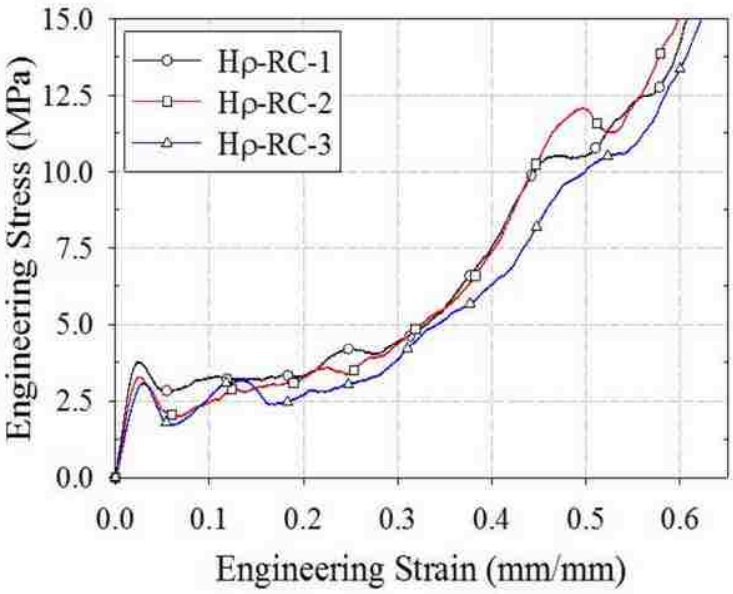

Figure D5: Stress/strain response of high density rectangular cores.

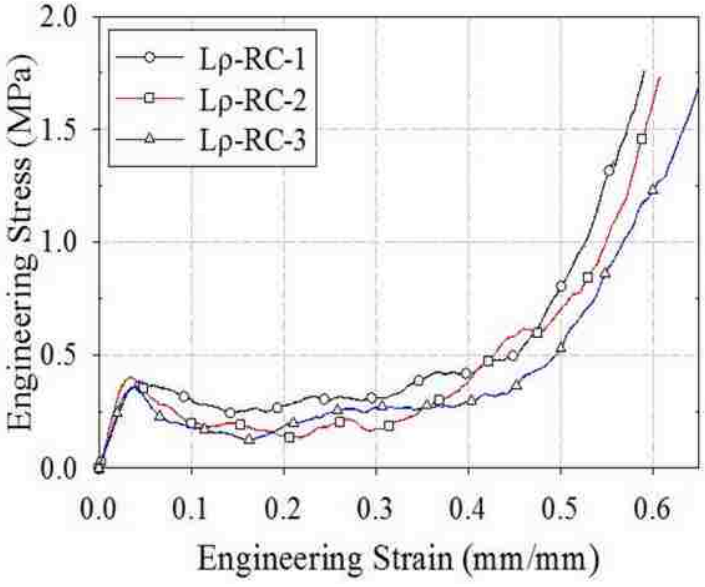

Figure D6: Stress/strain response of low density rectangular cores.

VITA AUCTORIS

NAME:	Ramsin Audysho
EDUCATION:	Assumption High School, Windsor, ON, 2001
	St. Clair College, O.C.A.D., Windsor, ON, 2006
	University of Windsor, B.A.Sc., Windsor, ON, 2009
PROFESSIONAL EXPERIENCE:	Process Engineer Nemak, Windsor Aluminum, Windsor, ON, 2006
	Safety Vehicle Development Chrysler Group LLC, Auburn Hills, MI, 2011
CANDIDATE:	University of Windsor, M.A.Sc., Windsor, ON, 2013